universität wien

DISSERTATION | DOCTORAL THESIS

Titel | Title

Hydroseismology - Ambient Seismic Noise Monitoring and Earth's Shallow Hydrosphere

verfasst von | submitted by

Richard Amon Kramer B.Sc. MSc.

angestrebter akademischer Grad | in partial fulfilment of the requirements for the degree of

Doktor der Naturwissenschaften (Dr.rer.nat.)

Wien | Vienna, 2025

Studienkennzahl lt. Studienblatt | Degree programme code as it appears on the student record sheet:	UA 796 605 416
Dissertationsgebiet lt. Studienblatt | Field of study as it appears on the student record sheet:	Geophysik
Betreut von | Supervisor:	Univ.-Prof. Dr. Götz Bokelmann

Abstract

As the disruption of the water cycle accelerates due to human overexploitation and global warming, monitoring and managing this resource has become increasingly important. Traditional satellite or well-based investigations offer a thorough overview of the current state of Earth's hydrosphere. However, those methods either lack sufficient spatial or temporal coverage. In recent years, a new branch of seismological applications based on ambient noise seismology has emerged. Environmental seismology focuses specifically on investigating the continuous temporal changes in seismic velocities within the subsurface that are related to environmental changes, such as variations in temperature or hydrology. This concept transforms existing and future seismic networks into environmental monitoring tools and is therefore a promising approach to bridging the observation gap between the traditional methods. These networks can track changes in key parameters such as ocean activity, groundwater depth, soil moisture, and ice thickness. The sensitivity of seismic waves to these properties provides insight into the dynamics of rapid changes occurring on our planet. Additionally, this new approach leverages the growing number of seismic stations and improved station coverage contributing to a more complete temporal and spatial resolution.

This thesis aims to expand the range of applications of seismic velocity monitoring to the Earth's hydrosphere. Cross-correlating time series of continuous ambient noise recordings and stacking the resulting noise correlations makes it possible to extract empirical Green's functions. Repeating this process provides a means of continuously probing the properties of the shallow Earth's subsurface down to the crust. Applying the concepts of coda wave interferometry (CWI) enables the detection and linking of velocity changes with a precision of 10^{-4}–10^{-5} to various parameters and influences. First, we use a dense local seismic array in Germany, and then regional networks across Central Europe, to focus on periodic relative seismic velocity changes (dv/v). Throughout our investigations, we discovered that these changes contain pronounced daily and sub-daily contributions. We linked air pressure fluctuations and their interaction with groundwater aquifers to changes in seismic velocity to explain our observations. Systematically investigating this behavior across Europe allowed us to evaluate the vulnerability of shallow groundwater reservoirs and improve our understanding of how environmental factors influence seismic velocities.

Furthermore, we extend the purely scientific context to an industrial application, using ambient seismology to provide tools for sustainable groundwater management and complement traditional hydrological datasets. We conduct a case study, applying time-lapse seismic tomography of a controlled pumping test in Austria, and demonstrate that passive imaging can be used for monitoring and provide continuous, spatial maps of seismic velocities closely linked to saturation changes. These maps offer a powerful complement to point-based well measurements.

These aspects show that ambient seismic monitoring advances our fundamental understanding of near-surface Earth processes and delivers practical, real-time insights to support water resource management under the pressures of climate change and human demand.

Kurzfassung

Da der Wasserkreislauf aufgrund der übermäßigen Nutzung durch den Menschen und der globalen Erwärmung mehr und mehr gestört wird, werden die Überwachung und das Management dieser Ressource immer wichtiger. Mithilfe traditioneller satelliten- oder bohrlochgestützter Untersuchungen lässt sich der aktuelle Zustand der Hydrosphäre der Erde umfassend ermitteln. Diese Methoden weisen jedoch entweder eine unzureichende räumliche oder zeitliche Abdeckung auf. In den letzten Jahren hat sich ein neuer Zweig seismologischer Anwendungen herausgebildet, der auf der Untersuchung von Umgebungsrauschen basiert. Die Umweltseismologie konzentriert sich speziell auf die Untersuchung kontinuierlicher zeitlicher Veränderungen der seismischen Geschwindigkeiten im Untergrund, die mit Umweltveränderungen, wie beispielsweise Temperaturschwankungen oder Veränderungen der Hydrologie, zusammenhängen. Dieses Konzept nutzt bestehende und künftige seismische Netze als Umweltsensoren und ist daher ein vielversprechender Ansatz, um die Beobachtungslücke zwischen den traditionellen Methoden zu schließen. Mithilfe dieser Netzwerke können Veränderungen wichtiger Parameter wie Meeresaktivität, Grundwassertiefe, Bodenfeuchtigkeit und Eisdicke erfasst werden. Die Empfindlichkeit der seismischen Wellen für diese Eigenschaften gibt Aufschluss über die Dynamik schneller Veränderungen auf unserem Planeten. Darüber hinaus nutzt dieser neue Ansatz die zunehmende Zahl seismischer Stationen sowie deren verbesserte Abdeckung, was zu einer vollständigeren zeitlichen und räumlichen Auflösung beiträgt.

Ziel dieser Arbeit ist es, das Anwendungsspektrum der seismischen Geschwindigkeitsüberwachung zu erweitern. Durch Kreuzkorrelation von Langzeitaufzeichnungen des Umgebungsrauschens und anschließendes Stapeln, lassen sich empirische Greensche Funktionen extrahieren. Mittels Coda-Wave-Interferometrie (CWI) können anschließend Geschwindigkeitsänderungen mit einer Präzision von 10^{-4}–10^{-5} nachgewiesen werden. Wir verwenden zunächst ein dichtes lokales seismisches Array in Deutschland und dann regionale Netzwerke in ganz Mitteleuropa, um uns auf periodische relative seismische Geschwindigkeitsänderungen (dv/v) zu konzentrieren. Im Laufe unserer Untersuchungen stellten wir fest, dass diese Veränderungen ausgeprägte tägliche und untertägige Schwankungen aufweisen. Um diese Beobachtungen zu erklären, haben wir Luftdruckschwankungen und ihre Wechselwirkung mit Grundwasserleitern mit Änderungen der seismischen Geschwindigkeit in Verbindung gebracht. Durch die systematische Untersuchung dieses Verhaltens in ganz Europa konnten wir die Anfälligkeit flacher Grundwasserreservoirs bewerten und unser Verständnis dafür verbessern, wie Umweltfaktoren die seismischen Geschwindigkeiten beeinflussen.

Darüber hinaus erweitern wir den rein wissenschaftlichen Kontext auf eine industrielle Anwendung, um mögliche Instrumente für ein nachhaltiges Grundwassermanagement bereitzustellen und herkömmliche hydrologische Datensätze zu ergänzen. Wir führen eine Fallstudie durch, in der wir seismische Zeitraffer-Tomographie bei einem kontrollierten Pumpversuch in Österreich anwenden. Wir zeigen, dass passive Bildgebungsverfahren kontinuierliche, räumliche Karten seismischer Geschwindigkeiten liefern, die eng mit Sättigungsänderungen korrelieren. Diese Karten stellen eine wirkungsvolle Ergänzung zu punktuellen Bohrlochmessungen dar.

Diese Ergebnisse belegen, dass passives Monitoring nicht nur unser grundlegendes Verständnis von Prozessen im oberflächennahen Untergrund voranbringt, sondern auch praxisnahe, Echtzeit-Einblicke liefert, die ein zukunftsfähiges Wassermanagement unter den Herausforderungen des Klimawandels und steigender Nachfrage unterstützen.

Acknowledgements

It takes a team. I would not have been able to complete my PhD without the support of a number of amazing people. This is an incomplete list of people I want to thank, and it is by no means an indication that I have forgotten those who aren't mentioned — you are on my mind and in my heart.

Firstly, I would like to thank Prof. Götz Bokelmann, my supervisor, for the opportunity to work at the University of Vienna, for his unwavering faith in my abilities, and for giving me the freedom to explore science and find my own academic path. I also would like to thank my incredible mentors, Yang, Chi, Qing-Yu, and Clément, for their endless kindness and support. It has been a pleasure to learn from you all, and I consider it a privilege and an honor to call you my friends. I also thank Christophe (Voisin) for the opportunity to conduct research in Grenoble. It is a great pleasure to learn from and collaborate with you.

Thanks to my other colleagues at IMGW, including Daniel, Cong, Helena, Titouan and Mohsen, for making everyday office life so enjoyable. Special thanks go to Herta and my officemate Yongki, not only for the endless coffee and lunch breaks, but also for their reliability in every situation, both at work and outside of it.

I would like to thank my parents for their never-ending support. Thank you for listening to me and my complaints on the phone, and for always having my back! Words cannot express my gratitude. I will be forever grateful! I would also like to thank the rest of my family for their support over the years.

Last but not least, I would like to thank my amazing friends. Some of you I have known for half my life or more. Thank you for sticking with me and acting as my unpaid psychologists and cheerleaders. To all the new people I met during my time in Vienna at workshops and conferences, you all have a special place in my heart!

We made it!

Dedication

- To my family, and especially to my beloved grandfather, who passed away far too early. -

Contents

List of Figures xiii

List of Tables xix

1. Introduction 1
- 1.1. Motivation for this Thesis . . . 1
- 1.2. Outline . . . 2

2. Utilizing Ambient Seismic Noise to Monitor Environmental Processes 3
- 2.1. Ambient Seismic Noise . . . 3
- 2.2. Noise Interferometry . . . 5
- 2.3. Applications of Noise Interferometry . . . 7
  - 2.3.1. Surface Wave Imaging . . . 8
  - 2.3.2. Monitoring of Relative Seismic Velocity Changes . . . 11
    - 2.3.2.1. Wave Equation from Hooke's Law . . . 11
    - 2.3.2.2. Coda Waves . . . 13
    - 2.3.2.3. Coda Wave Interferometry . . . 14
    - 2.3.2.4. Measuring Relative Seismic Velocity Changes . . . 15
    - 2.3.2.5. Origin of Relative Seismic Velocity Changes in the Earth's Crust . . . 17
- 2.4. Environmental Seismology - A New Set of Applications of Passive Seismic Observations . . . 19
  - 2.4.1. Environmental Seismic Sources . . . 20
  - 2.4.2. Monitoring Earth's Environment . . . 21
- 2.5. Aquifers under the Influence of Global Warming . . . 22
  - 2.5.1. Traditional Monitoring of Aquifers . . . 24
  - 2.5.2. Monitoring Earth's Hydrosphere Using Ambient Seismic Noise . . . 25
- 2.6. Concluding Remarks . . . 28

3. Main Cause of Sub-Daily Relative Seismic Velocity Changes 31
- 3.1. Introduction . . . 32
- 3.2. Data and Methods . . . 32
  - 3.2.1. GERES Array . . . 32
  - 3.2.2. Monitoring Seismic Velocity . . . 33
- 3.3. Results . . . 34
  - 3.3.1. Relative Seismic Velocity Changes . . . 34
  - 3.3.2. Spectral Analysis . . . 36
- 3.4. Discussion . . . 36
  - 3.4.1. Possible Environmental Effects Causing Seismic Velocity Variation . . . 36
  - 3.4.2. Interaction of Aquifers With Atmospheric Pressure . . . 38
  - 3.4.3. Second Order Effect: Temperature Changes . . . 40
  - 3.4.4. Comparison With Other Studies . . . 40

3.4.5. Perspectives . . . 41
3.5. Conclusions . . . 41
3.6. Extended Discussion . . . 44

4. Identifying Large Vulnerable Water Reservoirs Using Passive Seismic Monitoring 45
4.1. Introduction . . . 45
4.2. Data and methods . . . 47
4.2.1. Continuous seismic data . . . 47
4.2.2. Measurements of seismic velocity changes . . . 48
4.2.3. Measurements of atmospheric pressure . . . 50
4.2.4. Mapping spatial daily and semi-daily behavior of seismic velocities and meteorological parameters . . . 50
4.3. Results and discussion . . . 51
4.3.1. Periodic behavior of seismic velocity changes and air pressure . . . 51
4.3.2. Spatial variations of semi-daily velocity changes . . . 52
4.3.3. Mechanisms explaining the velocity changes . . . 53
4.3.4. Sub-daily seismic velocity changes as an indicator of vulnerable water reservoirs . . . 54
4.4. Challenges and limitations . . . 57
4.5. Conclusion . . . 57
4.6. Extended Discussion . . . 61

5. Monitoring Groundwater Pumping Using Time-Lapse Tomography 63
5.1. Introduction . . . 64
5.2. Integrated Hydrological and Seismic Monitoring of a Groundwater Pumping Test in Nickelsdorf (Burgenland, Austria) . . . 66
5.2.1. The Pumping Test Site . . . 66
5.2.2. Pumping Tests in Nickelsdorf - a Brief Hydrological Perspective . . . 66
5.2.3. Seismic Monitoring of the Nickelsdorf Pumping Tests . . . 69
5.3. Seismic Data Processing . . . 69
5.4. Towards Time-Lapse Tomography of Active Hydrological Experiments . . . 70
5.4.1. Inversion of 2-D Group Velocity Profiles . . . 72
5.4.2. Depth Inversion of the Profile . . . 75
5.4.2.1. General Subsurface Structure . . . 76
5.4.2.2. Influence of the Pumping to the Subsurface . . . 77
5.5. Limitations and Prospects for Optimization . . . 79
5.6. Conclusion and Outlook . . . 81
5.7. Extended Discussion . . . 84

6. Summary 85

7. Outlook 87

References 89

A. Appendix A: Main Cause of Sub-Daily Relative Seismic Velocity Changes 113

B. Appendix B: Identifying large vulnerable water reservoirs using passive seismic monitoring 117

C. Appendix C: Monitoring Groundwater Pumping Using Time-Lapse Tomography 123

List of Figures

2.1. A seismogram recorded close to the city of Vienna (OE.VIE). **a)** Daily record of the 7th of January including earthquake and noise records. **b)** Recorded P-, S- and surface wave arrivals of an earthquake in the Southern Tibetan Plateau. **c)** Zoom into the noise record of the seismometer. Note the decaying amplitudes in the nighttime compared to the afternoon. 3
2.2. Sources of ambient seismic noise. **a)** Schematic representation of potential natural and anthropogenic sources of ambient seismic noise (from Denolle and Nissen-Meyer, 2020). **b)** Power spectral density plot of records at seismic stations and the associated source. Additionally, the new low-noise (NLNM) and high-noise (NHNM) models (Peterson, 1993), are shown as gray lines (from Nakata et al., 2019). 5
2.3. Dispersion analysis. **a)** Surface waves filtered into different frequency bands showing different group velocities. **b)** Dispersion analysis normalized at each frequency. The blue dots show the picked group velocity and the green dots show the dispersion picks after applying the frequency re-centering introduced by Shapiro and Singh (1999) to account for systematic errors of the multiple filter analysis. 9
2.4. Schematic overview of the inversion procedure. While the procedure is the same for all inverse problems, the examples given are for solving the second step of ambient noise tomography. 10
2.5. Principle of the stretching method slightly modified after Hadziioannou (2011). **a)** ψ_{ref} is indicated as black line, while the red line is the ψ_{cur}. The different panels show the dilated waveforms for different stretching factors ε. **b)** The correlation coefficient for different values of ε between ψ_{ref} and ψ_{cur}. The black arrow indicates the relative seismic velocity change for this example. . . 16
2.6. Principle of the Moving Window Cross Spectral analysis slightly modified after Hadziioannou (2011). **a)** ψ_{ref} is indicated as black line, while the red line is the ψ_{cur}. **b)** Zoom into the window marked in **a)**. **c)** The phase for different frequencies of the cross-correlations derived from the cross-spectrum. **d)** Time shifts for different windows along the lapse time. The estimation of $\frac{\delta t}{t}$ with a linear regression is indicated with the dashed line. 17
2.7. Examples of seismic velocity change monitoring. **a)** Seismic velocity changes, GPS-recorded surface displacements, and tremor activity near Parkfield, California. The red curve indicates postseismic displacements along the San Andreas Fault measured by a GPS station (originally from Brenguier et al., 2008a). **b)** Seismic velocity changes measured at Piton de la Fournaise volcano as well as the seismic energy. The green columns indicating the periods of eruption (figure taken from Wang and Yao, 2020), originally from Brenguier et al., 2008b). 19
2.8. Sketch of hydrological processes on land. **a)** Factors which contribute to the water budget and cycle. **b)** Summary of factors controlling groundwater responses. (Figure from Wu et al. (2020) with slight modifications.) 23

3.1. (a) Location of the German Experimental Seismic System (GERES) array within Germany (inset). The zoom provides a more detailed overview of the topography of the region. (b) Configuration of the GERES array. The red dots indicate the position of the short-period seismometer GS-13. 33
3.2. (a) dv/v time series in the 4-8 Hz frequency band. The green curve shows a smoothed version of the hourly measurements (black line with crosses). (b) 2D spectrogram from a 7-day sliding window Fourier analysis. (c) Stack of the sliding windows. The red and blue lines indicate the one (S1) and two (S2) cycles per day, respectively. 35
3.3. Spectra of atmospheric pressure (blue line), temperature (red line), and dv/v (black dashed line). The inset shows the spectrum of the theoretically determined tidal strain at the German Experimental Seismic System array. Vertical lines indicate the main periods in the spectrum of different effects. 37
3.4. Schematic representation of the interaction of atmospheric pressure and water table depth. The illustration in the middle shows the pores of the different layers. 39

4.1. Maps of the study area. (**a**) Overview of topographical variations across Europe, including the main geological features (AF - Alpine Foreland, AM - Alpine Mountains, ApM - Apennines, DM - Dinarides, PB - Po Basin, and PM - Pyrenees). (**b**) Distribution of the broadband seismic stations. (**c**) Meteorological stations used within the study. 47
4.2. Conceptualization of our long-distance high-temporal resolution monitoring approach. (**a**) Location of two stations of the Italian seismic network. (**b**) Normalized hourly cross-correlations between the two stations vertical component within the investigation time period. (**c**) Stacked cross-correlation for every hour. Each trace represents the stack of all corresponding hours within the time period. The arrow around 15 s indicates the theoretical arrival time of surface waves, followed by coda-wave windows. 49
4.3. Comparison of the periodic patterns of seismic velocity changes and air pressure (averaged over the entire study area). The orange and blue dots represent the averaged measurements of (**a**) seismic dv/v and (**b**) air pressure. The dashed black line indicates the synthetic data from fitting sinusoidal functions using 24-hour, 12-hour, and 8-hour periods. The red and blue lines represent the fitted daily and semi-daily terms, respectively. The S_3 curve has been omitted for illustration reasons and can be found in the supplementary section (see Fig. B.2). 51

4.4. Spatial distribution of the amplitude of S_2. (**a**) S_2 amplitude for seismic velocity change (dv/v). The green contours outline aquifers characterized by continuous carbonates, moderate to high permeability, and large pore size (Cornu et al., 2013; Chen et al., 2017; Xanke et al., 2022).(**b**) S_2 amplitude of air pressure oscillations. The white contour outlines the Alpine Mountains. (Note: the amplitude of the air pressure refers to a de-meaned time series. The amplitude of air pressure oscillations (about 50 Pa) is much smaller than the absolute value of sea-level pressure (about 10^5 Pa) 53
4.5. Schematic evolution of the capillary fringe under different air pressure conditions. The left panel illustrates the decrease in capillary thickness under low air pressure, resulting in an increase in seismic wave velocity. The right panel depicts the process under high air pressure, where the capillary fringe becomes thicker with a lowered water table. The zoom-in in the middle shows the alteration in compressible air space with and without water infiltration (modified after Fabbri et al. (2019)). The orange shaded areas schematically represent the parts sampled by the coda waves. 55

5.1. The Nickelsdorf pumping test site showing locations of nodal seismic sensors (white triangles), hydrological wells (red circles) and local characteristics. The inset shows the location of the site within Austria. 67
5.2. Hydrological characteristics of the pumping tests. Panel **a)** shows a schematic view of the lowering of the groundwater table for each pumping phase. In panel **b)** and **c)** the groundwater levels (GWL) of the two wells EKB5 and EKB7 are presented. The encircled numbers are the phases of the pumping test, while the abbreviation "CP" stands for clear pumping and "TV" marks the time of the demonstration for the TV broadcast station. 68
5.3. Seismic waveforms from correlations of train generated noise. **a)** is the distance-time plot for all correlations stacked over the whole time period. **b)** shows the correlations over time for a representative station pair "104-113". The abbreviations "HM" and "FM" refer to higher mode and fundamental mode. The encircled numbers are the phases of the pumping test and the blue lines bound the time periods of each pumping test. 71
5.4. Dispersion analysis of station pair "102-114". **a)** Seismic profile with stations in gray, the analyzed station-pair is highlighted in black and has an inter-station distance of 150 m. **b)** Normalized cross-correlations filtered into different frequency bands. **c)** Dispersion analysis normalized by the maximum of the signals and **d)** by the maximum in every frequency band. The blue dots represent the picked dispersion curves, while the green dots are the re-centered picks. The yellow dashed lines indicate a lower and upper bound for the group velocities to guide the automated picking. 72

5.5. Temporal evolution of group velocities for station pair "104-113". **a)** Groundwater level but color coded for well EKB7. Blueish colors means higher water saturation in the subsurface, while reddish color indicate the opposite. **b)** Group velocities of different frequencies over time in the experiment. Note that, the two gaps are associated with field work and replacement of instruments. 73
5.6. 2-D group velocity profiles after the first step of inversion. Panels **a), b), d),** and **e)** show the obtained group velocities for the days 9, 20, 59, and 75. Panel **c** shows the groundwater level. The blue dashed lines indicate the start and end of the pumping cycles at EKB7. 75
5.7. 1-D depth inversion result for grid point 38 (close to the EKB7 well) for day 0. **a)** Posterior probability density for the grid point shown as v_s-depth profile. The red dashed line shows the mean, while the two black dashed lines are the standard deviation. **b)** Shows the local dispersion curve from the group velocity results (red dashed line) and the associated uncertainty. The background shows the fit of this local dispersion curve by the models produced by the McMC algorithm. **c)** Resulting v_S model obtained for day 0 of our experiment. The blue dashed lines indicated the measured groundwater table depth. The grey shaded areas mark parts where the relative standard deviation is higher than 40%. 77
5.8. v_s model of the transect obtained from the depth inversion. Panels **a), b), d),** and **e)** show the resulting v_s-models for the days 9, 20, 59 and 75. The blue dashed line indicates the groundwater table measured along the transect. The grey shaded areas mark parts where the relative standard deviation is higher than 40%. **c)** Shows the groundwater level. The blue dashed lines indicate the start and end of the pumping cycles at EKB7. 78
5.9. Temporal evolution of v_s during the pumping experiment. **a)** GWLTS but color coded. Blueish colors means higher water saturation in the subsurface, while reddish color indicate the opposite. **b)** v_s extracted for different depth from the final velocity models and averaged between 45 m and 135 m along the transect. The dashed blue lines indicate the start and the end of the pumping of the different phases. Note that, the two gaps are associated with field work and replacement of instruments. 80

A.1. **a)** Estimated shear-wave velocity profile for the investigated region. **b)** Sensitivity kernels calculated with the software of Herrmann (2013). The shown frequency is the center frequency of the different frequency bands. 113
A.2. Relative seismic velocity changes for different frequency bands. The green curve shows a smoothed version of the hourly measurements (black line with crosses). 114
A.3. 2D spectrograms calculated within a 7-day sliding window Fourier analysis. The three different panels show the different frequency bands. 115

A.4. Stack of the 2D spectrograms of Fig. S3. Each panel shows a different frequency band. The red and the blue line indicates the one (S_1) and two (S_2) cycles per day, respectively. 116

B.1. Temporal stability of the air pressure signal and the decomposition into the main periods of 24 h and 12 h. The panels (**a**) - (**d**) show the air pressure signals for the year 2016 - 2019 averaged over the whole investigation area. The dashed black line indicates the synthetic data from fitting sinusoidal functions using both 24-hour and 12-hour periods. The red and blue lines represent the fitted daily and semi-daily terms, respectively. 117
B.2. Temporal stability of the dv/v measurements (averaged over the study area) and the decomposition into the main periods of 24 h, 12 h and 8 h. (**a**) Shows the dv/v over the whole time from 2016 - 2019. The subfigures (**b**) - (**d**) show the stacking over two years as indicated to ensure a comparable station coverage. Panel (**e**) and (**f**) show the stacking result over winter and summer, respectively. The dashed black line indicates the synthetic data from fitting sinusoidal functions using both 24-hour and 12-hour periods. The red, blue and green lines represent the fitted daily, semi-daily and tri-daily terms, respectively. 118
B.3. Group velocity measurements across the study area in the frequency band around 1 Hz. 119
B.4. Map of the relative mean absolute misfit between the measured dv/v and the results of the fitting with three sinusoids with periods of 24 h, 12 h and 8 h. . 120
B.5. Histogram of the time delays between the air pressure (forcing) and the dv/v (reaction). 121

C.1. Simplified lithological log determined from core samples of **a)** the EKB5 and **b)** the EKB7 well. 123
C.2. Dispersion picks for all frequencies over 93 days from station pairs **a)** "102-114", **b)** "103-114" and **c)** "104-114". The red dashed line indicated the median dispersion curve. 124
C.3. Hyper-parameter estimates obtained from the inversion of group velocity dispersion data for day 89. **a)** Histogram of the posterior distribution on the number of nodes. **b)** Diagram shows the linear coefficient between unknown data errors and travel path length. **c)** and **d)** show the constant terms for unknown data error. 125
C.4. Estimated uncertainties from the 2-D group velocity inversion obtained from the ensemble of rjMcMC samples. The panels show day **a)** 9, **b)** 20, **c)** 59 and **d)** 75. 126
C.5. Temporal evolution of group velocities from **a)** dispersion analysis of station pair "104-113" and **b)** extracted from the 2-D group velocity profiles between 45 m and 135 m, corresponding to the extent of station pair "104-113". **c)** Shows the associated uncertainties for group velocities shown in **b)**. 127
C.6. Coefficient of variation (relative standard deviation) estimated from the McMC samples for the 1-D depth inversion results of day **a)** 9, **b)** 20, **c)** 59 and **d)** 75. 128

List of Tables

C.1. Prior bounds for the 2-D probabilistic inversion. U_0 is the group velocity, while a, b and c are the error parameters in $\sigma_i = a\Delta_i + b + c$·f. 129
C.2. Prior bounds for the 1-D depth inversion. Note: The last layer is the infinite half-space. 129

1 Introduction

1.1. Motivation for this Thesis

Over the past two decades, ambient noise seismology has emerged as an effective and widely used field within seismology. This approach is based on the principle that the Green's function can be reconstructed by correlating continuous noise recordings from two individual seismic stations. The resulting cross-correlation, represents the estimated Green's function between one station (acting as a virtual source) to another station (the receiver). Thus, this process reveals valuable information about the medium and its changes as the wavefield propagates through it. One significant advantage of this method over traditional earthquake seismology is that it does not require active sources. Instead, it utilizes the continuous presence of seismic ambient noise, enabling applications such as continuous monitoring and time-lapse imaging. This independence from earthquakes or active sources has facilitated a wide range of applications, including observing changes within the (shallow) crust and environmental monitoring. For example, ambient noise seismology has been used to monitor rock damage caused by earthquakes, assess volcanic activity, and detect changes in subsurface saturation.

These applications require a complete understanding of potential interfering processes that overprint the desired information. Although, much more advanced in other disciplines, the origin, strength, and potential removal of environmental effects on seismic velocities is still under debate and development. This thesis aims to fill existing gaps in the understanding of environmental effects on seismic velocities and explores the potential of ambient noise monitoring and imaging within the hydrological context. A deeper understanding of water resources is becoming increasingly crucial as society faces multiple challenges, including population growth, increased industrial activity, and the impacts of climate change, factors that collectively intensify the demand for water. Although water availability is not currently a critical issue in the northern hemisphere, effective and sustainable water management and monitoring methods will be essential to ensure that this remains the case in the future.

The research presented in this thesis begins with an investigation of daily and sub-daily seismic velocity changes beneath a small seismic array, focusing on the influence of atmospheric pressure changes on seismic velocities. By scaling this analysis to a larger context, we were able to utilize sub-daily seismic velocity changes to infer the vulnerability of water reservoirs, an assessment traditionally limited to localized, point-based measurements. To bridge the gap between purely scientific observations and industrial applications, the thesis concludes with a case study involving the monitoring of a groundwater pumping test using time-lapse tomography. By combining seismic techniques with hydrological observations, this thesis opens up new possibilities for transforming seismic data into practical tools for understanding the environment under rapidly changing conditions.

1.2. Outline

The core of this thesis is built around three manuscripts:

- **"Interaction of Air Pressure and Groundwater as Main Cause of Sub-Daily Relative Seismic Velocity Changes"** by Kramer et al. (2023) published in Geophysical Research Letters (GRL). This paper presents a novel observation of strong sub-daily periodicity in seismic velocities from high temporal resolution monitoring and introduces a first simple explanatory model (see chapter 3).
- **"Identifying large vulnerable water reservoirs using passive seismic monitoring"** by Kramer et al. (2025) published in Earth and Planetary Science Letters (EPSL). Building on the first paper, this study explores regional variations in periodic seismic velocity changes and their implications (see chapter 4).
- **"Monitoring Groundwater Pumping Using Time-Lapse Tomography from Ambient Seismic Noise"** by Kramer et al. (2025) submitted to Water Resources Research. This research focuses on monitoring groundwater pumping tests and examines the potential of ambient noise monitoring in applied hydrological contexts (see chapter 5).

To establish a foundation for the concepts and methodologies discussed in this thesis, Chapter 2 introduces the field of ambient noise and environmental seismology. It covers the fundamental principles of ambient noise monitoring and imaging, along with recent developments that have led to this research. The final chapters provide an overview of the unresolved questions and potential directions for future studies, as well as a summary of the thesis.

2 Utilizing Ambient Seismic Noise to Monitor Environmental Processes

This chapter establishes the theoretical foundation for the research presented in this thesis. It begins by explaining the term *ambient noise* and its origin. Next, it introduces the concept of *noise interferometry* and demonstrates the relationship between cross-correlation and the Green's function. The principles of *seismic imaging* and *relative seismic velocity monitoring* based on ambient noise are then presented. Finally, the chapter explores the emerging field of *environmental seismology* and outlines the research questions that frame this thesis.

2.1. Ambient Seismic Noise

The term ambient seismic noise refers to the persistent background wavefield generated by a variety of natural and anthropogenic mechanisms (Nakata et al., 2019). In seismometer records, this noise appears as low-amplitude signals present continuously before, during, and after earthquakes (see Fig. 2.1).

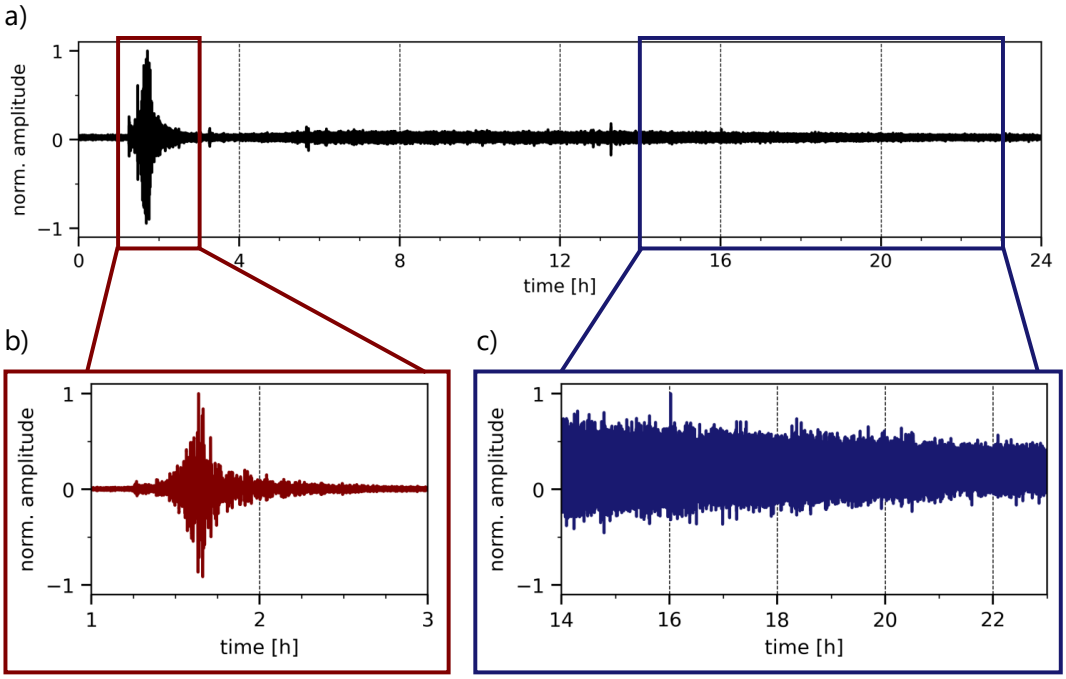


Figure 2.1.: A seismogram recorded close to the city of Vienna (OE.VIE). **a)** Daily record of the 7th of January including earthquake and noise records. **b)** Recorded P-, S- and surface wave arrivals of an earthquake in the Southern Tibetan Plateau. **c)** Zoom into the noise record of the seismometer. Note the decaying amplitudes in the nighttime compared to the afternoon.

Although the term ambient noise is widely used today, it is important to differentiate between its various source mechanisms. The origins of seismic noise can be broadly classified into three categories based on the period of the waves they generate: short-, mid-range, and long-period noise.

Short-Period Noise (0.1–1 s) is predominantly driven by anthropogenic sources, such as human activities. Common contributors include cars, trains, wind turbines, and industrial machinery, through which energy is coupled into the subsurface. The period band for anthropogenic noise typically falls within 0.1 to 1 s (Nakata et al., 2019). This type of noise exhibits clear daily and weekly cycles, closely reflecting human behavior and routines (Lecocq et al., 2020). During extraordinary global events, such as the COVID-19 lockdowns, significant reductions in short-period noise were observed, highlighting the impact of human activity on the ambient seismic wavefield (Lecocq et al., 2020). In addition to human activities, short-period noise can also be driven by natural phenomena, such as wind. Strong winds generate noise by interacting with buildings, trees, and loose debris, effectively coupling surface waves into the subsurface.

Mid-range period noise (1-20 s), is predominantly driven by the interaction of atmospheric turbulence and oceanic waves with the solid Earth. A notable component of this category is oceanic microseism, which constitutes a significant portion of the ambient noise field. Oceanic microseism can be divided into two types:

- Primary microseism ($T \approx 14$ s): This occurs when ocean waves directly couple into the seafloor in shallow coastal regions (Hasselmann, 1963; Ardhuin et al., 2011). The energy transfer results in seismic waves that propagate through the Earth's crust.
- Secondary microseism ($T \approx 7$ s): This arises when two ocean waves of the same frequency but traveling in opposite directions interact, forming standing waves. These standing waves generate periodic pressure variations on the seafloor, which contribute to seismic noise (Longuet-Higgins and Jeffreys, 1950; Ardhuin et al., 2015).

Secondary microseism is particularly significant because it is more energetic than primary microseism and is generated in deeper waters, making it less dependent on proximity to the coast. It can propagate over large distances, making them a valuable source of information for global and regional seismic studies (Ardhuin et al., 2011; Gualtieri et al., 2013).

Long-period noise (50–300 s), also known as seismic hum, represents the lower-frequency end of the noise spectrum. The primary sources of seismic hum are ocean infragravity waves (Webb, 2008; Bromirski and Gerstoft, 2009). These infragravity waves interact with the seafloor and induce pressure fluctuations that propagate through the solid Earth as seismic waves (Rhie and Romanowicz, 2004; Uchiyama and McWilliams, 2008; Ardhuin et al., 2015).

The relative strength of these noise components is typically visualized using power spectral density (PSD) plots, which quantify noise levels across different frequency bands (Peterson, 1993). Fig. 2.2 shows a summary of all the effects discussed as well as two examples of PSD plots for two seismic stations.

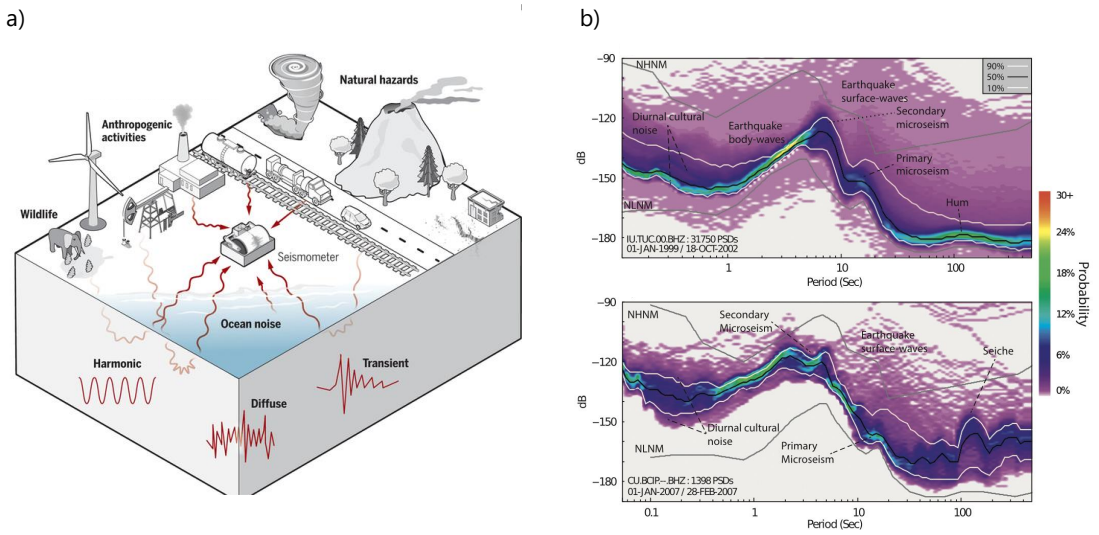


Figure 2.2.: Sources of ambient seismic noise. **a)** Schematic representation of potential natural and anthropogenic sources of ambient seismic noise (from Denolle and Nissen-Meyer, 2020). **b)** Power spectral density plot of records at seismic stations and the associated source. Additionally, the new low-noise (NLNM) and high-noise (NHNM) models (Peterson, 1993), are shown as gray lines (from Nakata et al., 2019).

2.2. Noise Interferometry

After discussing the origins and characteristics of ambient seismic noise, this section explores how the ambient seismic wavefield can be leveraged to retrieve the Green's function, enabling seismic imaging and monitoring applications. The theoretical frameworks for Green's function retrieval rely on the fundamental assumption that the ambient wavefield is equipartitioned, a state in which all wave propagation modes (e.g., body waves, surface waves) are statistically uncorrelated, evenly distributed, and carry equal energy. Equipartitioning can occur in two distinct ways: (1) directly, through the presence of uncorrelated and spatially homogeneous noise sources, or (2) indirectly, through strong multiple scattering within a medium, which redistributes energy among all available modes, effectively homogenizing the wavefield. In practice, perfect equipartitioning is rare. However, empirical studies have shown that the Green's function can still be reasonably approximated under less ideal conditions, depending on the density and distribution of sources (Weaver and Lobkis, 2002; Roux et al., 2005).

Several theoretical approaches establish the connection between the Green's function and the cross-correlation of ambient noise, such as those based on representation theorems, diffusion equations, or energy equipartitioning. However, this section focuses on the theory derived from the summation of normal modes, as presented by Lobkis and Weaver (2001). This method

offers an intuitive framework for understanding how the Green's function emerges from the noise field through the superposition of wave modes.

The derivation begins with the displacement response of the Earth to a wavefield, expressed in terms of normal modes:

$$u(\mathbf{r},t) = \sum_m \frac{u_m(\mathbf{r})}{\omega_m} \left(a_m \sin\omega_m t + b_m \cos\omega_m t\right), \tag{2.1}$$

where $u_m(\mathbf{r})$ is the eigenfunction of mode m, ω is the angular frequency, a_m and b_m are random coefficients that represent the contributions of mode m to the displacement field. As a first step, the time derivative of Eq. 2.1 is calculated, leading to:

$$v(\mathbf{r},t) = \sum_m u_m(\mathbf{r}) \left(a_m \cos\omega_m t - b_m \sin\omega_m t\right), \tag{2.2}$$

which can be understood as the measured velocity response of the Earth due to normal modes. In the next step, the characteristics of random ambient noise are introduced. We assume that the coefficients a and b satisfy the following conditions:

$$\langle a_n a_m\rangle = E^2\delta_{nm}, \tag{2.3}$$
$$\langle b_n b_m\rangle = E^2\delta_{nm}, \tag{2.4}$$
$$\langle a_n b_m\rangle = 0, \tag{2.5}$$

where E_m is the energy of mode m, and δ_{nm} is the Kronecker delta. While Eqs. 2.3 - 2.4 ensure that the excitation of different modes is uncorrelated, Eq. 2.5 indicates that the sine and cosine terms are statistically uncorrelated. In other words, each excited mode is uncorrelated with the others, and every mode is excited with the same energy (equipartitioning). Currently, Eq. 2.2 expresses the noise wavefield at a single position, $\mathbf{r}_A$. Now, we introduce another noise wavefield at position $\mathbf{r}_B$. By cross-correlating these two wavefields, we obtain:

$$C_{AB}^{(v)}(\tau) = \langle v(\mathbf{r}_A,t)v(\mathbf{r}_B,t+\tau)\rangle\,. \tag{2.6}$$

This cross-correlation can be represented as a sum of normal modes as follows:

$$\begin{aligned} C_{AB}^{(v)}(\tau) = \sum_{n,m} & u_n(\mathbf{r}_A)u_m(\mathbf{r}_B) \\ & \times \Big\{ \langle a_n a_m\rangle \cos\omega_n t \cos\omega_m(t+\tau) \\ & - \langle a_n b_m\rangle \cos\omega_n t \sin\omega_m(t+\tau) \\ & - \langle b_n a_m\rangle \sin\omega_n t \cos\omega_m(t+\tau) \\ & + \langle b_n b_m\rangle \sin\omega_n t \sin\omega_m(t+\tau)\Big\}. \end{aligned} \tag{2.7}$$

We impose Eqs. 2.3 - 2.5 on Eq. 2.7, which eliminates the cross-terms $\langle a_n b_m \rangle$ and $\langle b_n a_m \rangle$. Using the trigonometric identity:

$$\sin(\omega_m t)\sin(\omega_m(t+\tau)) + \cos(\omega_m t)\cos(\omega_m(t+\tau)) = \cos(\omega_m \tau), \tag{2.8}$$

it further simplifies to:

$$C_{AB}^{(v)}(\tau) = E^2 \sum_m u_m(\mathbf{r}_A) u_m(\mathbf{r}_B) \cos \omega_m \tau. \tag{2.9}$$

Now, we compare this with the Green's function. The Green's function, represented by normal modes for displacement, is given by:

$$G(\mathbf{r}_A, \mathbf{r}_B, t) = \sum_m \frac{u_m(\mathbf{r}_A) u_m(\mathbf{r}_B)}{\omega_m} \sin(\omega_m t) \times H(t), \tag{2.10}$$

where $u_m(\mathbf{r}_A)$ and $u_m(\mathbf{r}_B)$ are the eigenfunctions of the mode at the excitation point and the observation point, respectively. $H(t)$ is the Heaviside function, which is 0 for t $<$ 0 and 1 for t $>$ 1 and ω is the angular frequency. Now, we calculate the time derivative of Eq. 2.10, leading to:

$$G^{(v)}(\mathbf{r}_A, \mathbf{r}_B, tu) = \sum_m u_m(\mathbf{r}_A) u_m(\mathbf{r}_B) \cos \omega_m t \times H(t). \tag{2.11}$$

If we compare Eq. 2.9 and Eq. 2.11, we notice that they are identical for positive values of the Heaviside function.

The concept of reconstructing Green's functions from ambient seismic noise hinges on the assumption that the noise field is uniformly excited and that the noise sources are statistically independent. This implies that the ambient seismic wavefield should excite all modes equally, either through homogeneously distributed noise sources or strong multiple scattering effects. However, studies indicate that the fundamental mode of Rayleigh waves is most excited in the ambient noise field (Campillo and Paul, 2003; Shapiro and Campillo, 2004; Bensen et al., 2007). When ambient noise recorded at two stations is cross-correlated, the reconstruction of Rayleigh waves is particularly effective, as demonstrated in multiple studies, e.g., Shapiro and Campillo (2004). In contrast, the reconstruction of body waves requires additional processing due to their weaker excitation (Roux et al., 2005; Boué et al., 2013). In all cases, convergence towards the Green's function is increased by using longer data records.

2.3. Applications of Noise Interferometry

After deriving the relation between the cross-correlation of random ambient noise and the Green's function, this section will explore the applications of noise interferometry, with a particular focus on imaging and monitoring subsurface changes.

2.3.1. Surface Wave Imaging

Imaging the Earth's interior is a key objective for many seismologists. Traditionally, body- or surface-wave tomography is performed using data from earthquakes. However, this approach has significant disadvantages, such as sparse and often heterogeneous data coverage, since strong earthquakes primarily occur along active plate boundaries. As demonstrated in the previous section, a new approach has emerged in seismology based on the reconstruction of wavefields from ambient seismic noise. One of the first applications of this approach was surface wave tomography. As described in Chapter 2.1, most sources of ambient noise are concentrated near the surface. As a result, surface modes dominate the ambient noise field, leading to a predominance of surface waves, particularly Rayleigh waves (Toksöz and Lacoss, 1968). In contrast to classical earthquake tomography, the cross-correlations of ambient seismic noise offer several advantages, such as increased spatial coverage due to the growing number of seismic stations. Shapiro et al. (2005) was the first to demonstrate the feasibility of surface wave tomography using ambient noise. Since then, numerous studies have been conducted, ranging from local investigations (Brenguier et al., 2007; Stehly et al., 2009) to continental and even global tomography (Lu et al., 2018; Nishida et al., 2009). The following outlines the workflow for surface wave tomography based on ambient noise.

The reason surface waves are effective for imaging the Earth's crust is their dispersive behavior. Dispersion means that both the phase velocity (c) and the group velocity (U) vary with frequency (see Fig. 2.3a). This allows inference of information from different depths, as lower frequencies sample deeper structures, while higher frequencies are sensitive to shallower layers (Herrmann, 1987; Aki and Richards, 2002). To exploit this property, a two-step approach is traditionally used for ambient noise tomography.

In the *first step*, the dispersion curves are retrieved from the cross-correlation functions. One method, described by Dziewonski et al. (1969) and Herrmann (1973), involves systematically filtering the seismic waveform with a series of narrow-band Gaussian filters and analyzing the arrival times of the dominant energy at different frequencies. This approach effectively maps the wave energy to a frequency-time domain, helping to reveal the dispersion characteristics (see Fig. 2.3b). The advantage of this method lies in its robustness and its potential for automation. Furthermore, it can help identify and separate surface wave modes.

After retrieving the dispersion curves, the first inverse problem is solved to obtain tomographic maps of group velocities for each period (see, e.g., Lu et al., 2018). In general, the inverse problem can be stated as follows (e.g., Snieder and Trampert, 1999):

$$\mathbf{G}\mathbf{m} = \mathbf{d}, \tag{2.12}$$

where $\mathbf{G}$ is the forward operator, $\mathbf{m}$ is the vector of model parameters, and $\mathbf{d}$ is the data vector (observations). The objective is to determine the model that best explains the observations based on a given forward operator, which encapsulates the physical principles underlying the problem. In the context of seismic tomography, the forward operator describes how seismic

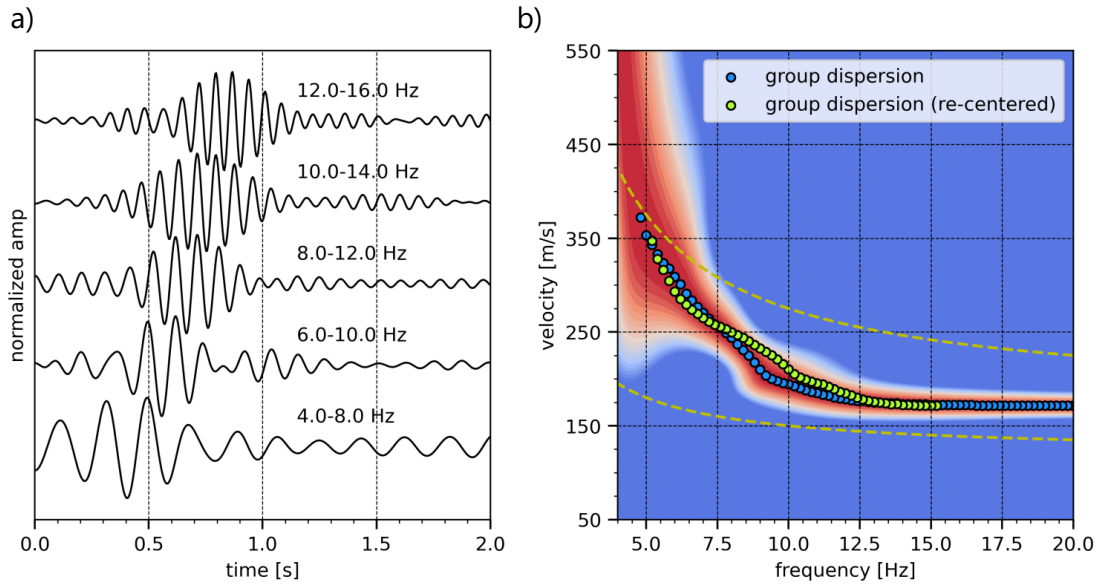


Figure 2.3.: Dispersion analysis. **a)** Surface waves filtered into different frequency bands showing different group velocities. **b)** Dispersion analysis normalized at each frequency. The blue dots show the picked group velocity and the green dots show the dispersion picks after applying the frequency re-centering introduced by Shapiro and Singh (1999) to account for systematic errors of the multiple filter analysis.

waves propagate through the medium and how their travel times are influenced by velocity heterogeneities. An approach to modeling this is the high-frequency approximation of waves (Aki and Richards, 2002). Under this approximation, the travel time t_{ij} of a wave between two stations i and j is given by the integral along the ray path P_{ij}:

$$t_{ij} = \int_{P_{ij}} \frac{ds}{c(s)}, \tag{2.13}$$

where $c(s)$ is the velocity at position s, and ds is an infinitesimal segment along the ray path. If the velocity model is discretized into small grid cells where the velocity is assumed to be constant, the travel time can be approximated as:

$$t_{ij} = \sum_{k} \frac{L_{ij,k}}{c_k}, \tag{2.14}$$

where $L_{ij,k}$ is the length of the ray path within grid cell k, and c_k is the velocity in the k-th grid cell. This equation states that the total travel time between two stations is the sum of the contributions from all the grid cells the wave traverses, weighted by their respective velocity values. Once the forward operator is established, the inverse problem can be solved to determine the model parameters m. Common methods for this include least-squares

approximations. However, in practice, the inverse problem is often ill-posed, meaning that small variations or noise in the data can significantly influence the solution. To address this, several techniques are commonly applied to stabilize the inversion and obtain meaningful results. The most widely used methods include:

- Regularization (e.g., Tikhonov regularization): introduces constraints to stabilize the inversion process and prevent overfitting.
- Singular Value Decomposition (SVD) and pseudo-inversion: mitigates the influence of small singular values that contribute to instability and noise.
- Bayesian methods: incorporates prior knowledge to constrain the solution space and improve inversion robustness.
- Damping of small eigenvalues: filters out noise-sensitive components to enhance solution stability.

Following this, the *second step* is implemented. The objective is to extract the local 1-D velocity profile at each point in the model. These so-called local dispersion curves represent the inverted group or phase velocities for individual frequencies (periods). The final goal is to invert these curves to derive the subsurface structure (see Fig. 2.4).

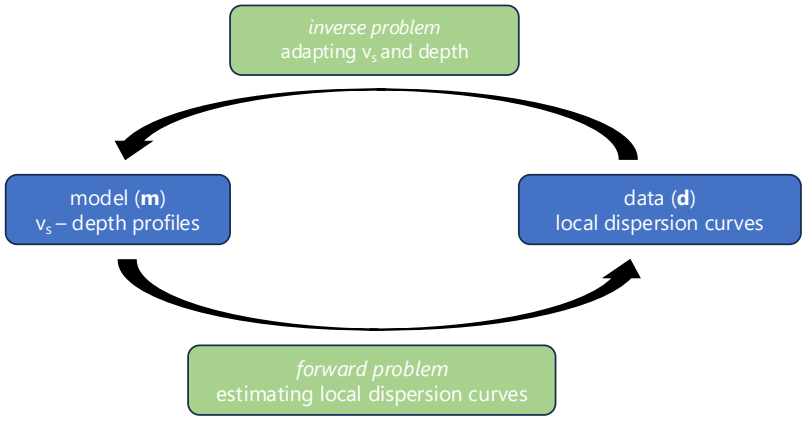


Figure 2.4.: Schematic overview of the inversion procedure. While the procedure is the same for all inverse problems, the examples given are for solving the second step of ambient noise tomography.

The inversion process typically aims to generate a 1-D velocity model that describes the shear-wave velocity (v_s) as a function of depth at each measurement point. Forward modeling is then used to compute the group or phase velocities of surface waves at different frequencies based on the velocity model and layer thicknesses, utilizing surface wave sensitivity kernels. These kernels are derived by computing the partial derivative of velocity with respect to other parameters, such as the shear-wave velocity. The inverse problem seeks to adjust the model

parameters (shear-wave velocities and layer thicknesses) to minimize the misfit between the theoretical dispersion curve and the observed local dispersion curve.

Although most classical ambient noise tomographies follow this two-step approach (e.g., Stehly et al., 2009; Lin and Ritzwoller, 2011; Bodin et al., 2012), recent advancements have introduced new methodologies. Some approaches utilize numerical simulations of the wave equation (e.g., Lu et al., 2020; Nouibat et al., 2023), while others attempt to incorporate full waveform information (e.g., Sager et al., 2020; Tsai et al., 2024). Both methods offer advantages over the traditional two-step approach by accounting for 3D wave propagation effects. However, full waveform inversion relies on amplitude information, which can be influenced by anisotropic noise source distributions and pre-processing steps (Fichtner, 2014, 2015). In addition, these advanced techniques are computationally expensive but continue to benefit from increasing computational power.

2.3.2. Monitoring of Relative Seismic Velocity Changes

The concept of monitoring subsurface changes using seismic wavefields is not new. As early as Poupinet et al. (1984), earthquake doublets, repeating earthquakes with the same location and source mechanism, were used to infer subsurface changes. Additionally, active seismic sources have been employed to study variations in the Earth's crust, as demonstrated by Silver et al. (2007). However, relying on earthquake doublets or active seismic sources is impractical for achieving continuous monitoring of subsurface changes. Continuous observations are crucial for improving our understanding of large earthquakes and identifying possible precursor phases (Ellsworth and Beroza, 1995; Conti et al., 2021). Earthquake events are closely linked to the state of stress in the subsurface. Traditionally, stress estimation has relied on direct point-wise observations, such as strain meters, or has been inferred from geodetic measurements. Both methods have significant limitations in terms of continuous temporal and spatial coverage. An alternative metric that directly reflects changes in the stress field is seismic velocity.

2.3.2.1. Wave Equation from Hooke's Law

This relation is anchored in the theory of elasticity, particularly Hooke's law (see Eq. 2.15), and the stiffness tensor C_{ijkl}, which relates the stress tensor σ to the strain tensor ϵ.

$$\sigma_{ij} = C_{ijkl}\epsilon_{kl}. \tag{2.15}$$

The infinitesimal strain (or deformation) tensor is defined as:

$$\epsilon_{kl} = \frac{1}{2}\left(\frac{\partial u_k}{\partial x_l} + \frac{\partial u_l}{\partial x_k}\right), \tag{2.16}$$

where $\mathbf{u} = (u_1, u_2, u_3)$ is the displacement vector.

Assuming an isotropic medium, the stiffness tensor is characterized by two independent constants, λ and μ (the Lamé parameters). Under this assumption, the stiffness tensor simplifies to:

$$C_{ijkl} = \lambda\delta_{ij}\delta_{kl} + \mu\left(\delta_{ik}\delta_{jl} + \delta_{il}\delta_{jk}\right), \tag{2.17}$$

where δ_{ij} is the Kronecker delta. Consequently, Hooke's law for an isotropic medium becomes:

$$\sigma_{ij} = \left[\lambda\delta_{ij}\delta_{kl} + \mu\left(\delta_{ik}\delta_{jl} + \delta_{il}\delta_{jk}\right)\right]\epsilon_{kl} \tag{2.18}$$

Noting that $\delta_{kl}\epsilon_{kl}$ is the trace of the strain tensor (the sum of its diagonal components), which corresponds to the volumetric strain, $\nabla \cdot \mathbf{u}$. Moreover, the term $\mu\delta_{ik}\delta_{jl}\epsilon_{kl}$ simplifies to $\mu\epsilon_{ij}$, and similarly, $\mu\delta_{il}\delta_{jk}\epsilon_{kl}$ also reduces to $\mu\epsilon_{ij}$. Inserting these results into Eq. 2.18 yields:

$$\sigma_{ij} = \lambda\delta_{ij}(\nabla \cdot \mathbf{u}) + 2\mu\epsilon_{ij}. \tag{2.19}$$

Next, we substitute this relation into Newton's second law, which in index notation is given by (see Eq. 2.20):

$$\rho\frac{\partial^2 u_i}{\partial t^2} = \frac{\partial \sigma_{ij}}{\partial x_j}, \tag{2.20}$$

where ρ is the density. Replacing σ_{ij} using Eq. 2.19 yields:

$$\frac{\partial \sigma_{ij}}{\partial x_j} = \frac{\partial}{\partial x_j}\left(\lambda\delta_{ij}(\nabla \cdot \mathbf{u}) + \mu\left(\frac{\partial u_i}{\partial x_j} + \frac{\partial u_j}{\partial x_i}\right)\right]. \tag{2.21}$$

We now evaluate the derivatives term by term:

$$\frac{\partial}{\partial x_j}\left(\lambda\delta_{ij}(\nabla \cdot \mathbf{u})\right) = \lambda\frac{\partial}{\partial x_i}(\nabla \cdot \mathbf{u}), \tag{2.22}$$

$$\frac{\partial}{\partial x_j}\left(\mu\frac{\partial u_i}{\partial x_j}\right) = \mu\nabla^2 u_i, \tag{2.23}$$

$$\frac{\partial}{\partial x_j}\left(\mu\frac{\partial u_j}{\partial x_i}\right) = \mu\frac{\partial}{\partial x_i}(\nabla \cdot \mathbf{u}). \tag{2.24}$$

Collecting these results, we obtain:

$$\frac{\partial \sigma_{ij}}{\partial x_j} = \lambda\frac{\partial}{\partial x_i}(\nabla \cdot \mathbf{u}) + \mu\nabla^2 u_i + \mu\frac{\partial}{\partial x_i}(\nabla \cdot \mathbf{u}) \tag{2.25}$$

$$= (\lambda + \mu)\frac{\partial}{\partial x_i}(\nabla \cdot \mathbf{u}) + \mu\nabla^2 u_i. \tag{2.26}$$

Substituting Eq. 2.26 back into Eq. 2.20 gives the wave equation:

$$\rho\frac{\partial^2 u_i}{\partial t^2} = (\lambda + \mu)\frac{\partial}{\partial x_i}(\nabla \cdot \mathbf{u}) + \mu\nabla^2 u_i. \tag{2.27}$$

This equation can be separated into compressional and shear components, corresponding to the two independent types of body waves (P-waves and S-waves, respectively). For compressional waves, we define the scalar potential:

$$\phi = \nabla \cdot \mathbf{u}. \tag{2.28}$$

Substituting this into the wave equation and focusing on compressional motion, we obtain:

$$\rho \frac{\partial^2 u_i}{\partial t^2} = (\lambda + \mu) \frac{\partial \phi}{\partial x_i} + \mu \nabla^2 u_i. \tag{2.29}$$

For compressional waves, the following equation holds:

$$\rho \frac{\partial^2 \phi}{\partial t^2} = (\lambda + 2\mu) \nabla^2 \phi. \tag{2.30}$$

which describes compressional (P) waves propagating with velocity:

$$v_p = \sqrt{\frac{\lambda + 2\mu}{\rho}}. \tag{2.31}$$

For shear waves, which are associated with rotational motion, we define the vector potential:

$$\mathbf{\Psi} = \nabla \times \mathbf{u}. \tag{2.32}$$

Substituting this into the wave equation for rotational motion leads to:

$$\rho \frac{\partial^2 \mathbf{\Psi}}{\partial t^2} = \mu \nabla^2 \mathbf{\Psi}, \tag{2.33}$$

indicating that shear (S) waves propagate with velocity:

$$v_s = \sqrt{\frac{\mu}{\rho}}. \tag{2.34}$$

Thus, we have demonstrated that seismic velocities are directly related to the elastic properties and, by extension, to changes in the stress state of the subsurface. This relationship has been supported by various theoretical studies (e.g., O'Connell and Budiansky, 1974; Schoenberg, 1980) as well as experimental investigations (e.g., Birch, 1961; Nur and Simmons, 1969; Nur, 1971; Reasenberg and Aki, 1974; Yamamura et al., 2003; Silver et al., 2007). Consequently, monitoring changes in seismic velocities can serve as a powerful tool for inferring variations in the subsurface stress field.

2.3.2.2. Coda Waves

The following sections discuss the principles of ambient noise monitoring using coda waves. Coda waves were first described by Aki (1969) and are observed following the arrival of body and surface waves generated by earthquakes. They are characterized by their scattered nature, resulting from multiple interactions with heterogeneities in the Earth's crust and upper mantle (Aki, 1969). In noise interferometry, coda waves are also reconstructed when cross-correlating noise records from two seismic sensors. Hennino et al. (2001) demonstrated that coda waves from ambient noise exhibit multiple scattering behavior, making them highly sensitive to small

perturbations in the medium and, therefore, particularly suitable for noise-based monitoring (Snieder et al., 2002). Moreover, as shown by Campillo and Paul (2003) and Shapiro and Campillo (2004), the reconstructed Green's function is dominated by surface waves; thus, it is reasonable to assume that coda waves exhibit properties similar to S-waves due to their dependence on the shear modulus μ.

2.3.2.3. Coda Wave Interferometry

As already mentioned, traditional measurements of seismic velocities rely on specific events or active sources. As a complementary approach, monitoring relative seismic velocity changes has proven to be a suitable tool for detecting small velocity variations based on noise interferometry. The theoretical framework of Coda Wave Interferometry was outlined by Snieder (2006). The following presents one of the key findings regarding velocity perturbation. We begin with the Green's function $G(t, \mathbf{r}, \mathbf{r}_s)$, which describes the wavefield response in a medium. For a constant velocity v, the travel time t_0 along the path P is given by:

$$t_0 = \int_P \frac{ds}{v}, \tag{2.35}$$

where ds is an infinitesimal segment along the ray path. When the velocity changes by δv, the perturbed travel time t' becomes:

$$t' = \int_P \frac{ds}{v + \delta v}. \tag{2.36}$$

A first-order Taylor expansion of $(v + \delta v)^{-1}$ yields:

$$\frac{1}{v + \delta v} \approx \frac{1}{v} - \frac{\delta v}{v^2}, \tag{2.37}$$

which, when substituted into the expression for t', gives:

$$t' \approx \int_P \frac{ds}{v} - \int_P \frac{\delta v}{v^2}\, ds. \tag{2.38}$$

The travel-time perturbation δt is defined as $t' - t_0$ and can be written as:

$$\delta t = t' - t_0 = -\int_P \frac{\delta v}{v^2}\, ds. \tag{2.39}$$

Assuming a homogeneous velocity change, meaning that δv is constant along the path, the expression simplifies to:

$$\delta t = -\frac{\delta v}{v} t_0. \tag{2.40}$$

Rewriting this equation by dividing both sides by t_0 (with t_0 taken as the center time of the examined window of the cross-correlation, which represents the average arrival time of the waves, as justified by Snieder (2006)) yields:

$$\frac{\delta t}{t} = -\frac{\delta v}{v}, \tag{2.41}$$

where t denotes the center time of the window. This result implies that, assuming the perturbation is homogeneous, one can directly retrieve the relative velocity change by measuring the time shift between two cross-correlations. Moreover, it demonstrates that the measurement is independent of the ray path through the medium when using coda wave arrival times.

2.3.2.4. Measuring Relative Seismic Velocity Changes

The theoretical descriptions by Snieder (2006) were later translated into practical approaches for measuring relative seismic velocity changes. The following sections outline and discuss the two most commonly used methods in the time and frequency domains. In general, these techniques are based on comparing a reference state of the medium, hereinafter denoted as ψ_{ref}, with the current state, hereinafter denoted as ψ_{cur}.

The **Time Stretching** method was introduced by Sens-Schönfelder and Wegler (2006) and Lobkis and Weaver (2003). It directly follows the concept proposed by Snieder (2006), which posits that a heterogeneous velocity change in the medium produces a time shift between ψ_{ref} and ψ_{cur}. To quantify the travel time change, and consequently, the velocity change ψ_{cur} is stretched (indicating a velocity decrease) or compressed (indicating a velocity increase) by the factor $t \rightarrow t(1 \pm \varepsilon)$. Next, the perturbed waveform is cross-correlated with ψ_{ref} (after Obermann and Hillers, 2019), resulting in:

$$CC(\varepsilon) = \frac{\int \psi_{\mathsf{ref}}[t]\, \psi_{\mathsf{cur}}[t(1+\varepsilon)]\, dt}{\sqrt{\int \psi^2_{\mathsf{ref}}[t]\, dt \cdot \int \psi^2_{\mathsf{cur}}[t(1+\varepsilon)]\, dt}}. \tag{2.42}$$

To determine the relative seismic velocity changes, a range of stretching factors ε is tested with the aim of maximizing the cross-correlation coefficient CC (see Fig. 2.5). The value of ε that yields the highest correlation corresponds to the relative velocity change of the medium, $\varepsilon = \frac{dv}{v}$.

Another way to estimate the seismic velocity change is the **Moving Window Cross Spectral Analysis (MWCS)**. As already mentioned, Poupinet et al. (1984) and Ratdomopurbo and Poupinet (1995), introduced the so-called doublet method to measure velocity changes from the coda of repeating earthquakes. Nowadays, the technique is also known as MWCS (Clarke et al., 2011). The idea is to measure the time shift between ψ_{ref} and ψ_{cur} in the frequency domain. The time shift is measured along the lapse time of the cross-correlation function (see Fig. 2.6a, b). Within a time window, the phase difference between ψ_{ref} and ψ_{cur} is calculated for different frequencies (see Fig. 2.6c). To do so, the Fourier Transform is calculated for ψ_{ref} and ψ_{cur}. To extract the phase difference, the cross-spectrum:

$$C = \mathcal{F}(\psi_{\mathsf{ref}})\mathcal{F}^*(\psi_{\mathsf{cur}}), \tag{2.43}$$

is computed, where $\mathcal{F}(\psi_{\text{cur}})$ and $\mathcal{F}(\psi_{\text{ref}})$ are the Fourier transforms of the current and reference waveforms, respectively, and $*$ denotes the complex conjugate. The phase differences can be described as:

$$\phi(f) = 2\pi\delta t_i, \tag{2.44}$$

where δt_i is the time-shift between the signals. This can be solved by a linear regression. For every time window, the time-shift is calculated. The relative time-shift $\frac{\delta t}{t}$ itself can again be estimated by a linear regression through zero (see Fig. 2.6d). By applying equation 2.41, the relative seismic velocity change can be retrieved.

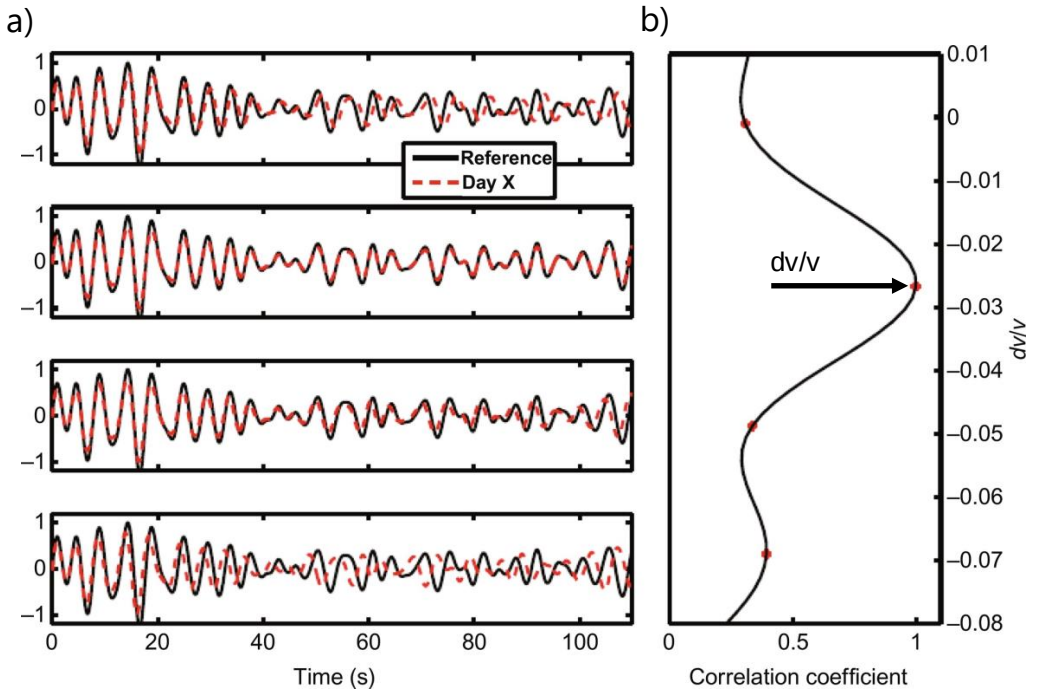


Figure 2.5.: Principle of the stretching method slightly modified after Hadziioannou (2011). **a)** ψ_{ref} is indicated as black line, while the red line is the ψ_{cur}. The different panels show the dilated waveforms for different stretching factors ε. **b)** The correlation coefficient for different values of ε between ψ_{ref} and ψ_{cur}. The black arrow indicates the relative seismic velocity change for this example.

A comparison of the two methods reveals some advantages and disadvantages of each method. In a comprehensive comparison in a laboratory setting, Hadziioannou et al. (2009) worked out that the MWCS analysis is less susceptible to timing errors and amplitude changes and less computationally expensive. Further, Zhan et al. (2013) found that this technique excludes any influence of changes in the noise spectra. Another advantage of the MWCS analysis over the stretching technique is the performance with traces with low signal-to-noise ratio (Mikesell et al., 2015). These numerical tests were further confirmed by studies like those from Hillers

et al. (2015a,b). A contrary observation was made in the laboratory dataset from Hadziioannou et al. (2009). The advantage of the stretching technique is that it allows obtaining smaller changes due to the integration along the coda window (Hadziioannou et al., 2009). While both methods have their advantages, they also show some disadvantages. For instance, the time-stretching method is based on a grid search algorithm, which is computationally slower (Hadziioannou et al., 2009). While the MWCS analysis is faster than the time stretching, the method needs a good understanding of the parameters and is susceptible to overfitting due to the amount of parameters to tune. While both methods work, other approaches have been developed in recent years (Mikesell et al., 2015; Mao et al., 2019b). The choice of method ultimately depends on the user's preference.

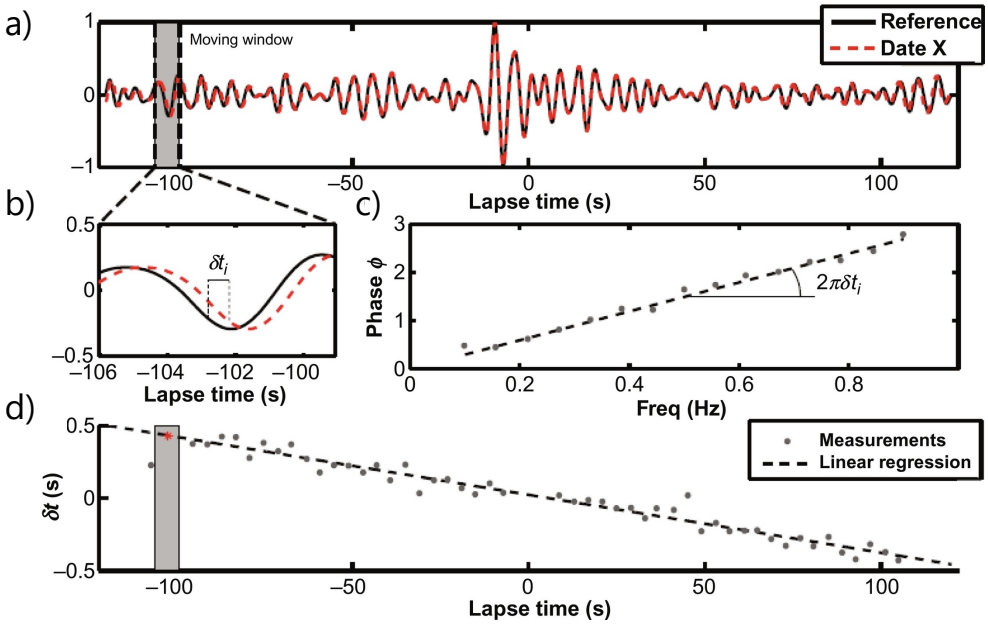


Figure 2.6.: Principle of the Moving Window Cross Spectral analysis slightly modified after Hadziioannou (2011). **a)** ψ_{ref} is indicated as black line, while the red line is the ψ_{cur}. **b)** Zoom into the window marked in **a)**. **c)** The phase for different frequencies of the cross-correlations derived from the cross-spectrum. **d)** Time shifts for different windows along the lapse time. The estimation of $\frac{\delta t}{t}$ with a linear regression is indicated with the dashed line.

2.3.2.5. Origin of Relative Seismic Velocity Changes in the Earth's Crust

Classically, the targets of continuous seismic monitoring were ***tectonic processes*** and ***volcanic activity***. Later, the influence of ***environmental factors*** was found to play a significant role. This section provides a brief review of these aspects.

Ambient noise monitoring in the context of ***tectonic processes*** is closely linked to earthquakes. The primary goal for seismologists remains to predict large earthquakes by understanding precursor and initiation phases (Bouchon et al., 2011). Measuring dv/v during the occurrence of an earthquake reveals consistent features across different case studies. Firstly, a clear co-seismic drop (see Fig. 2.7a) is observed, which is associated with damage in the shallow crust (Brenguier et al., 2008a; Nakata and Snieder, 2011; Ikeda and Tsuji, 2018; Wang et al., 2019). Secondly, after the earthquake, those studies show a long post-seismic relaxation process (see Fig. 2.7a). Studying these relaxation processes can provide important insights into the rheology of the crust (Pollitz, 1992, 2005). However, to date, there is no clear evidence that relative seismic velocity changes show anomalies before large earthquakes. Advancements in machine learning and big data analysis could enhance the capabilities of ambient noise monitoring. However, integrating ambient noise analysis with traditional seismic networks and geodetic observations remains essential to provide a more comprehensive approach to accessing earthquake hazards.

The application of dv/v monitoring related to ***volcanic activity*** is already one step further. As early as Brenguier et al. (2008b), precursory signals were found around two weeks before volcanic eruptions (see Fig. 2.7b). These precursors are associated with the inflation of magma, which leads to a velocity drop and can indicate an impending eruption (Brenguier et al., 2008b; Olivier et al., 2019). Studies monitoring volcanoes typically rely on the fact that the expansion or compression of the volcanic system alters seismic velocities. However, there are processes associated with volcanoes that counteract these changes (Liu et al., 2019). Furthermore, advancements have been made in locating the origin of velocity changes, as demonstrated by Obermann et al. (2013a). While all these studies offer valuable insights into the dynamics of volcanic activity, they suffer from sparse station coverage at certain volcanoes. To obtain more precise and refined results, future efforts should focus on improving station distribution.

Both of the described application scenarios for ambient noise monitoring highlight the importance and potential of this method. However, the time-series of dv/v is also influenced by ***environmental factors*** (e.g., Wang et al., 2017). Some of these factors exhibit strong seasonal variability, such as *precipitation (including snowfall)*, *temperature*, and *atmospheric pressure*. During periods of *precipitation*, the infiltration of water into the subsurface leads to rising pore pressure, which results in a decrease in shear modulus and, consequently, a reduction in seismic velocity (e.g., Sens-Schönfelder and Wegler, 2006; Meier et al., 2010; Tsai, 2011; Wang et al., 2017). *Temperature* fluctuations impact the system in two ways. First, direct heating of the very shallow subsurface leads to changes in rock elasticity and fluid properties (Schoen, 2015). Second, temperature variations induce thermoelastic strain, as described by Berger (1975) or Ben-Zion and Leary (1986), which propagates deeper into the crust (e.g., Richter et al., 2014; Hillers et al., 2015a). Meteorologically linked to *temperature* is *atmospheric pressure*. Several effects change seismic velocities: the direct effect is related to loading and unloading of mass on the Earth's surface, leading to compaction or extension (Silver et al., 2007). Another effect relates to changes in reservoir parameters, such as

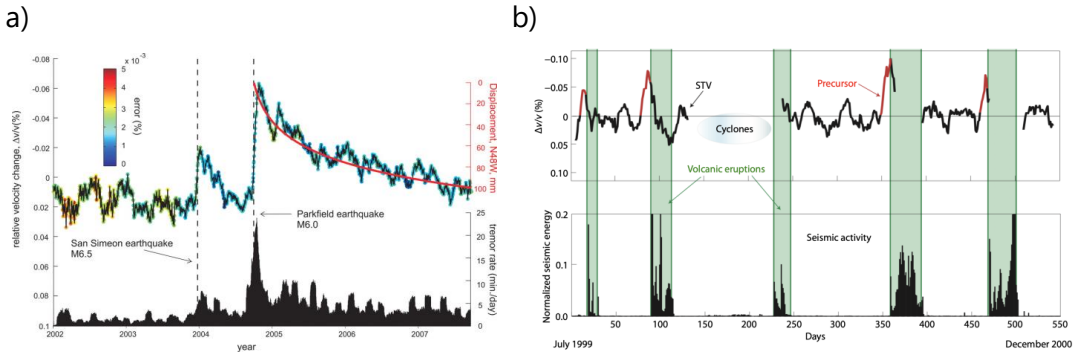


Figure 2.7.: Examples of seismic velocity change monitoring. **a)** Seismic velocity changes, GPS-recorded surface displacements, and tremor activity near Parkfield, California. The red curve indicates postseismic displacements along the San Andreas Fault measured by a GPS station (originally from Brenguier et al., 2008a). **b)** Seismic velocity changes measured at Piton de la Fournaise volcano as well as the seismic energy. The green columns indicating the periods of eruption (figure taken from Wang and Yao, 2020), originally from Brenguier et al., 2008b).

pore pressure, as described in Gradon et al. (2021). Other environmental factors, such as *gravitational forces* exerted by the Sun and Moon, induce minor crustal deformations, causing periodic velocity variations (Yamamura et al., 2003; Takano et al., 2014; Hillers et al., 2015c; Mao et al., 2019a). It is important to note that the subsurface may respond differently to the same environmental forcing depending on the local geology or location. Furthermore, multiple environmental factors could interact and superimpose, generating more complex effects, as seen in phenomena like snowfall (Mordret et al., 2016; Guillemot et al., 2021). As a result, it is crucial to quantify and systematically study these environmental drivers, as demonstrated in, e.g., Wang et al. (2017). The original idea was to remove the unwanted environmental signals from the dv/v time series to highlight small tectonic signals potentially related to earthquakes and their precursor phases or to better understand the pre-eruptive activity of volcanoes. However, it was quickly realized that this "noise" contains valuable information about subsurface processes closely linked to environmental factors.

2.4. Environmental Seismology - A New Set of Applications of Passive Seismic Observations

Before highlighting the importance and applications of environmental seismology, the term should be defined. One definition is given by Larose et al. (2015). They define environmental seismology as the study of natural seismic vibrations generated or influenced by external environmental processes beyond tectonic activity. The field can be divided into two main branches:

- Analysis of seismic sources induced by the atmosphere, hydrosphere and cryosphere, including storms, river dynamics, glacial movement and oceanic activity.
- Investigate how seismic wave propagation within the solid Earth is affected by environmental factors such as temperature variations or hydrological changes.

In general, this interdisciplinary field uses seismic techniques to gain insights into Earth system interactions and to monitor environmental changes that were previously inaccessible through conventional seismology.
The first part of this section deals with environmental seismic sources and what we can learn from them. This is followed by the aspect of monitoring environmental change using ambient noise. Special attention is later given to the monitoring of hydrological processes.

2.4.1. Environmental Seismic Sources

The study of environmental seismic sources provides valuable information on ice dynamics, slope stability, and atmospheric events, with important implications for natural hazard assessment and climate studies.

In the context of global warming and the extensive loss of glacier ice, the sub-discipline of cryoseismology has emerged. One of the most common sources of cryoseismic activity are icequakes (Podolskiy and Walter, 2016; Aster and Winberry, 2017; Montagner et al., 2020). These seismic events are generated by the fracturing of glacier ice, stick-slip motion, or the sudden movement of ice masses, such as iceberg calving (Montagner et al., 2020 and references therein). Their distinctive signatures offer insights into glacier dynamics and ice loss. For instance, studies by Canassy et al. (2016) have reported seasonal variations in icequake activity associated with different patterns of glacier motion, while other investigations have linked changes in icequake activity to melting events and overall ice loss (Köhler et al., 2015; Montagner et al., 2020). These observations are critical for understanding glacier responses to climate change and for predicting potential surges or collapses.

Another environmental seismic source that exhibits clear changes due to climate change is ocean activity (Aster et al., 2023). Due to the coupling between ocean waves and the seafloor (see section 2.1), it is possible to track storm activity using seismometers. Such analyses reveal an increase in the frequency of storms such as hurricanes or typhoons (Montagner et al., 2020). Moreover, it has been shown that these storm-generated seismic signals can be used to track storm dynamics (Gerstoft and Bromirski, 2016; Retailleau and Gualtieri, 2019, 2021) and potentially improve forecasting. The integration of seismic data with meteorological observations enables a more comprehensive understanding of the processes driving severe weather events.

These two sources are explicitly highlighted because they allow us to draw conclusions about the current state of our environment. Other sources include the seismic signatures of river flooding (Gonzalez et al., 2023) and landslides (Weichert et al., 1994). Together, these

examples illustrate that environmental seismic sources, whether arising from the cryosphere, hydrosphere, or atmosphere, offer a rich dataset for understanding Earth dynamics. By analyzing these signals, it is possible to monitor changes in ice mass, assess landslide risk, and track storm activity, thereby contributing to a more holistic understanding of natural hazards and environmental change.

2.4.2. Monitoring Earth's Environment

Just as changes in noise sources can reveal environmental variations, monitoring Earth's surface processes is a vital tool, given that many of these processes have critical implications for natural hazards, resilience against climate change, and resource management. In the following some examples of recent developments are presented. This list does not claim to be complete, especially due to the rapid development of this discipline in recent years.

One of the most significant natural hazards are landslides. They are posing risks to infrastructure and environment. Landslides can occur suddenly or gradually, and their triggering mechanisms often involve complex interactions between geological, hydrological, and climatic factors (Mainsant et al., 2012; Voisin et al., 2016; Bontemps et al., 2020). This complexity makes them difficult to predict, but understanding these processes is essential for developing effective early warning systems and mitigation strategies. Noise monitoring seems to be a promising tool in untangling these drivers. Mainsant et al. (2012) was one of the first studies to show that changes of relative seismic velocity changes could serve as precursors to landslide events by reflecting variations in rigidity before landslide failure. Building on this, Voisin et al. (2016) analyzed data from a network of seismometers on a landslide. Their work revealed that fluctuations in seismic velocity are connected to the water table below the landslide and its changes due to rainfall. More recently, Bontemps et al. (2020) integrated ambient noise analysis with conventional geotechnical measurements to examine the long-term evolution of landslide behavior. This study demonstrated that ambient noise monitoring can capture both gradual deformation processes and abrupt changes in slope dynamics, which are crucial for developing effective early warning systems and advancing our understanding of landslide mechanics (Le Breton et al., 2021).

An example for a fast changing environment under the influence of global warming are regions of permafrost. Permafrost refers to any ground that remains continuously below 0 °C for at least two years (Subcommittee Permafrost, 1988). Ambient noise monitoring has emerged as a powerful tool for tracking permafrost dynamics, offering continuous and non-invasive measurements of frozen ground properties. For instance, James et al. (2019) demonstrated that ambient noise techniques can effectively capture the seasonal evolution of permafrost, revealing changes in elastic properties that correspond to freeze-thaw cycles. Similarly, Lindner et al. (2021) employed these methods to monitor variations in the mechanical behavior of permafrost in an alpine environment, providing insights into thaw-induced softening and related deformation processes. Albaric et al. (2021) further advanced this approach by integrating ambient noise monitoring with complementary geophysical measurements to map the temporal evolution of permafrost degradation over multiple years. The thawing of permafrost comes

with certain risks. Permafrost stores a large amount of methane (Knoblauch et al., 2018) a greenhouse gas contributing to global warming (Lashof and Ahuja, 1990; Boucher et al., 2009). Further, thawing of permafrost could lead to destruction of human infrastructure (Hjort et al., 2022) as well as higher risks of rockfalls in alpine regions (Gruber et al., 2004). But, permafrost loss not only alters local hydrology and ground stability but may also trigger the formation of quick clay (Bruland et al., 2025). As permafrost thaws, the previously frozen, clay-rich sediments can destabilize and transform into quick clay, a metastable material highly susceptible to liquefaction (Okamoto et al., 2004; Khaldoun et al., 2009). Monitoring permafrost with ambient noise thus offers an early warning mechanism for potential quick clay hazards, contributing significantly to risk assessments (Bruland et al., 2025).

These are only two examples of how ambient noise monitoring can help understanding environmental geohazards and changing environmental conditions. Further applications in understanding geohazards include understanding environmental-triggered earthquakes (Wang et al., 2024b) or influences on volcanic activity (Yates et al., 2024).

One rapidly developing aspect of environmental seismology is the monitoring of hydrological processes. Monitoring the hydrosphere and employ sustainable water management strategies will become crucial in the next decades due to higher frequencies of droughts, as well as continuous growth of population and industry (Megdal, 2018; Mukherjee et al., 2018). Already Sens-Schönfelder and Wegler (2006) were able to link changes in the seismic velocities to precipitation rates and changes in the groundwater table. It took some time until the community came back to this approach. In the following chapters, the need for modern and innovative monitoring methods for water resources is elaborated.

2.5. Aquifers under the Influence of Global Warming

Aquifers hold the largest volume of liquid freshwater on Earth (Gleick, 1996). However, due to global warming, population growth, and the increasing demand from industrial and agricultural activities, these vital resources are experiencing a significant decline (e.g., Wada et al., 2010; Megdal, 2018).

World population has grown exponentially, currently standing at around 8 billion people (United Nations, 2025). This growth has intensified pressure on natural resources, particularly freshwater. Expanding urban centers, industrialization, and intensive agricultural practices have significantly increased water consumption. Agriculture alone accounts for approximately 70 % of global freshwater withdrawals, primarily for irrigation (Food and Agriculture Organization of the United Nations (FAO), 2021). Additionally, industrial processes, including energy production, manufacturing, and mining, require vast amounts of water, further straining aquifers and surface water sources. Over-extraction of groundwater to meet these rising demands has led to aquifer depletion, land subsidence, and water quality degradation in many regions (Bouwer, 1977; Wada et al., 2010; Gleeson et al., 2012; du Plessis, 2022; Shi et al., 2024). In some cases, groundwater recharge cannot keep pace with extraction rates,

making many aquifers non-renewable on human timescales (Tiwari et al., 2009; Syed et al., 2009). Climate change aggravated these challenges by altering precipitation patterns, reducing snowpack, and increasing evaporation rates, further stressing water availability (Wu et al., 2020; Dharmarathne et al., 2024). A summary of these effects can be seen in Fig. 2.8.

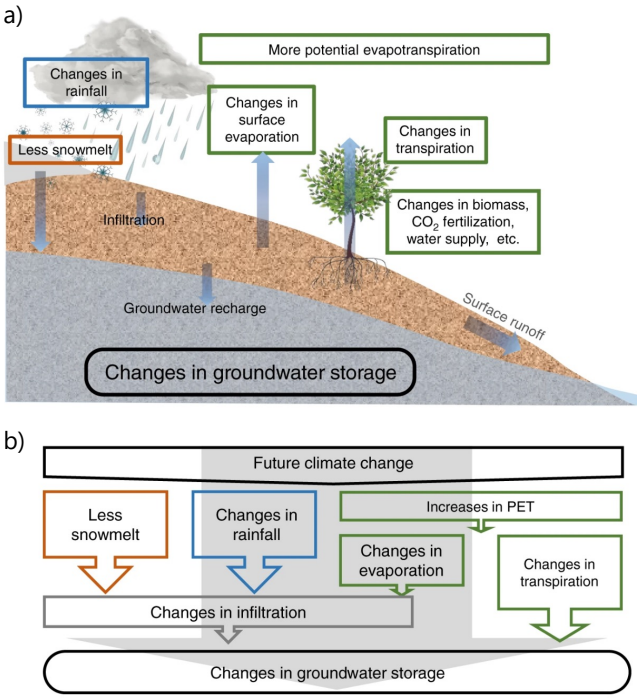


Figure 2.8.: Sketch of hydrological processes on land. **a)** Factors which contribute to the water budget and cycle. **b)** Summary of factors controlling groundwater responses. (Figure from Wu et al. (2020) with slight modifications.)

Climate change refers to long-term shifts in temperature and weather patterns (Demeritt, 2001). While natural factors, such as variations in the solar cycle, have historically driven climate fluctuations, leading to glacial and interglacial cycles (Petit et al., 1999), since the 1800s, human activities have become the dominant driver of global climate change. Sectors such as energy production, industry, transportation, and land-use changes have significantly contributed to greenhouse gas emissions, primarily through the combustion of fossil fuels like coal, oil, and gas (IPCC, 2021). An increase in the concentration of greenhouse gases, like carbon dioxide (CO_2) or methan (CH_4) leads to the so-called greenhouse effect. As a direct consequence less infrared radiation is reflected back into space leading to global temperature increases. According to the Intergovernmental Panel on Climate Change (IPCC) temperatures could rise between 1.5°C to 4.5°C above pre-industrial levels (IPCC, 2021). This rise in temperature accelerates terrestrial evaporation (Berg et al., 2016; Short Gianotti et al., 2020), thereby reducing the amount of water available to replenish aquifers. Additionally this

will lead to a reduction of available soil moisture providing crucial water in the critical zone, e.g., for plants to grow (Berg and Sheffield, 2018). This altering in the soil condition could further influence infiltration into shallow aquifers (Taylor et al., 2013). While surface water resources show a quick response to changes in e.g. precipitation patterns response in aquifers can be delayed and might be only visible after extensive dry periods (droughts) (Hetzel et al., 2008). Although the impact of climate change on surface water is well known, there is a lack of understanding about the deeper water resources (Erler et al., 2019). Knowledge about this is crucial to implement long-term sustainable groundwater management strategies. To achieve this goal a comprehensive understanding of aquifers, their properties and vulnerability is imperative.

2.5.1. Traditional Monitoring of Aquifers

Monitoring aquifers is essential for effective water resource management and understanding the evolution of groundwater systems, yet traditional monitoring methods often suffer from incomplete spatial coverage or infrequent measurements (Wada et al., 2010; Taylor et al., 2013). In general, aquifer monitoring relies on three primary approaches:

1. The most common method involves direct measurements of groundwater levels using piezometers installed in boreholes (Taylor and Alley, 2001). These devices record the hydraulic head, the pressure exerted by the water above a defined vertical reference point. Although such point measurements yield accurate data on local water levels, they are inherently spatially limited, which is a disadvantage given the heterogeneity of aquifers (Wang et al., 2024a). Further drilling observational wells could lead to a negative interference with the ecological system (Jones et al., 2015).

2. Recent advances in satellite remote sensing have introduced methods such as the GRACE (Gravity Recovery and Climate Experiment) mission, which tracks changes in Earth's gravity field to estimate large-scale groundwater storage variations (e.g. Rodell and Famiglietti, 2002; Castellazzi et al., 2016). However, GRACE's coarse spatial (approximately 100 km) and temporal (monthly) resolution limits its effectiveness for smaller aquifers. Alternatively, ground-based techniques, such as GNSS (e.g. King et al., 2007; Ji and Herring, 2012; Young et al., 2024) and InSAR (e.g. Bell et al., 2008; Chaussard et al., 2014; Rezaei and Mousavi, 2019), offer higher resolution in time and space than e.g., the GRACE mission. Nevertheless, both methods have some disadvantages, especially the interpretation of the data is not always straightforward and a superposition of multiple effects (e.g. Larson et al., 2008; Saji et al., 2020). In addition, the typically lower temporal resolution of this measurements can miss changes in aquifer conditions, making it difficult to capture the dynamic behavior of groundwater systems.

3. To account for both resolution in time and space multiple geophysical methods are employed to image and characterize aquifer properties. Methods that exploit the electrical and magnetic properties of near-surface materials, such as induced polarization, self-potential, electromagnetic induction, and ground-penetrating radar, offer high spatial

resolution and provide insights into subsurface lithology and moisture content (e.g. Rubin and Hubbard, 2006; Vereecken et al., 2006; Robinson et al., 2008). Seismic methods, including reflection and refraction surveys, also contribute to aquifer characterization. Seismic reflection, for instance, produces detailed images of subsurface stratigraphy and can reveal the geometry of aquifer systems, although it is mainly used to identify layer boundaries rather than to quantify hydrological properties (Binley et al., 2015). Seismic refraction, on the other hand, can efficiently estimate water table depths and assess the presence of fluids by analyzing compressional and shear wave velocities (e.g Haeni, 1986; Galibert, 2016).

While each of these traditional methods offers valuable insights, they also exhibit significant limitations, whether in spatial extent, temporal resolution, or cost. Point measurements and local geophysical surveys provide detailed information but are inherently site-specific and often sparse. Large-scale satellite monitoring captures broader trends but lacks fine detail. Given the increasing stresses on groundwater resources due to climate change, population growth, and intensified industrial and agricultural activities, an integrated, continuous monitoring approach is essential for sustainable water management and effective pollution mitigation.

2.5.2. Monitoring Earth's Hydrosphere Using Ambient Seismic Noise

As already elaborated, hydrological processes play a crucial role in shaping the Earth's surface, affecting groundwater flow, water table dynamics, and surface water distribution (Fan et al., 2019). While other geophysical methods are reliable and well established tools for probing the hydrosphere (Rubin and Hubbard, 2006) the use of ambient seismic noise monitoring is relatively new. However, the increasing use of ambient seismic noise has provided new insights into subsurface water flow, aquifer changes, and seasonal hydrological variations.

The first study highlighting the capabilities of ambient noise monitoring was by Sens-Schönfelder and Wegler (2006), it marked a breakthrough in using seismic interferometry to detect small velocity variations in the subsurface and relate them to variations in soil moisture and water table fluctuations. This laid the foundation for applying ambient noise techniques to hydrological monitoring.

Subsequent studies, such as those by Lecocq et al. (2014), built on these concepts further by explicitly linking seasonal variations in groundwater levels to observable changes in seismic velocities. Lecocq et al. (2014) linked the observed long-term changes in dv/v to hydrological, primarily pore pressure, and thermo-elastic pressure changes underneath the Graefenberg array (Germany). This work not only established a quantitative relationship between dv/v and groundwater head but also proposed a method to estimate aquifer recharge rates.

This approach was further refined in a series of investigations by Voisin et al. (2016, 2017). Unlike Lecocq et al. (2014), they linked changes in seismic velocities to different saturation states through oscillating groundwater tables. Furthermore, Voisin et al. (2017) first

demonstrated the application of passive seismic monitoring in active hydraulic experiments by monitoring the created hydraulic dome, which acts as a barrier in the event of pollution in the drinking water supply reservoir. This potential was further explored by Gaubert-Bastide et al. (2022). In their investigation of these hydraulic barriers, they employed dv/v monitoring to assess their effectiveness by continuously recording seismic velocity changes before, during and after filling the basin, which led to the installation of these barriers. By inverting the obtained changes in dv/v, they found a strong correlation, demonstrating the effectiveness of this monitoring tool. Both studies (Voisin et al., 2017; Gaubert-Bastide et al., 2022) demonstrated that dv/v monitoring could serve as a valuable tool in both passive observational studies and active hydrological experiments where immediate operational decisions are required.

Shortly after the work by Voisin et al. (2017) the work of Clements and Denolle (2018) reinforced the practical applicability of dv/v demonstrating a direct relationship between changes in seismic velocity and variations in the groundwater table. Their study quantified the magnitude of the responses of dv/v to the depletion of the groundwater table, providing a practical framework for using seismic monitoring in aquifer management by estimating water loss. The clear correlation established in their work has been pivotal in validating dv/v as a proxy for hydrological activity, inspiring subsequent investigations into the dynamic behaviour of subsurface water storage.

Building on these methodological advancements, Rodríguez Tribaldos and Ajo-Franklin (2021) expanded the application of dv/v techniques to distributed acoustic sensing (DAS) measurements. As well as linking changes in pore pressure to observed changes in seismic velocity, they also discuss other potential mechanisms that cause velocity changes, such as water-air substitution above the water table and in the capillary fringe. However, due to the lack of sensitivity of the measurements to this depth range, they ruled out these mechanisms by providing some depth constraints through inversion of a velocity-depth profile. Building on these developments, Sobolevskaia et al. (2024) later used ballistic waves reconstructed from DAS measurements to monitor water level variations in an aquifer. This approach provided data with high spatial and temporal resolution. This study further demonstrated the potential of DAS-based methods for hydrological monitoring.

The contributions of Illien et al. (2021, 2022) further extended the capabilities of dv/v monitoring by investigating its use in alpine environments. Their work focused on the influence of seasonal water infiltration on seismic velocity variations, demonstrating how this information could be used to improve our understanding of critical freshwater reserves in mountainous regions. Illien et al. (2021) demonstrated that dv/v monitoring could be used effectively to track hydrological processes in high-altitude regions where direct groundwater measurements are often impractical. These insights have significant implications for water management applications in these regions.

In recent years, methodological improvements have been driven by theoretical advancements in the understanding of coda wave sensitivity kernels. Mao et al. (2022) introduced a space-time

monitoring approach for groundwater fluctuations using passive seismic interferometry. Focusing on the Los Angeles Basin, her study linked dv/v variations to different district depletion rates, highlighting spatial heterogeneity in groundwater extraction patterns. By correlating the dv/v signals with known depletion practices, the study provided valuable insights into the influence of urban water management on subsurface dynamics, demonstrating the effectiveness of seismic monitoring in large-scale hydrological studies.

The contributions of Delouche and Stehly (2023) further refined the methodological landscape by monitoring seasonal seismic velocity variations in Greece to understand aquifer dynamics. Their findings revealed that seasonal velocity variations are influenced by both natural recharge events and anthropogenic groundwater extraction. These results provided new insights and strengthened the case for using dv/v monitoring as a valuable tool in water resource management.

Similarly, Shen et al. (2024) has contributed to the expanding frontier of dv/v monitoring by focusing on fiber optic sensing techniques to track soil moisture dynamics in the vadose zone. This study uses DAS to capture high-resolution spatiotemporal variations in soil moisture. By integrating fiber optic sensing with dv/v methodologies, Shen et al. (2024) opened up new avenues for investigating vadose zone hydrology and improved our ability to monitor infiltration processes, evaporation rates, and subsurface water retention. This novel approach increases the potential for dv/v-based studies to contribute to precision agriculture, early drought detection, and sustainable groundwater management. Together, these studies demonstrate a clear trajectory of innovation, from the initial development of ambient noise methods to the sophisticated techniques that have emerged in recent years.

Despite the advantages of the methods, such as providing spatial and temporal monitoring of the hydrosphere and potentially bridging the gap of point-wise hydrological well measurements, there are still some uncertainties and limitations. Similar to GPS or InSAR methods, seismic velocity changes are a complex overlay of multiple factors (e.g., temperature or stress changes). Furthermore, hydrological properties are non-uniform across regions, and seismic signals can be influenced by complex geological structures. This makes interpreting results in regions with complex subsurface conditions difficult. A similar issue arises from the complex depth-sensitivity kernels of coda waves. Localizing the origin of velocity changes can be challenging and lead to complex interpretations. As discussed in the review, multiple studies suggest different mechanisms driving changes in seismic velocities. Changes in seismic velocity can correspond to various hydrological phenomena, including water infiltration, pore pressure changes, and saturation levels. However, similar velocity variations can result from different physical processes, making it difficult to correlate specific dv/v changes with particular hydrological events. Furthermore, accurately interpreting dv/v variations in hydrological terms (e.g., water content or pore pressure) often requires calibration with direct hydrological measurements (e.g., groundwater level data or precipitation records). The difficulty of establishing clear relationships between seismic velocities and hydrological parameters can make calibration challenging. Lastly, these obstacles currently prevent us from providing interpretable results for

hydrologists. Thus, improving the sensitivity, spatial resolution, and temporal accuracy of these methods, enhancing data processing techniques, and developing better calibration approaches are critical areas for future research. Additionally, integrating ambient noise methods more directly with hydrological models and multidisciplinary data will make them a more robust tool for hydrological monitoring in diverse environments.

2.6. Concluding Remarks

This chapter has reviewed the main methods and advancements in ambient and environmental seismology. It presents the tools and studies that form the basis of this thesis. This section provides context for the current state of research and discusses the advancements that will be made in this thesis.

Despite recent advances in understanding the influence of environmental effects on seismic velocities, seismology has only recently begun to discuss and understand them. Despite increasing recognition that environmental factors such as temperature, precipitation, air pressure, and snow cover significantly affect seismic velocities, seismology as a discipline has been slow to integrate these effects into both data interpretation and theoretical frameworks. Historically, such effects have been treated as noise to be filtered or averaged out, rather than as signals worthy of scientific investigation in their own right. This view is gradually changing, but our understanding remains fragmented and largely qualitative.

One of the key challenges is the interdisciplinary nature of the problem. Environmental perturbations affect seismic velocities through various coupled physical processes, such as thermoelastic expansion, poroelastic deformation, fluid saturation, and freeze-thaw transitions in the shallow subsurface. These mechanisms vary with depth, material properties, and site-specific conditions. Their combined effects are difficult to disentangle without targeted experiments or simultaneous environmental monitoring. Consequently, many studies remain descriptive, highlighting correlations without resolving causality or providing transferable models.

Meanwhile, disciplines like gravimetry, InSAR, and GNSS have made substantial progress in accounting for environmental and atmospheric effects, often correcting signals with remarkable precision (e.g., Bevis et al., 1992; Crossley et al., 1995; Rosen et al., 1996; Larson et al., 2008; Hanssen, 2001; Van Camp et al., 2017). In contrast, ambient noise seismology has only recently begun to shift its perspective on environmental influences. Rather than viewing them as unwanted signal overprinting, e.g., tectonic signals, seismologists now use these influences as probes of near-surface processes. Yet, herein lies the opportunity. Seismology is uniquely sensitive to mechanical properties in the near surface and has the potential to become a leading tool in environmental sensing if we rise to the challenge. Continuous cross-correlation workflows allow us to track how freeze-thaw cycles, rainfall-driven saturation, and barometric pressure oscillations alter seismic velocities. This provides new insights into near-surface diffusivity, hydrology, seasonal permafrost dynamics, and more. By learning from

and adapting the rigorous environmental characterization methods of ultrasonics, GNSS, meteorology, gravimetry, and InSAR, we can not only remove these influences from the time series but also interpret velocity perturbations as valuable signals of subsurface environmental change.

The following chapters 3 and 4 aim to push for such applications of better understanding environmental influences on seismic velocities and use the gained knowledge for an innovative approach in environmental monitoring.

Chapter 2.5.1 also outlined the need for innovative methods in monitoring the Earth's hydrosphere. Although ambient noise monitoring has shown promising potential for detecting and monitoring hydrological processes, such as changes in groundwater levels, soil moisture, or snow loading, it remains a relatively new and experimental tool in the context of hydrology. The physical link between hydrological parameters and seismic velocity changes, while conceptually well established, remains poorly constrained in terms of quantitative interpretation. Key mechanisms such as pore pressure variations, saturation-dependent elastic moduli, and thermoelastic coupling are often entangled and difficult to isolate, especially under field conditions where multiple environmental variables interact.

A major limitation is the lack of ground truth data with the necessary spatial and temporal resolution to calibrate seismic observations. Although changes in travel time or velocity can be correlated with rainfall events or seasonal recharge, determining absolute changes in hydrologic parameters (e.g., volumetric water content) remains challenging without additional measurements, such as those from soil moisture probes or piezometers. Additionally, site-specific effects, such as lithology or topography can significantly impact the seismic response to hydrological changes, limiting the applicability of the results to other regions.

To fully realize this potential, the field must progress from proof-of-concept studies to long-term, site-specific deployments with robust validation datasets. Only then will ambient noise monitoring become a routine and reliable component of hydrological observation systems.

Chapter 5 tries to enrich the landscape of monitoring hydrological processes using ambient noise by inferring spatio-temporal contraints in a controlled setting to build a foundation for future studies.

Together, this thesis explores novel concepts of monitoring and imaging with ambient noise to gain deeper insights into the hydrosphere. Through the use of ambient noise interferometry and advanced signal processing techniques, we seek to unveil the dynamics of groundwater systems and their interactions with surface processes. These innovative approaches are ultimately expected to enhance our understanding of subsurface hydrological processes. These advancements have the potential to inform sustainable groundwater management strategies and address the urgent issues of water scarcity and resource depletion in the context of climate change and increasing human demand.

3 Interaction of Air Pressure and Groundwater as Main Cause of Sub-Daily Relative Seismic Velocity Changes

Abstract

Our study investigates variations of seismic velocity that occur over short time scales of hours. We use coda wave interferometry to inspect 5 months of continuous data from a seismological array in southern Germany. This results in relative seismic velocities (dv/v) that show temporal variations on the order of 10^{-4}. Spectra of the velocity time series contain strong daily and sub-daily behavior indicating that the daily and sub-daily changes in the seismic velocity are primarily caused by atmospheric tides. We also note the influence of temperature changes on daily variations, but as a second-order effect. The explanatory model focuses on depth variations of the groundwater table, linking atmospheric pressure (loading and deloading the Earth's surface) to variations in seismic velocity. Our results highlight an important environmental influence on seismic velocity that needs to be considered before seismic velocity variations can be used for inspecting fluid and stress variations in situ.

Key Points

- We observe strong daily and sub-daily variations of seismic velocity using coda wave interferometry
- The effect is caused predominantly by the coupling of atmospheric pressure and groundwater table variations
- The coupling allows a better understanding of crustal deformation and suggests novel techniques for characterizing aquifer systems

Plain Language Summary

Geological and environmental effects manifest themselves in changes of crustal properties, and we record these as variations of seismic wave velocity. This is especially the case for seismic waves that travel within the Earth's crust. Changes in tectonic stress are particularly interesting, since they can cause earthquakes. We would also like to know more about changes in fluid content in the crust at the various depth levels. Both tectonic stress and fluid content affect seismic velocity, but environmental factors also have an effect and these need to be taken into account. This study shows that the interaction of air pressure and groundwater, has considerable influence on measured daily velocity variations. This opens important possibilities in itself. On the other hand, we can remove these pressure effects from the velocity changes, to highlight changes due to tectonic effects, such as earthquakes.

3.1. Introduction

The research toward understanding large earthquakes' generation and precursor phases is still in process (Conti et al., 2021; Ellsworth and Beroza, 1995). A key parameter to better understand the temporal component of these processes is the changing strain and stress within Earth's crust. The elastic moduli of the rocks directly link these variations to seismic velocity changes. By knowing this relationship, measuring changes of seismic velocity provides insight into the temporal evolution of strain in the subsurface. However, this relationship is disturbed by the influence of environmental effects, for example, temperature, precipitation (Hillers et al., 2015a; Richter et al., 2014; Sens-Schönfelder and Wegler, 2006; Wang et al., 2017). Collecting information about time-varying environmental processes perturbing Earth's crust is thus essential to reveal crustal deformation associated with tectonics.

The classical approaches to probe this behavior, which have used active seismic experiments (Niu et al., 2008; Yamamura et al., 2003) are increasingly replaced by monitoring using seismic ambient noise and the concept of coda wave interferometry. In the first step, the long-term influence of environmental effects was discussed (Gradon et al., 2021; Richter et al., 2014; Sens-Schönfelder and Wegler, 2006). Also, the strong imprint of groundwater level changes is widely discussed and described (Clements and Denolle, 2018; Gassenmeier et al., 2014). Recent years have shown a trend toward high temporal resolution monitoring (Mao et al., 2019a; Oakley et al., 2021; Sens-Schönfelder and Eulenfeld, 2019). These studies show that environmental effects such as daily temperature changes (Mao et al., 2019a; Oakley et al., 2021) and tidal stress (Mao et al., 2019a; Sens-Schönfelder and Eulenfeld, 2019) substantially impact seismic velocities. However, in contrast to long-term studies, the influence of daily groundwater table changes or atmospheric pressure variations is merely discussed.

In this study, we fill this gap by investigating data from a highly sensitive array in southern Germany, which is far away from potential local disturbances, such as cities or roads. We calculate an hourly dv/v value for high temporal resolution monitoring. Our measurements show that the seismic velocities have daily and sub-daily periodicity which may be forced by the repetitive loading and unloading of the Earth's surface due to the atmospheric pressure changes and thermal effects. This coupling of atmospheric pressure and seismic velocity provides insight into the behavior of aquifers in the near-surface region, and it might give rise to a range of new seismic applications for groundwater purposes.

3.2. Data and Methods

3.2.1. GERES Array

We use seismic data from the GERES (German Experimental Seismic System) array (Harjes, 1990). GERES is part of the global network of seismic stations for the Comprehensive Nuclear-Test-Ban Treaty Organization (CTBTO), providing a long continuous data set over several years. The GERES array is located in the Bavarian Forest in South East Bavaria, close to the

borders with the Czech Republic and Austria (see Figure 5.1a).

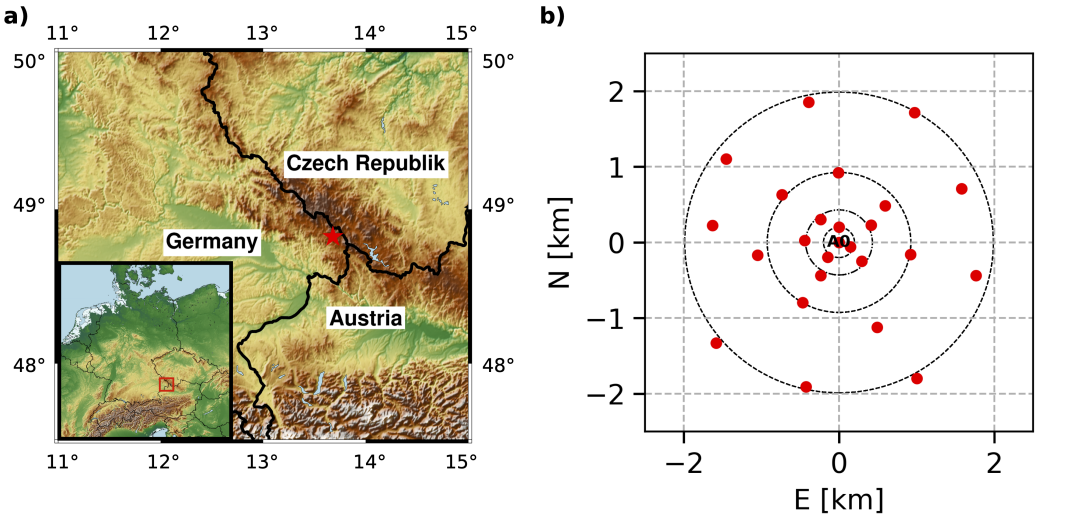


Figure 3.1.: (a) Location of the German Experimental Seismic System (GERES) array within Germany (inset). The zoom provides a more detailed overview of the topography of the region. (b) Configuration of the GERES array. The red dots indicate the position of the short-period seismometer GS-13.

It consists of 25 vertical short-period seismometers (GS-13 seismometers, typically 1 Hz corner frequency, 40 Hz sampling frequency). The seismometers are installed in 3–5 m depth holes on four concentric circles around the center station A0 (see Figure 3.1b). The circles' minimum and maximum radii are 200 and 1,988 m, respectively, which corresponds to a maximum aperture of around 4 km. Due to the emplacement in holes, the seismometers are directly coupled to the granitic bedrock (Haidmühler granite). This type of emplacement ensures that the seis- mometers are not directly affected by environmental effects, for example, wind and air pressure changes. GERES is thus one of the most sensitive seismic arrays in central Europe (Harjes, 1990), with particularly high data quality. Beside this, GERES is located in a low-noise area, in a forest far away from particular noise sources, such as coastal lines, lakes or big cities. We use the GERES array to perform a monitoring of the subsurface properties with high temporal (hourly) sampling, for frequencies up to 10 Hz. For our investigation, we used 5 months of continuous data from January to June 2014. As additional data sets, we use the meteorological measurements from the close-by infrasound array I26DE, which provides temperature and atmospheric pressure measurements.

3.2.2. Monitoring Seismic Velocity

Our seismic monitoring is based on ambient seismic noise, from which we estimate the Green's function by calculating the cross-correlation function of the noise recorded at two stations (Shapiro and Campillo, 2004). The Green's function represents the seismic impulse response

of a medium to a point source at one station, recorded at the other. To monitor changes in the subsurface, we then use the technique of coda wave interferometry (Snieder et al., 2002). This concept, based on scattered coda waves, shows its advantage in capturing small changes in the probed medium's elastic properties (Poupinet et al., 1984). The technique can be seen as probing a given volume in the subsurface repeatedly over time (Snieder et al., 2002). We use this to calculate differences in the coda waves' arrival time (dt/t) over the investigation period and transform this into a relative seismic velocity change (dv/v). Our workflow starts with a continuous record of ambient seismic noise cut into hourly segments to gain a high temporal resolution. Afterward, we apply spectral whitening and estimate Green's function for every possible station pair using MSNoise (Lecocq et al., 2014). We use a Wiener Filter similar to Mao et al. (2019a) to increase the signal-to-noise ratio. This 2D filter is applied with the same filter length of 3 in both dimensions (vertical: hour [h]; horizontal: lag time [s]), which helps to reduce incoherent noise. From the filtered traces, we calculate a reference stack for every month and station pair to remove seasonal trends and increase the focus on the daily behavior of the subsurface. To determine the differences in the arrival time (dt/t), we use the Moving Window Cross Spectral Analysis (MWCS; Clarke et al., 2011; Ratdomopurbo and Poupinet, 1995). The underlying assumption is that the velocity perturbation is constant within the whole medium. This perturbation leads to a linear proportionality between the lapse time and the delay time (Poupinet et al., 1984). By estimating the slope of this proportionality, we get the relative arrival time changes (dt/t) which corresponds to the negative relative velocity change (dt/t = -dv/v). Using the MWCS analysis, we measure phase changes in coda waves to rule out or avoid potential influences of changes in the noise spectrum (Zhan et al., 2013). In addition to other studies on daily behavior, we calculate the relative seismic velocity changes in different frequency bands (3-7, 4-8, 5-9, 6-10 Hz) to investigate their depth dependency (after Herrmann (2013), Figure A.1 in Supporting Information A).

3.3. Results

3.3.1. Relative Seismic Velocity Changes

The result of the MWCS-Analysis in the 4-8 Hz frequency band is shown in Figure 3.2a. To decrease errors of individual station pair dv/v measurements, we calculate the mean over 300 station pairs. The other time series of dv/v can be found in Figure A.2 in Supporting Information A. We observe dv/v perturbations of the order of $10{-}4$, which is in good agreement with other studies (Mao et al., 2019a; Sens-Schönfelder and Eulenfeld, 2019). Our results show short-term (daily) variations and long-term (monthly) trends. The driving force for the long-term behavior is likely precipitation (Nakata and Snieder, 2012; Sens-Schönfelder and Wegler, 2006), including snowfall and the resulting load of the snow (Guillemot et al., 2021; Mordret et al., 2016), as well as barometric pressure (Gradon et al., 2021; Niu et al., 2008). Comparing the results of the other frequency bands shows that all significant long-term features are observable in the different bands (see Figure A.2 in Supporting Information A), for example, the linear decrease of the seismic velocities around Julian day 110. This study rather focuses on daily and sub-daily features which are more accessible via spectral analysis

as presented in the following.

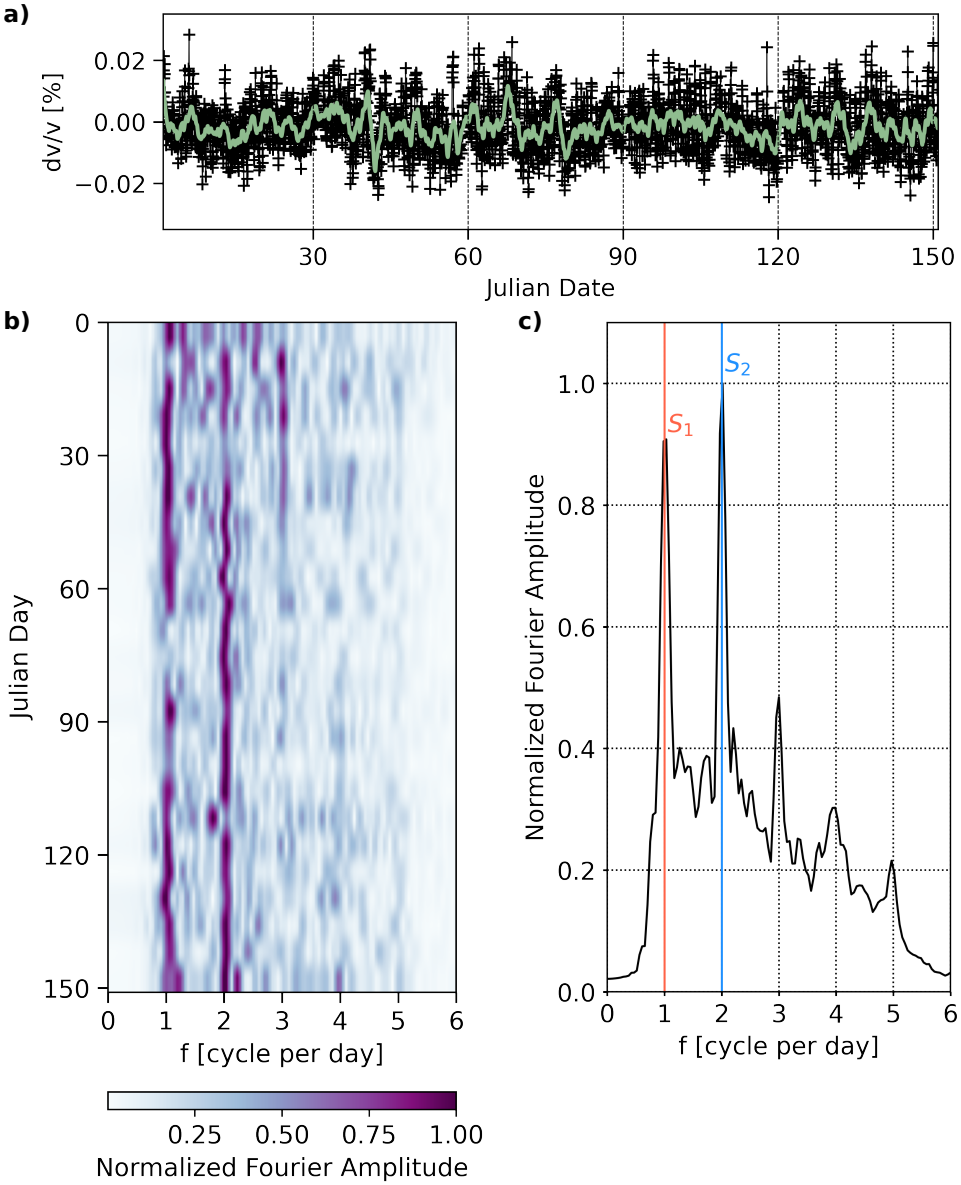


Figure 3.2.: (a) dv/v time series in the 4-8 Hz frequency band. The green curve shows a smoothed version of the hourly measurements (black line with crosses). (b) 2D spectrogram from a 7-day sliding window Fourier analysis. (c) Stack of the sliding windows. The red and blue lines indicate the one (S1) and two (S2) cycles per day, respectively.

3.3.2. Spectral Analysis

To reveal the periodicity of dv/v throughout the days we have calculated the Fourier transform. For that, we split the dv/v time series into chunks of 7 days and padded them with zero to get more frequency bins. The overall process works in a sliding window with a step of 2 days. We do that to increase the number of individual spectra to increase the signal-to-noise ratio of the final stack. The resulting 2D spectrogram in Figure 3.2b shows consistent strong amplitudes around one and two cycles per day (called in the following simply S_1 and S_2). They are also often called the diurnal and semidiurnal terms. Some weaker amplitudes are observable at three, four, and five cycles per day. This trend manifests itself, when we increase the length of the sliding window. Even with a high resolution in the frequency domain the main peaks occur at S_1 and S_2. We do not observe a strong peak at 1.93 cycles per day, which we might have expected from solid-Earth tides (M_2). The stack along the time axis (see Figure 3.2c) verifies the observation and reveals the strong peaks and their ratios. The spectrograms and stacks for the different frequency bands show some differences (Figures A.3 and A.4 in Supporting Information A). For the highest frequencies S_1 is dominant. The lower the frequencies the stronger the S_2 peak is. The band in between shows the background trend, which is an increase of the S_2 peak. For the three- and four-cycles-per-day peaks, a decrease in strength is observed as well.

3.4. Discussion

3.4.1. Possible Environmental Effects Causing Seismic Velocity Variation

High-temporal-resolution monitoring has received more attention in recent years (Mao et al., 2019a; Oakley et al., 2021; Sens-Schönfelder and Eulenfeld, 2019). The interest is to observe small changes in subsurface properties, and to eventually relate them to changes in stressing conditions and/or fluid content. There are more factors the observations are sensitive to, and we need to consider several environmental effects and their potential influence on the behavior of seismic velocities.

We can distinguish between periodic and non-periodic influences. Precipitation is a non-periodic effect, which affects the long-term behavior of seismic velocities (Andajani et al., 2020; Nakata and Snieder, 2012; Sens-Schönfelder and Wegler, 2006; Wang et al., 2017). If water is added or removed from the medium, the seismic velocity changes. The slow diffusion of water toward greater depth can be a reason for a long-term trend (Roeloffs, 1996). On the same timescale, atmospheric pressure influences velocities (Gradon et al., 2021). A particular case of precipitation is snowfall, which is a coupled effect that not only changes the water content. It adds a load to the medium, which changes the elastic properties (Guillemot et al., 2021; Mordret et al., 2016).

In this paper, we focus primarily on periodic effects. Temperature and atmospheric pressure are largely, but not strictly periodic; we investigate their influence on a daily time-scale only. Figure 3.3 shows a combined plot of the spectra of these effects together with the spectrum of the velocity time series. We can see that all of them have daily and sub-daily components.

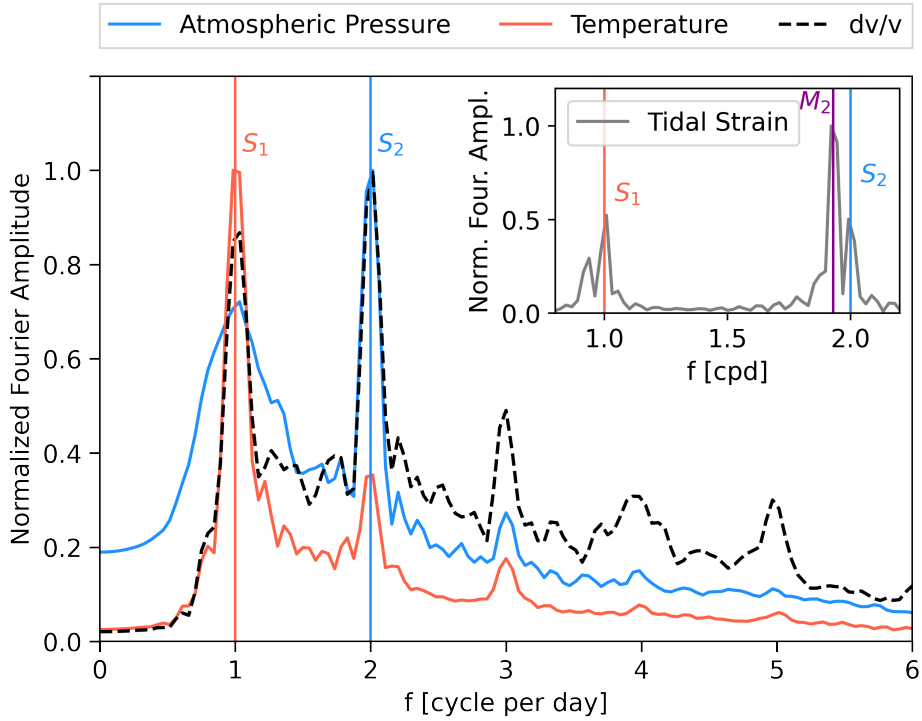


Figure 3.3.: Spectra of atmospheric pressure (blue line), temperature (red line), and dv/v (black dashed line). The inset shows the spectrum of the theoretically determined tidal strain at the German Experimental Seismic System array. Vertical lines indicate the main periods in the spectrum of different effects.

The deformation of the Earth's subsurface due to solid-Earth tides is widely discussed (Sens-Schönfelder and Eulenfeld, 2019). Due to gravitational forces, the elastic rocks are deformed, which leads to variation of the seismic velocities (Yamamura et al., 2003). The spectrum of the tides (Figure 3 inset) shows a one (S_1), two (S_2), and 1.93 (M_2) cycles per day behavior. The first two are called diurnal and semi-diurnal term. The M_2 component is the one with the highest amplitude. Since the dv/v observations show no such component, the influence of solid-Earth tides is clearly much weaker than that of other effects.

The temperature spectrum shows a strong one-cycle-per-day (S_1) and a weak two-cycles-per-day (S_2) peak. This suggests that temperature contributes to the S_1 peak but not significantly to the S_2 behavior. The influence of temperature on the dv/v measurements is not as straightforward as the one of precipitation or tides. On one hand, the direct influence of temperature changes applies to the top meters of the subsurface. On the other hand, heating and cooling throughout the day caused changes in the strain in the subsurface. From Ben-Zion and Leary (1986) or Berger (1975), we know that the impact of this thermoelastic strain can be much deeper than the few meters influence of temperature.

Since atmospheric pressure shows a strong S_1 and S_2 behavior, similar to the dv/v, we suggest it as the dominating force of the daily behavior of the dv/v. Gradon et al. (2021) already emphasized a strong correlation between longer-term atmospheric pressure changes and dv/v measurements over certain time scales. In the following section, we suggest a model of how the strong influence on daily behavior can be explained.

3.4.2. Interaction of Aquifers With Atmospheric Pressure

Spectral analysis of the dv/v time series shows a dominant peak around one and two cycles per day (S_1 and S_2). The comparison with potential periodic effects has suggested that the dominant driving force for this behavior is the atmospheric pressure changes. The atmospheric pressure has strong diurnal and semi-diurnal variations. This phenomenon is called atmospheric tides. It is a globally observed phenomenon mainly caused by solar radiation and thermodynamic effects related to ozone and water vapor (Chapman, 1951; Palumbo, 1998). In contrast to the solid or ocean Earth tides, the gravitational effects play a minor role in the generation of atmospheric tides. The diurnal component (S_1) is directly related to the heating and cooling of air due to solar radiation during the day. The origin of the semi-diurnal component (S_2) is still under discussion. It is most likely due to an interplay between thermodynamic mechanisms with a one cycle per day component (Palumbo, 1998). A quantitative analysis of both cycles shows that the S_2 is much stronger than the S1 component (Chapman and Malin, 1970). This is also visible in the spectrum of atmospheric pressure measured at the GERES array (see Figure 3.3).

The question arises, why the atmospheric pressure has such a strong imprint on the dv/v measurements while solid Earth tides do not. In the following, we will discuss possible mechanisms related to seismic velocity changes and air pressure variations.

The direct effect of air pressure changes is the loading and unloading of mass at the Earth's surface. An increase of pressure is associated with the mass which acts on the surface. This load results in a compression of the material in the subsurface. On a microscopic scale, this would mean that cracks are closing (Silver et al., 2007). This yields an increase of seismic velocity. During an episode of unloading cracks open up again and seismic velocity decrease. In saturated conditions, another mechanism must be considered. When cracks are closed, the fluid within is pushed to the pores. This leads to an overall increase of the pore pressure and a decrease of seismic velocity (Andajani et al., 2020). To quantify the effect we assume that a change of 1 kPa induces 10^{-9} elastic strain in the Earth's crust (Rabbel and Zschau, 1985). We observe daily changes of 600 Pa, so this will result in 6×10^{-10}. A comparison with Mao et al. (2019a) shows that this strain will lead to a relative velocity change of about 6×10^{-6}. This effect is too small to explain the observed velocity changes of 10^{-4}.

The second mechanism which one has to take into consideration is the displacement of the water table due to changes in atmospheric pressure. Hydrological measurements, for example, McMillan et al. (2019), show a strong correlation between atmospheric pressure changes and

groundwater level. The effect of groundwater level changes on long-term dv/v measurements has already been discussed in the literature (Clements and Denolle, 2018; Voisin et al., 2017). More importantly, we can observe these changes on a daily and sub-daily basis. If the pressure increases the water table is pushed into deeper parts.

During a period of low pressure, the water migrates toward the surface (see Figure 3.4). The reaction of the groundwater table to the pressure changes is lagging and thus phase shifted up to several hours (for example, Rasmussen and Crawford, 1997), due to the propagation time of the pressure wave to the aquifer and water diffusion towards greater depth.

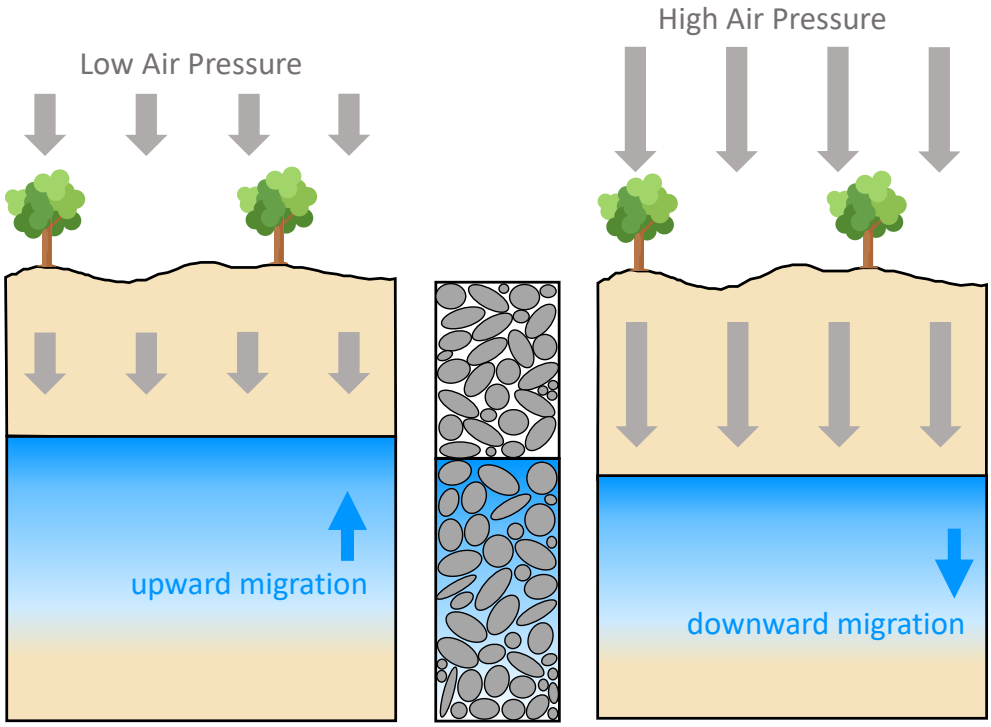


Figure 3.4.: Schematic representation of the interaction of atmospheric pressure and water table depth. The illustration in the middle shows the pores of the different layers.

This will influence the subsurface in several ways. Tsai (2011) proposed two mechanisms that come along with the change of groundwater table depth. The first one is the poroelastic effect which describes the reaction of a saturated material to a strain. It is characterized by the hydraulic properties of the media. The second mechanism is the direct elastic effect due to the additional mass of water. According to Tsai (2011), the two effects have the same order of magnitude, but the model is not fully suitable for our observations. The model is constrained for the media below the groundwater table. We expect that our method is most sensitive around the groundwater table. This leads to a minor influence of the two described effects. We therefore want to introduce another mechanism that would lead to the observed

velocity changes. If the atmospheric pressure changes the depth of the groundwater table some parts of the subsurface will change their saturation degree. According to multiple laboratory measurements, for example, Mavko et al. (2009), Dong and Lu (2016) as well as modeling studies like Solazzi et al. (2021) a different saturation would lead to significant changes in the S wave velocity, which also dominates the surface wave velocity. This mechanism can explain the observed velocity change in the order of 10^{-4}. In the observed time series, a combination of all described effects is realistic.

3.4.3. Second Order Effect: Temperature Changes

We recognize a strong daily variation in the day's temperature and seismic velocity (see Figure 3.3). The influence of temperature changes on dv/v is discussed in Mao et al. (2019a), Oakley et al. (2021) and Sens-Schönfelder and Eulenfeld (2019). For the S_1, thermoelastic strain is estimated to be on the order of 10^{-8}. This is in the same range as the estimated strain caused by the displacement of the water table. According to Ben-Zion and Leary (1986), the strain induced by the S_2 variation is smaller, but yet not quantified. We notice that the ratio between the amplitudes at the dominant peaks changes with frequency. Decay in the amplitude of S_1 is observed while S_2 increases. Within a few meters, S_1 is not dominating anymore. We interpret that as a decreasing influence of thermoelastic strain with increasing depth. This leads to the conclusion that we can explain the behavior of dv/v as a superposition of thermal and pressure effects, but it is dominated by the latter over depth (see Figures A.2 and A.3 in Supporting Information A).

3.4.4. Comparison With Other Studies

In our study, we observe a strong S1 effect. This is in good agreement with other studies on the daily behavior of dv/v (Mao et al., 2019a; Oakley et al., 2021; Sens-Schönfelder and Eulenfeld, 2019). All studies interpret this cycle as an imprint of temperature changes. In addition, Mao et al. (2019a) have evoked tidal forcing to explain this peak. Unlike other studies with this high temporal resolution (Mao et al., 2019a; Sens-Schönfelder and Eulenfeld, 2019), we do not consistently observe the M2 peak caused by the tidal deformation of the Earth (Figure 3.3 inset). An M_2 peak is observable for some station pairs only, but much weaker than in other studies. This could be because this effect is too small to be detected with our accuracy or within our geological setting. A similar conclusion was reached from a study of monochromatic seismic signals at the same place (Baisch and Bokelmann, 1999). The other mentioned studies had been performed primarily in sedimentary settings. Compared with the hard-rock environment, the stiffness of sedimentary rocks is lower (Karagianni et al., 2010). That means that they deform more under tidal stressing than hard rocks. The absence of an M_2 peak could also be associated with the location of our test site, far away from coastal lines, which are affected by oceanic tides (which would give rise to a strong M_2 peak). Since we cannot observe that tidal constituent, we can neglect tidal effects as driving force for the daily velocity variations.

Oakley et al. (2021) do not observe the strong S_2 component, as we see it in our data. They use higher frequencies and show that their experiment is under dry conditions. In some special cases, coda wave sensitive close to the depth of the groundwater table observe a weak S2 component. Oakley et al. (2021) interpret this effect also as water table migration. This strengthens our argument about the interaction of aquifers and atmospheric tides in the behavior of dv/v in a day.

The comparison with other studies shows the complexity of the problem. It seems that the character of velocity variations depends somewhat on the test site. This includes the geological setting as well as their location. Further, the outcome depends on the chosen frequency bands. Lower frequencies are more sensitive to greater depth and are potentially stronger influenced by the interaction of aquifers and atmospheric tides. The higher the frequency, the lower this influence.

3.4.5. Perspectives

Ambient seismic monitoring has been found to be very useful for geophysical monitoring, to better understand the behavior of Earth's crust before, during and after tectonic events, especially in active seismic regions (Brenguier et al., 2008a; Ellsworth and Beroza, 1995). This is also motivated by recent laboratory studies that suggest that seismic velocity variations have important predictive capabilities (Dresen et al., 2020; Scuderi et al., 2016). The determined velocity time series however contain multiple imprints of environmental effects, which can be relatively strong compared to the small changes due to tectonic stress changes or earthquakes. Our study helps to filter out those interferences to reveal the response of the Earth to stress changes, and preseismic effects in particular. The results also manifest the strong influence of water/fluids on the dv/v, which may also be of more direct use itself (Roeloffs, 1988). That we can observe the relatively small changes of the groundwater table suggests that the technique may have sufficient sensitivity to also see other perturbations of the groundwater system, and that it may open new perspectives in groundwater geophysics, for example, for reservoir characterization; it may perhaps also help to better understand geothermal reservoirs. The non-intrusive nature of seismic methods may indeed be particularly useful in hydrogeophysics in general. Somewhat surprisingly, the field of hydrogeophysics appears to be largely devoid of "transmission" seismic methods so far.

3.5. Conclusions

We use ambient noise monitoring to show daily and sub-daily seismic velocity variations with a magnitude of 10^{-4}. We achieve a high temporal resolution for the velocity time series by using a small and relatively dense array. By calculating the spectrum of the dv/v, we reveal strong daily and sub-daily components. To some extent, we confirm the results and proposed driving forces from earlier studies of the daily variation. In contrast, we do not observe a strong influence of Earth's tides. Instead, we detect a strong influence of atmospheric pressure variations (atmospheric tides) on the behavior of relative seismic velocity

changes. We thus introduce a model that connects atmospheric loading and the observed dv/v changes. There is ample room for more seismic studies of groundwater and groundwater reservoir. The sensitivity to groundwater indicates that these effects may need to be taken into account if one wants to connect temporal velocity changes with tectonic stress changes. Different sites and experimental settings may lead to different dominating effects and varying strengths. Nevertheless, a step in the direction of high temporal resolution monitoring of crustal deformation is made.

Data Availability Statement

The data used for performing this study is publicly available. It can be requested either via European Integrated Data Archive (EIDA - https://eida.bgr.de) or the incorporated Research Institutions for Seismology (IRIS - http://ds.iris.edu/ds/). The GERES array is part of the German Regional Seismic Network (GR - https://doi. org/10.25928/mbx6-hr74) and is hosted by the BGR. To get the data of the GERES array the stations GEA0, GEA1, GEA2, GEB1, GEB2, GEB3, GEB4, GEB5, GEC1, GEC2, GEC3, GEC4, GEC5, GEC6, GEC7, GED1, GED2, GED3, GED4, GED5, GED6, GED7, GED8, GED9 must be selected.

Acknowledgments

The authors thank two anonymous reviewers and the Editor, Germán Prieto, for their constructive feedback, which helped us to improve our manuscript. The authors also want to acknowledge that the Federal Institute for Geosciences and Natural Resources (BGR, Germany) and the Comprehensive Nuclear-Test Ban Treaty Organization (CTBTO) maintain the seismic stations and provide open access to the data.

Erratum

The originally published version of this article contained a typographical error. In the reference for Niu et al. (2008), the article title should be "Preseismic velocity changes observed from active source monitoring at the Parkfield SAFOD drill site" instead of "Superior colliculus and visual spatial attention." The error has been corrected, and this may be considered the authoritative version of record.

Publication

The presented study (Kramer et al., 2023) was published in the Journal Geophysical Research Letters on April 3, 2023.

AGU ADVANCING EARTH AND SPACE SCIENCE

Geophysical Research Letters

RESEARCH LETTER
10.1029/2022GL101298

Interaction of Air Pressure and Groundwater as Main Cause of Sub-Daily Relative Seismic Velocity Changes

R. Kramer[1], Y. Lu[1], and G. Bokelmann[1]

[1]Department of Meteorology and Geophysics, University of Vienna, Vienna, Austria

Key Points:

- We observe strong daily and sub-daily variations of seismic velocity using coda wave interferometry
- The effect is caused predominantly by the coupling of atmospheric pressure and groundwater table variations
- The coupling allows a better understanding of crustal deformation and suggests novel techniques for characterizing aquifer systems

Supporting Information:

Supporting Information may be found in the online version of this article.

Correspondence to:

R. Kramer,
richard.kramer@univie.ac.at

Citation:

Kramer, R., Lu, Y., & Bokelmann, G. (2023). Interaction of air pressure and groundwater as main cause of sub-daily relative seismic velocity changes. *Geophysical Research Letters*, *50*, e2022GL101298. https://doi.org/10.1029/2022GL101298

Received 20 SEP 2022
Accepted 26 JAN 2023

Author Contributions:

Conceptualization: R. Kramer
Investigation: R. Kramer
Methodology: R. Kramer
Supervision: Y. Lu, G. Bokelmann
Visualization: R. Kramer
Writing – original draft: R. Kramer
Writing – review & editing: Y. Lu, G. Bokelmann

© 2023. The Authors.
This is an open access article under the terms of the Creative Commons Attribution License, which permits use, distribution and reproduction in any medium, provided the original work is properly cited.

Abstract Our study investigates variations of seismic velocity that occur over short time scales of hours. We use coda wave interferometry to inspect 5 months of continuous data from a seismological array in southern Germany. This results in relative seismic velocities (dv/v) that show temporal variations on the order of 10^{-4}. Spectra of the velocity time series contain strong daily and sub-daily behavior indicating that the daily and sub-daily changes in the seismic velocity are primarily caused by atmospheric tides. We also note the influence of temperature changes on daily variations, but as a second-order effect. The explanatory model focuses on depth variations of the groundwater table, linking atmospheric pressure (loading and de-loading the Earth's surface) to variations in seismic velocity. Our results highlight an important environmental influence on seismic velocity that needs to be considered before seismic velocity variations can be used for inspecting fluid and stress variations in situ.

Plain Language Summary Geological and environmental effects manifest themselves in changes of crustal properties, and we record these as variations of seismic wave velocity. This is especially the case for seismic waves that travel within the Earth's crust. Changes in tectonic stress are particularly interesting, since they can cause earthquakes. We would also like to know more about changes in fluid content in the crust at the various depth levels. Both tectonic stress and fluid content affect seismic velocity, but environmental factors also have an effect and these need to be taken into account. This study shows that the interaction of air pressure and groundwater, has considerable influence on measured daily velocity variations. This opens important possibilities in itself. On the other hand, we can remove these pressure effects from the velocity changes, to highlight changes due to tectonic effects, such as earthquakes.

1. Introduction

The research toward understanding large earthquakes' generation and precursor phases is still in process (Conti et al., 2021; Ellsworth & Beroza, 1995). A key parameter to better understand the temporal component of these processes is the changing strain and stress within Earth's crust. The elastic moduli of the rocks directly link these variations to seismic velocity changes. By knowing this relationship, measuring changes of seismic velocity provides insight into the temporal evolution of strain in the subsurface. However, this relationship is disturbed by the influence of environmental effects, for example, temperature, precipitation (Hillers et al., 2015; Richter et al., 2014; Schönfelder & Wegler, 2006; Wang et al., 2017). Collecting information about time-varying environmental processes perturbing Earth's crust is thus essential to reveal crustal deformation associated with tectonics.

The classical approaches to probe this behavior, which have used active seismic experiments (Niu et al., 2008; Yamamura et al., 2003) are increasingly replaced by monitoring using seismic ambient noise and the concept of coda wave interferometry. In the first step, the long-term influence of environmental effects was discussed (Gradon et al., 2021; Richter et al., 2014; Schönfelder & Wegler, 2006). Also, the strong imprint of groundwater level changes is widely discussed and described (Clements & Denolle, 2018; Gassenmeier et al., 2014). Recent years have shown a trend toward high temporal resolution monitoring (Mao et al., 2019; Oakley et al., 2021; Schönfelder & Eulenfeld, 2019). These studies show that environmental effects such as daily temperature changes (Mao et al., 2019; Oakley et al., 2021) and tidal stress (Mao et al., 2019; Schönfelder & Eulenfeld, 2019) substantially impact seismic velocities. However, in contrast to long-term studies, the influence of daily groundwater table changes or atmospheric pressure variations is merely discussed.

In this study, we fill this gap by investigating data from a highly sensitive array in southern Germany, which is far away from potential local disturbances, such as cities or roads. We calculate an hourly dv/v value for high temporal resolution monitoring. Our measurements show that the seismic velocities have daily and sub-daily

3.6. Extended Discussion

The study presented a new observation based on high-temporal-resolution monitoring of relative seismic velocity changes. It is an important contribution to our understanding of the influence of environmental parameters, such as air pressure, on dv/v. The GERES array is ideal for this study because the sensors are installed in holes in the ground. This eliminates the direct influence of environmental factors, such as variations in air pressure, on the seismic sensor. Although the methods presented are robust, the paper could benefit from a more in-depth discussion of the stability and distribution of noise sources. This is particularly relevant on the sub-daily timescale, as well as for potential variations in source intensity or directionality, which could affect the inferred changes. Due to the array's location in the forest, far from potential periodic human noise sources, this effect may be negligible, but further strengthening the conclusion is possible.

The intention of this study was to build on the findings of Mao et al. (2019a) and deepen our understanding of the periodic influences on seismic velocity throughout the day. Although the study settings are quite different, the extent of the arrays is comparable. Throughout the data processing and frequency analysis, we noticed the absence of the M_2 tidal component found in Mao et al. (2019a). Despite testing multiple methods and signal enhancement processes, it was not observable. This led to a different scope of publication and shaped the dissertation in general. In need of an alternative explanation for the observed periodicity, we considered the potential influence of air pressure on seismic velocity changes. As this was unexplored territory in seismology, the interpretation may be lacking in detail; however, the intention was to provide an initial description and explanation of the observed phenomenon.

The focus on air pressure and groundwater interaction was an initial attempt to establish a connection through seismic velocities. However, this approach oversimplifies near-surface dynamics and does not fully explain possible other mechanisms. For instance, it disregards the principles of poroelasticity to link atmospheric loading with near-surface stress variations and subsequent changes in seismic velocities. Furthermore, the spatial variability in subsurface properties could be addressed more explicitly. Variations in lithology, porosity, and hydraulic conductivity could lead to differential responses in seismic velocity changes. Ultimately, the hypothesis should be verified using numerical modeling that takes these factors into consideration.

Additionally, the specific setting and the use of data from a small array could lead to conclusions that are context-specific. Expanding the analysis to a larger region with varying subsurface characteristics would help determine the broader applicability of the findings. These considerations motivated the second study, which is presented and discussed in the next chapter.

4 Identifying Large Vulnerable Water Reservoirs Using Passive Seismic Monitoring

Highlights

- Mapping periodic dv/v across large-scale regional seismic networks.
- Assessing shallow aquifer vulnerability using seismic observations.
- Innovative applications of seismic methods in environmental research.

Abstract

Seismic waves capture important insights into subsurface behavior. We introduce an adapted coda-wave interferometry approach to monitor the spatial variability of semi-daily periodic seismic velocity changes on a regional scale, applied to data collected across South and Central Europe. Our results reveal a broad spatial correlation between seismic velocity changes and air pressure fluctuations, suggesting that air pressure is the dominant driving force. Specifically, air pressure fluctuations modulate saturation levels within the capillary zone through the dynamic interplay between fluid and gaseous phases, producing significant seismic velocity changes. The mechanism explains the large variations observed in regions with high connectivity between the surface and saturated zone. We associate this enhanced interaction with the high vulnerability of shallow water resources. We propose inspecting semi-daily periodic seismic velocity changes as a new tool for gaining a regional view of water reservoir vulnerability.

4.1. Introduction

Climate-change induced droughts and increasing industrial activity, have significantly intensified water demand (Megdal, 2018). Addressing these global challenges requires understanding and managing water resources to ensure a sustainable and resilient society and ecosystem (Mukherjee et al., 2018). In this context, shallow groundwater resources are broadly available and easily accessible and therefore particularly important (Wang et al., 2014; Gao et al., 2018). However, the high permeability and connectivity associated with shallow aquifer systems raise concerns about potential pollution and contamination (Al-Hashimi et al., 2021). Thus, acquiring a better understanding of the vulnerability of this water resource is imperative.

Aquifer vulnerability refers to the risk of pollution or contamination by substances such as chemicals or wastewater (Jang et al., 2017; Heinz et al., 2006). Methods and tools that allow constraining vulnerability are important to enhance awareness among decision-makers and the public, promoting secure water usage practices. The assessment of aquifer vulnerability commonly relies on measuring barometric efficiency (Hussein et al., 2013; Odling et al., 2015). This metric represents the susceptibility of the groundwater table to air pressure fluctuations,

and it offers information about aquifer vertical diffusivity as a crucial determinant of vulnerability (Hussein et al., 2013). However, at present, measurements of barometric efficiency are confined to sparse point-wise borehole observations, subject to local geo-hydrological variabilities. This emphasizes the need for a novel efficient tool that can infer shallow aquifer properties at larger scales, ranging from individual reservoirs to regional hydrological units.

Recent studies (Clements and Denolle, 2018; Mao et al., 2022) have highlighted the potential of ambient noise seismology for imaging the shallow subsurface and for temporal monitoring beside registering seismic events. This approach can provide continuous tracking of (temporal variations) seismic velocities. Initially aimed at understanding the evolution of crustal stress associated with earthquakes (Brenguier et al., 2008a; Obermann et al., 2014; Wang et al., 2019), many studies have also revealed that the observed seismic velocities are affected by environmental processes like seasonal temperature cycles, precipitation, snow, and air pressure fluctuations (Sens-Schönfelder and Wegler, 2006; Richter et al., 2014; Hillers et al., 2015a; Wang et al., 2017; Gradon et al., 2021; Guillemot et al., 2021). Moreover, long-term investigations have drawn attention towards the notable impact of groundwater-level fluctuations on the seismic velocities (Sens-Schönfelder and Wegler, 2006; Gassenmeier et al., 2014; Lecocq et al., 2014; Voisin et al., 2017; Clements and Denolle, 2018; Rodríguez Tribaldos and Ajo-Franklin, 2021). Recent research has further illuminated the impact of short-term periodic effects, which routinely alter seismic velocities (Mao et al., 2019a; Sens-Schönfelder and Eulenfeld, 2019; Oakley et al., 2021; Kramer et al., 2023). Considered as repetitive phenomena overprinting transient events, observations on the periodic seismic velocity changes contain stable information about the subsurface processes (Oakley et al., 2021; Kramer et al., 2023).

This study aims at assessing the vulnerability of shallow aquifers across South-Central Europe using observations of air-pressure-induced seismic velocity changes. As demonstrated in e.g. Gradon et al. (2021) and Kramer et al. (2023), air pressure fluctuations and their interaction with aquifers lead to substantial changes in seismic velocities. We focus specifically on examining periodic air pressure fluctuations caused by atmospheric tides.

Atmospheric tides are regular diurnal and semi-diurnal oscillations in the wind, temperature and pressure fields, which arise from the superposition of thermal effects and the gravitational force. The absorption of solar radiation in the atmosphere generates internal gravity waves that propagate downwards, contributing to both diurnal and semi-diurnal surface pressure oscillations (Chapman and Lindzen, 1970). In tropical areas, semidiurnal oscillations typically have greater amplitude than diurnal oscillations. Over land areas in the extratropics, the amplitude of diurnal oscillations is greatly enhanced by sensible heating from the ground (Dai and Wang, 1999). Semi-diurnal atmospheric pressure oscillations are supposed to be the main driving force for sub-daily periodic seismic velocity changes (Kramer et al., 2023). We propose that the strength of this seismic velocity cycle primarily reflects the air and water diffusivity above the groundwater table, which can serve as a proxy for barometric efficiency. The underlying mechanism will be elaborated upon in subsequent sections.

Studies of the barometric efficiency are conducted locally at boreholes (Hussein et al., 2013; Odling et al., 2015; Valois et al., 2022), and spatial mapping of this fundamental metric is hardly available. This is where our investigation becomes crucial, since it can provide such spatial information, allowing to capture the complexity of the geo-hydrogeological settings within Europe and the study area. Among the prominent geological features are the Po plain, the Alps, the Apennines, the Dinarides, the Pyrenees, and additional distinctive formations such as the Alpine Foreland (Fig. 4.1a). This diverse landscape gives rise to two primary types of aquifers, exhibiting spatial variations across the region (Cornu et al., 2013). Aquifers within consolidated rocks, such as limestones or sandstones, coexist alongside aquifers within unconsolidated rocks like sands (Cornu et al., 2013; Nistor, 2020). To capture the complex structure of the area, our study takes advantage of data obtained from meteorological services as well as seismic networks across southern and central Europe (Hetényi et al., 2018), to (i) demonstrate the feasibility of passive coda-wave monitoring utilizing typical broadband network setups with large inter-station spacing, and (ii) unveil the potential of using seismic velocity observations to map the hydro-physical properties of underlying groundwater bodies.

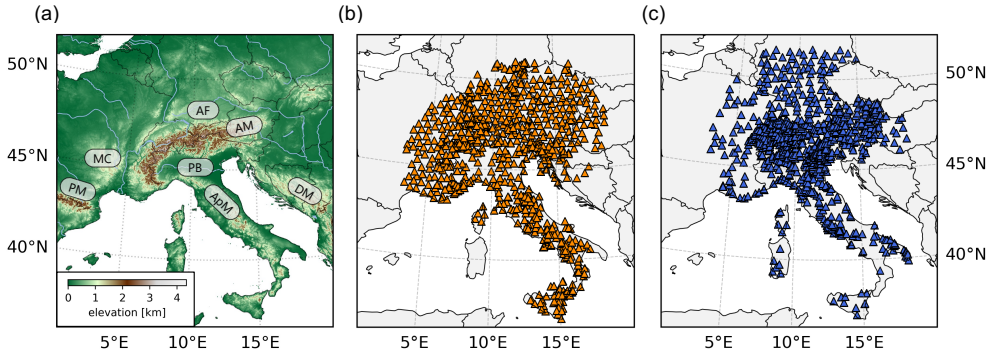


Figure 4.1.: Maps of the study area. (**a**) Overview of topographical variations across Europe, including the main geological features (AF - Alpine Foreland, AM - Alpine Mountains, ApM - Apennines, DM - Dinarides, PB - Po Basin, and PM - Pyrenees). (**b**) Distribution of the broadband seismic stations. (**c**) Meteorological stations used within the study.

4.2. Data and methods

4.2.1. Continuous seismic data

This study benefits from the growing number of broadband sensor installations across Europe in recent years. Notably, temporary deployments associated with the AlpArray project (Hetényi et al., 2018), have significantly contributed to filling the existing broadband station gaps

in central and southern Europe. This has resulted in a dense broadband station coverage in the region during the considered period of data analysis, where the average inter-station distance is around 50 km. In total we gather four years (2016-2019) of continuous seismic data recorded at more than 1400 broadband seismic stations distributed over southern and central Europe, as shown in Fig. 4.1b. Following Lu et al. (2018), we pre-processed the continuous data reordered by each station in two main steps. Firstly, each hourly data was detrended, band-pass filtered, and instrument-response corrected. Secondly, we removed hourly data possibly containing earthquakes or other transient events. The remaining hourly segments were then whitened in the frequency domain and cross-correlated between station pairs with an inter-station distance between 25 km and 75 km.

4.2.2. Measurements of seismic velocity changes

Our objective is to extract short-term periodic seismic velocity changes from large-scale seismic arrays with relatively long interstation distances (around 50 km on average). Previous studies that focused on daily and sub-daily seismic velocity variations typically used relatively small arrays (Mao et al., 2019a; Oakley et al., 2021; Kramer et al., 2023) or single stations (Sens-Schönfelder and Eulenfeld, 2019). Extending this approach for large-scale observations presents challenges: the interstation distances become larger, making it more difficult to obtain stable and reliable hourly observations over larger areas. To address this challenge, we propose a novel approach to generate pseudo high-temporal-resolution seismic velocity observations. We profit from the stable short-term periodic variations in the environmental driving forces such as air pressure and temperature. Resulting daily and sub-daily seismic velocities are expected to follow a similar repeating cycle each day. This is validated by inspecting spatio-temporal changes in the meteorological dataset (Fig. B.1).

We calculate hourly cross-correlations within the frequency band of 0.5-1.5 Hz (Fig. 4.2b) to focus on near-subsurface behavior. As mentioned earlier, calculating hourly cross-correlations for large-scale investigations proves challenging due to the presence of long travel paths and strong attenuation, making it difficult to obtain reliable measurements (Hadziioannou et al., 2011). Therefore, we stack the cross-correlations for corresponding 24-hour periods over the four-year time span (Fig. 4.2c). It is important to note that each cross-correlation is normalized by its maximum amplitude before stacking to mitigate the effects of transient events and highlight those of periodic phenomena that occur consistently over days. This approach yields a total of 24 unique cross-correlation functions (Fig. 4.2c) for each station pair, from which we measure changes in seismic velocity from coda waves.
In order to precisely define the coda-wave time window, we first measured the Rayleigh wave peak-envelope arrival time around the desired periods for each station pair. The obtained group velocities at 1-s period, the dominant period band used in this study, demonstrate a striking spatial correlation with the prominent geological features of the region. For instance, high velocities are evident in the Alps, contrasting with lower velocities observed in the Po plain and the Molasse basin (Fig. B.3). This in a way validates our determination of Rayleigh-wave arrivals. Accordingly, we define the coda wave time window starting 2 s after the surface wave arrival and lasting for 30 s.

After identifying the coda window, we use the time stretching method (Sens-Schönfelder and Wegler, 2006) to determine the relative seismic velocity changes (dv/v). The underlying idea is that waveforms are compressed or stretched proportionally in response to dv/v variations in the medium. To find the corresponding dv/v value, we examine different stretching factors ϵ, selecting the one that maximizes the similarity between the stretched correlation function and the reference. Employing this technique in a series of sub-time windows (with 4-s window length) within the coda, we calculate their median value as the final dv/v measurement of each station pair to stabilize our results and minimize procedural error.

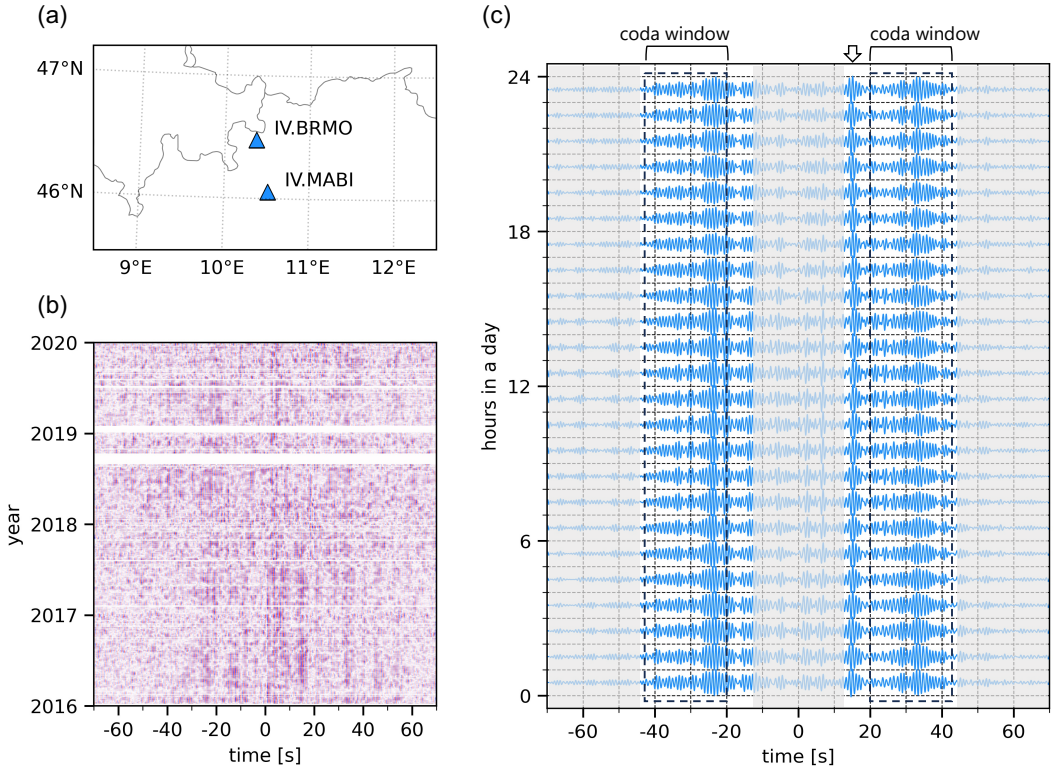


Figure 4.2.: Conceptualization of our long-distance high-temporal resolution monitoring approach. (**a**) Location of two stations of the Italian seismic network. (**b**) Normalized hourly cross-correlations between the two stations vertical component within the investigation time period. (**c**) Stacked cross-correlation for every hour. Each trace represents the stack of all corresponding hours within the time period. The arrow around 15 s indicates the theoretical arrival time of surface waves, followed by coda-wave windows.

4.2.3. Measurements of atmospheric pressure

We compile an atmospheric pressure dataset covering a similar spatial extent as the seismic dataset (Fig. 4.1c). Measurements of surface atmospheric pressure are routinely collected by meteorological services at hourly or sub-hourly temporal resolution and ingested in operational data assimilation and weather prediction systems worldwide Bauer et al. (2015). This study combines data transmitted to the WMO Global Telecommunication System and archived in NOAA's freely accessible Integrated Surface Database (Smith et al., 2011) with additional measurements obtained by national weather services upon request or through open data repositories. Measurements covering Italy were extracted by the Meteonetwork database (Giazzi et al., 2022), a citizen science open crowdsourced meteorological network that shares data from thousands of weather stations online on a sub-hourly basis. Because of heterogeneous data conventions, our merged hourly dataset (approx. 1500 stations from 01/2016 to 12/2019) contains a combination of station-level pressure and pressure reduced to sea level. The former is needed in this study. Missing records of surface pressure were reconstructed from sea-level pressure by inverting the pressure reduction formula (World Meteorological Organization (WMO), 1954). This was accomplished using information on surface temperature and elevation, but neglecting the influence of atmospheric humidity. Considering data subsets in which both surface pressure and reduced pressure are available, we verified that this approximation in the inversion of pressure reduction has a negligible impact on the reconstructed diurnal variability of station pressure.

4.2.4. Mapping spatial daily and semi-daily behavior of seismic velocities and meteorological parameters

To analyze the dominant periodic behavior, we decompose the measured seismic velocity changes (dv/v) into multiple sinusoidal functions with the periods of 24 h (S_1) and 12 h (S_2), representing the daily and semi-daily components respectively.

In order to capture and visualize spatial variations in the sub-daily behavior of the seismic velocity changes, we employed a regionalization procedure, spatially averaging measurements from individual station pairs. This involved defining a grid that covers the area of interest. Subsequently, we computed the average dv/v time series from station pairs within a 200 km radius around each centered grid point. To mitigate the influence of station pairs farther from the center, we applied a spatial Gaussian weighting function, effectively scaling down their impact. As basis for this we used the mid-point between the two stations and its distance from the grid point.

We adopted the aforementioned approach similarly for analyzing meteorological data. However, we reduced the radius to 50 km. This adjustment accounts for the strong spatial variability of meteorological variables across short spatial scales, influenced by factors like topography and other local effects.

4.3. Results and discussion

4.3.1. Periodic behavior of seismic velocity changes and air pressure

As described in the section before we decomposed the seismic velocities and air pressure into their main components. We further introduce the period of 8 hours (S_3) for the seismic velocities, as recognized by Mao et al. (2019a) and Kramer et al. (2023).

This will reduce the fitting residual error for the whole investigation area (see Fig. 4.3A; Fig. A.2 and Fig. A.4). Other minor components with higher frequencies only lead to a slightly improved fit. We focus on the daily and semi-daily components, which dominate the periodic changes. The spatial analysis of S_3 shows that it is roughly half of the S_2 amplitude. With that, we confirm earlier observations made from the GERES array in southern Germany using a conventional seismic noise coda-wave monitoring workflow (Kramer et al., 2023). Fig. 4.3a shows that the averaged amplitudes of S_1 and S_2 over the study area are in a similar range of magnitude, both on the order of 10^{-5}. The S_1 component shows a peak at approximately 14 hours, while the minimum occurs in the early morning hours around 2 hours. The S_2 component peaks around 5 hours and 17 hours, with minima occurring at approximately 11 hours and 23 hours.

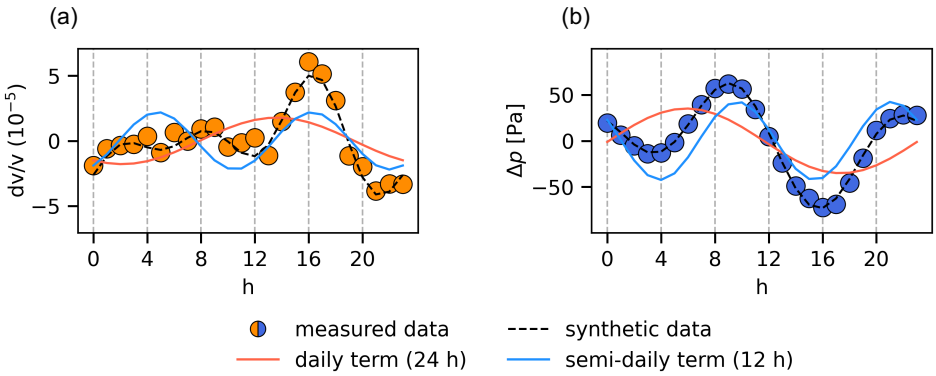


Figure 4.3.: Comparison of the periodic patterns of seismic velocity changes and air pressure (averaged over the entire study area). The orange and blue dots represent the averaged measurements of (**a**) seismic dv/v and (**b**) air pressure. The dashed black line indicates the synthetic data from fitting sinusoidal functions using 24-hour, 12-hour, and 8-hour periods. The red and blue lines represent the fitted daily and semi-daily terms, respectively. The S_3 curve has been omitted for illustration reasons and can be found in the supplementary section (see Fig. B.2).

A similar picture emerges when we decompose the signal of air pressure into S_1 and S_2 patterns (Fig. 4.3b). The two sinusoidal signals show amplitudes of 35 Pa and 43 Pa. The

S_1 component exhibits a peak at approximately 6 hours, while the minimum occurs in the late afternoon hours around 17 hours. Conversely, the S_2 component demonstrates an inverse slightly time shifted trend to seismic velocity changes, with peaks around 11 hours and 23 hours, and minima occurring at approximately 4 hours and 16 hours. These observations highlight the distinct periodic behaviors of air pressure, shedding light on its potential correlations with seismic phenomena.

Several studies (Hillers et al., 2015a; Mao et al., 2019a; Sens-Schönfelder and Eulenfeld, 2019; Oakley et al., 2021; Kramer et al., 2023) have identified the various driving forces that contribute to a significant S_1 component in the dv/v observation. These driving forces encompass temperature variations within the subsurface, leading to changing thermoelastic strain (Berger, 1975; Ben-Zion and Leary, 1986). Additionally, thermal-induced self-noise from the instrumentation has been recognized as another contributing factor (Wielandt, 2012). The quantification of the latter effect is challenging due to variations in the installation standards for different station networks. Furthermore, we have identified that fluctuations in air pressure can also play a significant role in the diurnal variation of seismic velocities (Kramer et al., 2023). In contrast to that, the S_2 is predominantly caused by changes in the air pressure (Kramer et al., 2023). Other factors such as solid Earth tides or soil moisture variations cannot explain the observations. This would help separate various driving forces, with its behavior more directly attributed to subsurface properties, particularly the hydro-physical properties of underlying groundwater bodies. Thus, we focus on the spatial pattern of the component in the following and elaborate on its meaning and potential applications.

4.3.2. Spatial variations of semi-daily velocity changes

Mapping the amplitude of the component (Fig. 4.4a) reveals significant spatial variability in this semi-daily behavior of seismic velocity changes across South-Central Europe.
Areas north of the Alps exhibit relatively low amplitudes, measuring below $0.25 \cdot 10^{-4}$, whereas areas to the south tend to display higher amplitudes, occasionally exceeding $0.5 \cdot 10^{-4}$. Particularly high amplitudes exist along the southern Alps in northern Italy and Slovenia, and along the Apennines in central Italy. The S_2 component of air pressure (Fig. 4.4b) exhibits a simpler spatial pattern characterized by a North-South difference, with smooth variations mostly in the range of 40 to 55 Pa. The highest amplitudes are observed in the border region between Slovenia and Croatia. Additionally, other notable features above the average of roughly 47 Pa are observed in southeastern France, within the Po plain in northern Italy, and along the Italian peninsula, following the mountain ridges of the Apennines.

Comparing velocity and air pressure reveals a general spatial correlation (Fig. 4.4), particularly regarding the north-south division relative to the Alps. Such a correlation is expected given the influence of air pressure on the amplitude of seismic velocity changes. Yet, this can not explain important detailed spatial discrepancies. For instance, the highest anomaly of air pressure does not coincide with the highest anomaly of seismic velocity changes. In general, we conclude that a stronger sub-daily air pressure cycle does not necessarily result in a stronger S_2 component in seismic velocity changes, suggesting that the local geo-hydrological variability

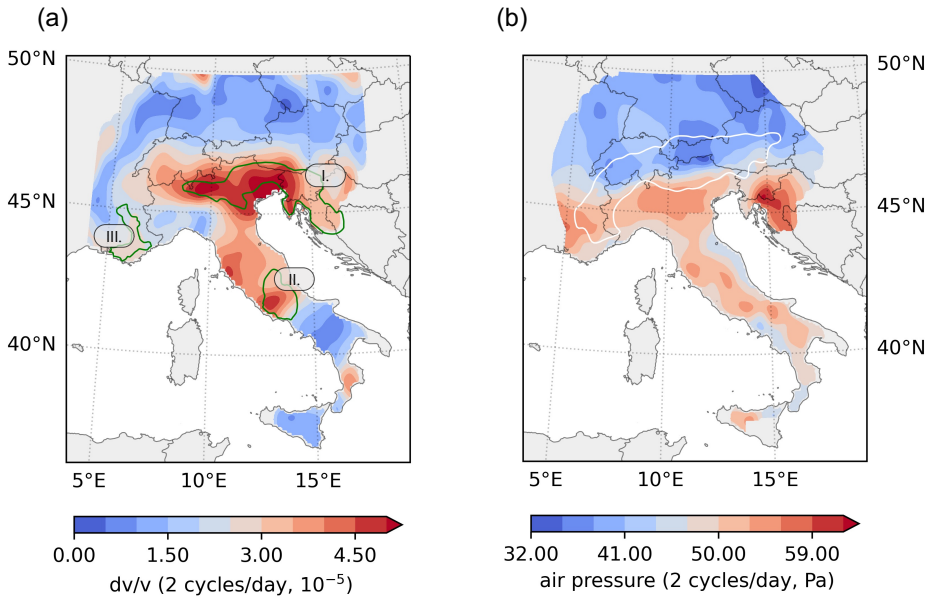


Figure 4.4.: Spatial distribution of the amplitude of S_2. (**a**) S_2 amplitude for seismic velocity change (dv/v). The green contours outline aquifers characterized by continuous carbonates, moderate to high permeability, and large pore size (Cornu et al., 2013; Chen et al., 2017; Xanke et al., 2022).(**b**) S_2 amplitude of air pressure oscillations. The white contour outlines the Alpine Mountains. (Note: the amplitude of the air pressure refers to a de-meaned time series. The amplitude of air pressure oscillations (about 50 Pa) is much smaller than the absolute value of sea-level pressure (about 10^5 Pa)

plays a crucial role in semi-daily velocity behavior.

4.3.3. Mechanisms explaining the velocity changes

The spatial correlation between semi-daily changes in seismic velocity and air pressure, as well as in previous studies (Kramer et al., 2023) suggest that air pressure is the main cause of semi-daily velocity variations. In the following we present the mechanisms underlying sub-daily seismic velocity changes and their implications for characterizing geo-hydrological features of shallow water reservoirs. Seismic velocity changes measured within the 0.5-1.5 Hz frequency range exhibit depth sensitivities highly restricted to the shallow subsurface (Qin et al., 2022; Fokker et al., 2023). As discussed earlier the only reasonable explanation for the sub-daily velocity changes are fluctuations in the air pressure above the observation point. As a direct effect, air pressure influences the unsaturated zone, causing compression during high air pressure and extension during low air pressure phases (Silver et al., 2007). Soils or weathered rocks, prevalent in the unsaturated zone, would experience significant water redistribution, thereby altering shallow seismic velocities.

Shallow seismic velocity changes, as demonstrated by (Solazzi et al., 2021), are strongly influenced by capillary effects in partially saturated soils. The capillary fringe, which is a thin layer above the water table between the unsaturated and saturated zones, responds to changes in pressure by rising or falling. This dynamic behavior of the capillary fringe is crucial as it mediates the relationship between air pressure fluctuations and alterations in seismic velocities. Understanding this relationship requires a conceptual grasp of the conditions in the subsurface. The subsurface medium comprises solid, fluid, and gaseous phases (Peck, 1960; Norum and Luthin, 1968). Above the water table, the pores of the solid phase are filled with water, entrapped air, and air that can move freely and is connected to the atmosphere (Peck, 1960). When air is disconnected from the atmosphere, it becomes entrapped air, unable to move freely due to blockages by the fluid phase (Norum and Luthin, 1968). If air is entrapped in the zone around the water table and within the capillary fringe, changes in air pressure will induce alterations in this zone, as it is compressible (Norum and Luthin, 1968; Turk, 1975). Under high air pressure, entrapped air compresses, occupying less pore space, and water from the saturated zone is drawn upward by capillary forces to fill this space. Consequently, this results in a decrease in the water table level and an expansion of the capillary fringe. Conversely, if air pressure decreases, entrapped air expands, pushing water downwards the water table, leading to a rise in the water table level and a reduction in the thickness of the capillary fringe (Turk, 1975). Fig. 4.5 illustrate this dynamic process. The impact of air pressure on changes in the water table varies considerably depending on the type of aquifer and can reach up to 6 cm (Turk, 1975). High air pressure results in a thicker capillary fringe, increasing saturation of the probed medium and causing a decrease in shear-wave seismic velocity (Toksöz et al., 1976; Mavko et al., 2009; Dong and Lu, 2016; Solazzi et al., 2021). Conversely, under low air pressure conditions, the opposite effect occurs. Laboratory experiments confirm that this effect occurs almost instantly (Norum and Luthin, 1968; Turk, 1975). Based on our experimental setting we found an average time delay between air pressure and dv/v of approx. 0.6 h (see Fig. B.5). The interplay among air pressure, water table, and capillary layer clarifies the observed negative correlation between the S2 component of seismic observations and atmospheric conditions (Fig. 4.3). It is important to note that other effects could also contribute to variations in the seismic velocity, e.g. changes in the pore pressure due to air pressure variations (Clements and Denolle, 2018) altering the seismic velocities. While this effect could further contribute to the velocity changes it is not able to explain the observed phase delays (Fig. B.5), since the reaction would be quasi-instantaneous.

4.3.4. Sub-daily seismic velocity changes as an indicator of vulnerable water reservoirs

Building upon the links established earlier a high amplitude in the of seismic velocity changes would indicate a strong interaction of air pressure with the subsurface. This reflects the connectivity that allows the air pressure to diffuse through the unsaturated zone. Delving into various (hydro)geological settings across Europe, we can discern specific conditions that favor this pronounced behavior.

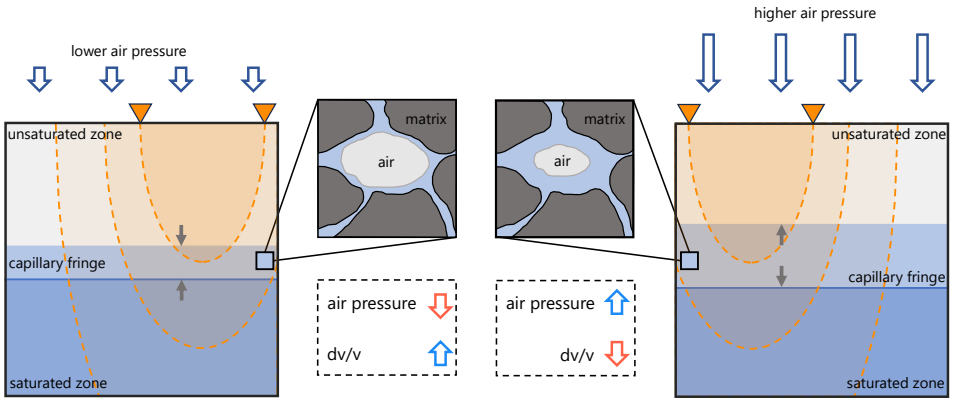


Figure 4.5.: Schematic evolution of the capillary fringe under different air pressure conditions. The left panel illustrates the decrease in capillary thickness under low air pressure, resulting in an increase in seismic wave velocity. The right panel depicts the process under high air pressure, where the capillary fringe becomes thicker with a lowered water table. The zoom-in in the middle shows the alteration in compressible air space with and without water infiltration (modified after Fabbri et al. (2019)). The orange shaded areas schematically represent the parts sampled by the coda waves.

The highest anomalies in Fig. 4.4a overlap with consolidated aquifers composed of continuous carbonate rocks exhibiting moderate to high permeability and large pore size, known as karst formations (Cornu et al., 2013; Chen et al., 2017; Nistor, 2020). This aquifer type is characterized by features such as caves, sinkholes, fractures, underground rivers and interconnected conduits (Ford and Williams, 2007). These features formed by corroding effects lead to a stronger secondary porosity, dominating the water regime (Ford and Williams, 2007). These properties enable karsts to effectively redistribute and infiltrate water in short periods, evident in a strong fluctuation of the water table (Serpelloni et al., 2018). This provides a unique setting to pronounce the semi-daily behavior of the seismic velocities. Particularly noteworthy are sinkholes and other openings to the atmosphere, such as fractures, which provide a direct path for air pressure to act on the capillary zone. This configuration within the geological formations presented here results in a stronger impact of air pressure changes. While we believe that the sub-daily variations are mainly driven by the atmospheric tides it is noteworthy that karst systems undergo further significant non-periodic changes due to meteorological and tectonic factors like presented in Barajas et al. (2021). Our spatial mapping reveals three significant groundwater reservoirs in Europe following this pattern.

Fig. 4.4a I. shows the karst in the southern calcareous Alps including the karst plateau and adjacent karst in the Dinarides (Chen et al., 2017; Xanke et al., 2022). It is the largest and most pronounced anomaly within our study. This might be due to the continuity of the

formation over a large area. Fig. 4.4a II. overlays with the Apennine carbonate platform in the central Apennines, recognized as a substantial water-bearing formation (Mantovani et al., 2019; Xanke et al., 2022). Our method images the central part of this formation. The third reservoir in southeastern France (Fig. 4.4a III.), located in the western Alps and the southern France basin (Xanke et al., 2022), is also identified with our method. However, this reservoir exhibits a less pronounced anomaly. We found two reasons for that. Firstly, the reservoir sustained by continuous karst is smaller compared to the others (Chen et al., 2017) and is closely located to discontinuous carbonates (Chen et al., 2017) and non-aquiferous rocks (Cornu et al., 2013). Secondly, the station coverage in this area is sparse, implying stronger smoothing.

Further notable geo-hydrological units across the study area are semi- to high-altitude mountain ridges such as the Alps or the Apennines. They are permeated with fissures and cracks (Somers and McKenzie, 2020) which are not necessarily intra-connected or open to the surface leading to trapping of the fluids and a lower level of permeability compared to other aquifer types. As a consequence of these geological attributes, these aquifers show a slower infiltration rate and interaction between air pressure variations and the subsurface in these regions is inherently limited. Another large-scale geo-hydrological unit is the Po Basin. It is characterized by marine deposits (Wendland et al., 2008), and accordingly, large pore sizes and high permeability (Cornu et al., 2013). While we observed a pronounced anomaly in the central-eastern Po Basin, drawing conclusions about its seismic response to semi-daily air pressure changes for its western part is difficult due to limited station coverage (Fig. 4.1b).

Our method provides a new assessment of barometric efficiency. This could be used to correct for air pressure influence in routine hydrological borehole measurements. To do so, it would be necessary to remove the actual air pressure force signal from the dv/v. By doing that it would be ensured that the results purely reflect the reaction of the system to those changes. Knowing which reservoirs are likely to have a stronger interaction with air pressure potentially help to get more precise groundwater level measurements (Rasmussen and Crawford, 1997). More importantly, it serves as a measure of vertical diffusivity (Hussein et al., 2013), which is closely linked to the vulnerability of the aquifer. Our technique allows large-scale mapping of this metric and therefore overcomes the point-wise character of the well-based method. Our study points out karst as a dominant feature in air pressure-subsurface interaction. This highlights the importance of this formation, since karst aquifers are renowned for their easy accessibility, making them an essential sources of potable water for approximately 25% of the world's population (Ford and Williams, 2007; Stevanovic, 2019). This accessibility makes them vital resources for buffering the increasing demand for water needed for both society and industry. Naming their essential role in water management, karst formations contribute significantly to sustainable water resources. However, the fast infiltration, permeability and flow patterns of karst formations also expose them to significant vulnerabilities, particularly in terms of contamination (Heinz et al., 2006; Ford and Williams, 2007; Stevanovic, 2015). Various contaminants can easily infiltrate these aquifers posing risks to both the environment and humans. In this regard, the method presented in this study offers the potential to effectively assess vulnerable aquifers which is essential for their responsible management and protection.

This entails large-scale mapping, exemplified in the context of southern-central Europe, and also more focused small-scale applications aimed at better understanding individual aquifers or hydrological units.

4.4. Challenges and limitations

Our study demonstrates the feasibility of extracting periodic patterns of dv/v from large regional arrays, with these patterns showing clear correlations to large-scale water reservoirs influenced by interactions between air pressure changes and the capillary zone. While assessing this important parameter yields valuable insights, it comes at certain costs.

One of the main challenges is stabilizing the dv/v measurements across long inter-station distances without losing the temporal component. As described earlier, we stacked the data over both time (4 years) and space (200 km), resulting in a smoothed representation across these dimensions. While this approach aligns with our primary objective, it imposes limitations and introduces potential ambiguities in data interpretation. The spatial smoothing imposes certain thresholds on the detectability of water reservoirs in our analysis. Larger and spatially continuous reservoirs are detectable through higher amplitude signals; however, when an aquifer is limited in size or discontinuous, averaging can reduce or obscure these signals, resulting in minimal or no detectable anomaly. By stacking and averaging our analysis over a 4-year period, we aim to exclude potential effects from non-periodic environmental drivers (e.g., precipitation) as well as natural variations, such as annual cycles of groundwater levels. Although this approach supports the interpretation of periodic behaviors on a large scale, it limits our sensitivity to these parameters. While our method effectively detects aquifers that exhibit strong interactions with air pressure changes - serving as an indicator of vulnerability - it is not capable of distinguishing between different aquifer types or aquifer depth. For instance, a strong interaction may occur in both karst systems with open channels and shallow sedimentary aquifers.

4.5. Conclusion

We have demonstrated the feasibility of investigating daily and sub-daily seismic velocity changes within large array settings. With an adapted coda-wave interferometry approach we are able to study the spatial variability of semi-daily seismic velocity changes. We associate fluctuations of air pressure with changes of the saturation in the capillary zone through an interplay between the fluid and the gaseous phase to explain the observed dv/v variations. This offers valuable information on the vulnerability of shallow water resources in southern-central Europe, particularly those with high connectivity, which exhibit a pronounced interaction with air pressure.

However, covering a vast area with different geological, hydrological and meteorological settings imposes certain limitations and challenges. One such challenge is ensuring reliable dv/v

measurements. While averaging over a distance helps stabilize measurements, it comes at the cost of spatial resolution, potentially omitting small hydrological formations.

To directly use them as a measure of barometric efficiency further steps are required. This includes the deconvolution of the air pressure force signal from the dv/v measurements. Further, seismic velocity behavior is a complex superposition of local characteristics. To account for that, some calibrations between the air pressure, groundwater depth, near-surface structure, and dv/v need to be done. Since these factors could be quantified locally, we anticipate that our method may be even more effective at local scales.

Consequently, studying semi-daily velocity variation, as a special case of dv/v monitoring becomes a tool for hydrology and even for environmental research. The seismic outputs, upon calibration and standardizing, may in principle serve as one of the core metrics or fundamental indices for the assessment of barometric efficiency, and evaluation of vulnerability. Further research could elevate this approach to a means of distinguishing various aquifer characteristics, beyond in-situ point-wise measurements. This may advance our comprehension of subsurface conduits, connectivity, permeability, and potential fault systems within the formation.

Establishing this kind of workflow as a time-lapse approach would help examine how these properties change over time that is essential for tracking environmental changes in the context of climate changes. Doing this would transform the regional seismic networks also into valuable hydrological monitoring systems. This could contribute to a comprehensive understanding of trends in the subsurface permeability and the karst formations, offering deeper insights into our water resources using passive seismology.

CRediT authorship contribution statement

R. Kramer: Writing – review & editing, Writing – original draft, Visualization, Software, Methodology, Investigation, Formal analysis, Data curation, Conceptualization. **Y. Lu:** Writing – review & editing, Supervision, Methodology, Data curation, Conceptualization. **Q.-Y. Wang:** Writing – review & editing, Supervision, Conceptualization. **S. Serafin:** Writing – review & editing, Data curation, Conceptualization. **A. Ceppi:** Writing – review & editing, Data curation, Conceptualization. **G. Bokelmann:** Writing – review & editing, Supervision, Conceptualization.

Declaration of Competing Interest

The authors declare that they have no known competing financial interests or personal relationships that could have appeared to influence the work reported in this paper.

Acknowledgements

The authors thank the editor, Hans Thybo, as well as Piero Poli and an anonymous reviewer for their questions and constructive feedback, which helped us improve our manuscript. We thank the operators of the permanent and temporary seismic networks across Europe who make the data available through EIDA (http://www.orfeus-eu.org/data/eida/). The authors thank the meteorological services of Germany (Deutscher Wetterdienst), Austria (Geosphere Austria), Switzerland (Bundesamt für Meteorologie und Klimatologie), France (MétéoFrance), and Slovenia (Slovenian Environmental Agency) for making their measurements accessible for this research. Further we thank Meteonetwork for compiling the data across Italy and making it available for us.

Data availability

The seismic data is available through EIDA (European Integrated Data Archive). This service is provided by ORFEUS (www.orfeus-eu.org). The meteorological dataset can be shared upon request.

Publication

The presented study (Kramer et al., 2025) was published in the Journal Earth and Planetary Science Letters on January 21, 2025.

Earth Planet. Sci. Lett. 653 (2025) 119223

Contents lists available at ScienceDirect

Earth and Planetary Science Letters

journal homepage: www.elsevier.com/locate/epsl

Identifying large vulnerable water reservoirs using passive seismic monitoring

R. Kramer [a,*], Y. Lu [a], Q.-Y. Wang [b], S. Serafin [a], A. Ceppi [c], G. Bokelmann [a]

[a] Department of Meteorology and Geophysics, University of Vienna, Vienna, Austria
[b] Institut Terre et Environnement de Strasbourg (ITES) UMR 7063, Université de Strasbourg, EOST/CNRS, Strasbourg, France
[c] Department of Civil and Environmental Engineering, Politecnico di Milano, Milan, Italy

ARTICLE INFO

Editor: H. Thybo

Dataset link: www.orfeus-eu.org

Keywords:
Seismic noise
Seismic monitoring
Near surface processes
Groundwater resources

ABSTRACT

Seismic waves capture important insights into subsurface behavior. We introduce an adapted coda-wave interferometry approach to monitor the spatial variability of semi-daily periodic seismic velocity changes on a regional scale, applied to data collected across South and Central Europe. Our results reveal a broad spatial correlation between seismic velocity changes and air pressure fluctuations, suggesting that air pressure is the dominant driving force. Specifically, air pressure fluctuations modulate saturation levels within the capillary zone through the dynamic interplay between fluid and gaseous phases, producing significant seismic velocity changes. The mechanism explains the large variations observed in regions with high connectivity between the surface and saturated zone. We associate this enhanced interaction with the high vulnerability of shallow water resources. We propose inspecting semi-daily periodic seismic velocity changes as a new tool for gaining a regional view of water reservoir vulnerability.

1. Introduction

Climate-change induced droughts and increasing industrial activity, have significantly intensified water demand (Megdal, 2018). Addressing these global challenges requires understanding and managing water resources to ensure a sustainable and resilient society and ecosystem (Mukherjee et al., 2018). In this context, shallow groundwater resources are broadly available and easily accessible and therefore particularly important (Wang et al., 2014; Gao et al., 2018). However, the high permeability and connectivity associated with shallow aquifer systems raise concerns about potential pollution and contamination (Al-Hashimi et al., 2021). Thus, acquiring a better understanding of the vulnerability of this water resource is imperative.

Aquifer vulnerability refers to the risk of pollution or contamination by substances such as chemicals or wastewater (Jang et al., 2017; Heinz et al., 2006). Methods and tools that allow constraining vulnerability are important to enhance awareness among decision-makers and the public, promoting secure water usage practices. The assessment of aquifer vulnerability commonly relies on measuring barometric efficiency (Hussein et al., 2013; Odling et al., 2015). This metric represents the susceptibility of the groundwater table to air pressure fluctuations, and it offers information about aquifer vertical diffusivity as a crucial determinant of vulnerability (Hussein et al., 2013). However, at present, measurements of barometric efficiency are confined to sparse point-wise borehole observations, subject to local geo-hydrological variabilities. This emphasizes the need for a novel efficient tool that can infer shallow aquifer properties at larger scales, ranging from individual reservoirs to regional hydrological units.

Recent studies (Clements and Denolle, 2018; Mao et al., 2022) have highlighted the potential of ambient noise seismology for imaging the shallow subsurface and for temporal monitoring beside registering seismic events. This approach can provide continuous tracking of (temporal variations) seismic velocities. Initially aimed at understanding the evolution of crustal stress associated with earthquakes (Brenguier et al., 2008; Obermann et al., 2014; Wang et al., 2019), many studies have also revealed that the observed seismic velocities are affected by environmental processes like seasonal temperature cycles, precipitation, snow, and air pressure fluctuations (Sens-Schönfelder and Wegler, 2006; Richter et al., 2014; Hillers et al., 2015; Wang et al., 2017; Gradon et al., 2021; Guillemot et al., 2021). Moreover, long-term investigations have drawn attention towards the notable impact of groundwater-level fluctuations on the seismic velocities (Sens-Schönfelder and Wegler, 2006; Gassenmeier et al., 2014; Lecocq et al., 2014; Voisin et al., 2017; Clements and Denolle, 2018; Rodríguez Tribaldos and Ajo-Franklin,

* Corresponding author.
E-mail address: richard.kramer@univie.ac.at (R. Kramer).

https://doi.org/10.1016/j.epsl.2025.119223
Received 16 July 2024; Received in revised form 24 November 2024; Accepted 14 January 2025

Available online 21 January 2025
0012-821X/© 2025 The Author(s). Published by Elsevier B.V. This is an open access article under the CC BY license (http://creativecommons.org/licenses/by/4.0/).

4.6. Extended Discussion

This study is the first to systematically examine the daily and sub-daily behavior of seismic velocity across Europe. By analyzing four years of continuous ambient noise recordings from hundreds of stations, we were able to extract small changes in seismic velocity at this scale for the very first time. This combination of broad spatial coverage and fine temporal resolution opens up new possibilities for passive seismic monitoring of groundwater dynamics, while also highlighting the computational and methodological challenges associated with continental-scale studies. Despite the promise of using passive seismic dv/v monitoring to map aquifer vulnerability on a large scale, several limitations must be acknowledged and investigated further.

One crucial point that requires further analysis is the complex issue of depth sensitivity. While most studies approximate the depth sensitivity of coda waves to that of surface waves, we believe it also depends on the kernel of the actual subsurface forcing. Furthermore, the analysis of sensitivity kernels shows a peak of sensitivity near the surface, which would support our hypothesis. Whether this is true can only be clarified with further research. Additionally, our analysis simplifies certain geological and hydrological settings. One example is the potential variability of capillary fringe depths. Depths can vary from a few meters to much greater depths depending on the geological setting. Moreover, medium properties, such as porosity and elastic modulus, evolve with depth. Local investigations with ground-truth datasets about hydrological conditions would clarify this and increase the potential applications of this method.

By averaging four years of continuous recordings, we can suppress non-periodic water-table drifts, e.g. seasonal recharge, and isolate periodic signals. As discussed in the publication we ruled out other possibilities that could cause the S_2 periodicity. However, temperature-driven velocity changes or shifts in the distribution of ambient noise sources can each induce fluctuations in dv/v that could interfere with the influence of atmospheric pressure.

Our theoretical framework assumes a laterally homogeneous subsurface in which dv/v varies with changes in saturation within the capillary zone. However, real aquifers exhibit spatially variable porosity, permeability, and fracture networks, which could produce non-linear and anisotropic seismic responses. To confirm that these variations reflect changes in the capillary fringe, it is crucial to validate this assumption against independent hydrological datasets, such as water heads and soil moisture measurements.

Resolving these issues is beyond the scope of this thesis. An approach would be to deploy dense arrays at well-characterized field sites for joint seismic-hydrological calibration. By explicitly articulating these challenges, we aim to clarify the limitations of our passive seismic approach and lay the foundation for future studies to establish a stronger link between seismic velocity changes and groundwater dynamics.

5 Monitoring Groundwater Pumping Using Time-Lapse Tomography from Ambient Seismic Noise

Abstract

Management of water resources will be of critical importance as the effects of climate change accelerate. This implies the need to monitor water resources with high spatial and temporal resolution. One way to meet this need could be passive seismic methods using ambient seismic noise. In this study, we present a novel approach using time-lapse probabilistic tomography to monitor a hydrological pumping test in the municipality of Nickelsdorf (Austria). We deployed a dense array of nodal seismic sensors that recorded seismic noise for approximately 4 months in early 2023. To assess changes in subsurface properties associated with the pumping, we conducted trans-dimensional probabilistic tomography with daily time resolution using train-generated noise. Our results show a clear correlation between water table fluctuations and shear wave velocities. We interpret this to be due to variations in saturation caused by groundwater pumping. Mapping these spatio-temporal variations enables water resource monitoring that complements well-based point-wise measurements. Such an approach can lead to improved understanding of groundwater dynamics such as inflow from external water resources.

- We showed the feasibility of using time-lapse probabilistic tomography for monitoring a hydrological pumping test.
- We can clearly identify the phases of pumping in the group velocities and the resulting shear wave velocity models.
- Changes in shear waves are coupled to fluctuations in the saturation of unconsolidated sediments in response to water level oscillations.

Plain Language Summary

As climate change increases the challenges of water management, our study presents a new method that uses the Earth's natural vibrations to monitor changes in the subsurface associated with fluctuating groundwater levels. During a water pumping test in Nickelsdorf, Austria, we set up a dense array of low-cost seismic sensors that captured recordings of seismic waves over four months. We created maps showing how the speed of these waves in the ground varies in space and time, related to variations in water saturation. The clear correlation we found between water table fluctuations and wave velocity suggests that this approach can effectively monitor changes in soil moisture caused by pumping. In addition to bridging the gap between punctual well measurements and large-scale groundwater assessments, this method provides a practical and cost-effective tool for managing water resources in a changing climate.

5.1. Introduction

Growing population and industrial activity expansion lead to an increased demand for water (Megdal, 2018), making it a critical resource (Richey et al., 2015). In order to meet this demand, there is a need to responsibly manage its use. A major component of the readily available and accessible water on Earth is shallow groundwater (Wang et al., 2014; Gao et al., 2018) and its relevance is emphasized by the acceleration of global warming and its consequences (Mukherjee et al., 2018). One of the main challenges in hydrological research is the spatial and temporal coverage of observations. Traditionally, hydrological observations are based on well-based measurements (Taylor and Alley, 2001). This type of observation has two main limitations: (a) it is a point measurement, representing the behavior of the aquifer only at a specific location. Given the heterogeneity of aquifer systems (Wang et al., 2024a), such observations provide an incomplete description of the system. (b) The cost of drilling remains high and can have significant environmental impacts, such as the removal of vegetation, which can disrupt soil systems and natural habitats (Jones et al., 2015).

Current approaches to bridge the gap between point measurements are diverse. The two most common approaches are hydrogeodesy (White et al., 2022) and hydrogeophysics (Binley et al., 2015). Geodetic measurements include Global Navigation Satellite System (GNSS) measurements to track ground deformation at local stations (King et al., 2007; Ji and Herring, 2012; Young et al., 2024). Another commonly used method is InSAR (Interferometric Synthetic Aperture Radar), which uses differences in the phase of between emitted and backscattered radar waves measured by satellites to measure ground deformation (Bawden et al., 2001; Watson et al., 2002; Lanari et al., 2004; Bell et al., 2008; Chaussard et al., 2014; Rezaei and Mousavi, 2019). The most common methods in hydrogeophysics include dc resistivity measurements, ground penetrating radar, induced polarization, and nuclear magnetic resonance (Topp et al., 1980; Rubin and Hubbard, 2006; Vereecken et al., 2006; Robinson et al., 2008; Binley et al., 2015). While each of these methods provides direct or indirect information about water content, permeability, or pore water conductivity, their effectiveness may be limited under certain conditions, particularly in environments with high electrical conductivity or resistivity, or in soils with significant clay content (Romero-Ruiz et al., 2018; Pathirana et al., 2023).

Another component of hydrogeophysics is active seismic exploration. Their advantage over other methods lies in their ability to provide high-resolution images of the subsurface. However, the application of reflection and refraction seismic methods has so far remained sparse. This is due to the fact that their implementation is costly and does not allow continuous monitoring. One way to overcome this problem is to use passive seismology, also known as ambient noise seismology. Unlike active seismic surveys, which rely on discrete sources such as explosions or vibroseis trucks, passive seismology takes advantage of the continuous ambient wavefield generated by both natural and anthropogenic sources. By cross-correlating the noise recorded by two seismic sensors, it is possible to estimate the Green's function between them (Derode et al., 2003; Wapenaar, 2004; Weaver and Lobkis, 2004). The reconstructed wavefield consists

of both ballistic surface waves and multiply-scattered coda waves. By applying the principles of coda-wave interferometry (Snieder et al., 2002), it is possible to establish a continuous monitoring setup that measures relative seismic velocity changes (dv/v) that indicate variations in the physical properties of the medium. It was originally developed to monitor geological processes such as the pre-eruption phases of volcanoes (Brenguier et al., 2014; Obermann et al., 2013b) or structural changes after large earthquakes (Brenguier et al., 2008a; Ikeda and Tsuji, 2018; Wang et al., 2019), coda-wave based monitoring has also proven valuable for understanding environmental impacts on the subsurface (Wang et al., 2017; Hillers et al., 2015a; Kramer et al., 2023; Wang et al., 2024b) and even hydrological constraints (Sens-Schönfelder and Wegler, 2006; Lecocq et al., 2014; Voisin et al., 2016, 2017; Rodríguez Tribaldos and Ajo-Franklin, 2021; Kramer et al., 2025). However, the main drawback of using coda waves for monitoring is their complex sensitivity kernels and multi-scattering origin, which complicates the localization of velocity perturbations in the subsurface (Pacheco and Snieder, 2005; Larose et al., 2010). Although studies suggest an empirical relationship between changes in dv/v and water level (Voisin et al., 2017; Gaubert-Bastide et al., 2022), or use coda wave sensitivity kernels to map dv/v variations to depth (Margerin et al., 2015; Mayor et al., 2014; Mao et al., 2022), a straightforward interpretation for hydrologists remains a challenge.

Another approach to continuous monitoring in noise is time-dependent tomography using surface waves. Unlike coda waves, the sensitivity kernels of surface waves are well understood, making it easier to localize the origin of velocity changes (Voisin et al., 2017; Kim and Lekic, 2019; Garambois et al., 2019). However, few time-lapse tomography studies using ambient noise have been performed to date (de Ridder et al., 2014; Stork et al., 2018; Guo et al., 2024), and even fewer in hydrological applications (Sobolevskaia et al., 2024). Compared to coda-wave interferometry, time-lapse tomography is more difficult to implement. One reason for this is the need for a strong, stationary, repeating noise source field with a wide frequency range, as surface wave reconstruction from noise correlation is more sensitive to noise source variability (Paul et al., 2005; Gouédard et al., 2008; Froment et al., 2010; Hadziioannou et al., 2011). Another crucial factor is the choice of the right methodological framework for the inversion. For instance, classical linearized inversion is often subject to the choice of regularization (damping and smoothing) parameters, which can bias the relative velocity perturbations derived from data of different time periods.

In this study, we investigate the potential of passive seismic imaging for monitoring. We take advantage of a controlled experiment conducted in early 2023 near the village of Nickelsdorf in Burgenland, Austria. In addition, we benefit from a relatively dense network of groundwater level measurements along our deployed seismic profile, which allows us to compare these data with the results from our seismic analysis. The purpose of this study is to test the hypothesis that we can measure shear wave velocity changes as a result of saturation changes due to groundwater pumping in a field experiment. It will also help to identify the nature of velocity changes observed in various other applications. We overcome the aforementioned methodological challenges by using repetitive passing trains and an objective, fully data-driven probabilistic inversion scheme.

5.2. Integrated Hydrological and Seismic Monitoring of a Groundwater Pumping Test in Nickelsdorf (Burgenland, Austria)

5.2.1. The Pumping Test Site

The test site is located near the village of Nickelsdorf in the state of Burgenland (Austria, Fig. 5.1). More specifically, it is located between the Leitha River and railroad tracks used by local and international freight and passenger trains. Two wells at the test site, EKB5 and EKB7 (Fig. 5.1), provide lithological logs (see Fig. C.1). Four other wells served as observation wells. Geologically, the Nickelsdorf area is dominated by the eastern end of the Parndorf Plate (also Parndorf Plateau or Parndorf Plain). The Parndorf Plate consists of several soil layers of the Pleistocene Danube valley, mainly gravel and sand (Pascher et al., 1999; Schnabel et al., 2002). The base of the gravel layer is characterized by sandy deposits from Lake Pannon or calcareous-dolomitic and silty-clayey deposits (Fuchs et al., 1985). Hydrologically, the area is characterized by local (separated) groundwater resources of higher productivity or extensive groundwater resources of average productivity (GeoSphere Austria, 2025). The dominant aquifer type is porous aquifers (GeoSphere Austria, 2025), characterized by low groundwater flow velocities, high groundwater storage capacity, and good filtration properties (Domenico and Schwartz, 1997).

5.2.2. Pumping Tests in Nickelsdorf - a Brief Hydrological Perspective

The extraction of groundwater from the subsurface is a common practice today, especially in agriculture (Qureshi et al., 2010). This highlights the growing reliance on shallow groundwater resources, which are often favored for their high quality and accessibility, especially in regions experiencing population growth or seasonal fluctuations in surface water availability (Wang et al., 2014; Gao et al., 2018). To ensure the productivity of these wells and to mitigate the impact on the productivity of nearby wells, pumping tests must be conducted before new groundwater wells are put into operation. The municipality of Nickelsdorf aims to improve its water supply by using groundwater from shallow aquifers. To meet legal and regulatory requirements, it is necessary to perform pumping tests, which are a standard method to evaluate the properties of the aquifer (Austrian Water Act, 1959; ÖNORM ISO 22282-4:2021, 2012).

A pumping test involves the active extraction of water from an aquifer using a pumping well while simultaneously monitoring the groundwater level (GWL) at several observation wells located around the pumping site (Kruseman et al., 1970; Domenico and Schwartz, 1997). The primary objective is to observe how the aquifer responds to water extraction over time and space (see Fig. 5.2a). By analyzing the water levels in response to pumping, several key hydraulic parameters can be determined (Theis, 1935; Kruseman et al., 1970):

1. hydraulic conductivity, which is a measure of the ease with which water can flow through the aquifer material, providing insights into the permeability of the subsurface (e.g., Bear, 1979; Freeze and Cherry, 1979),

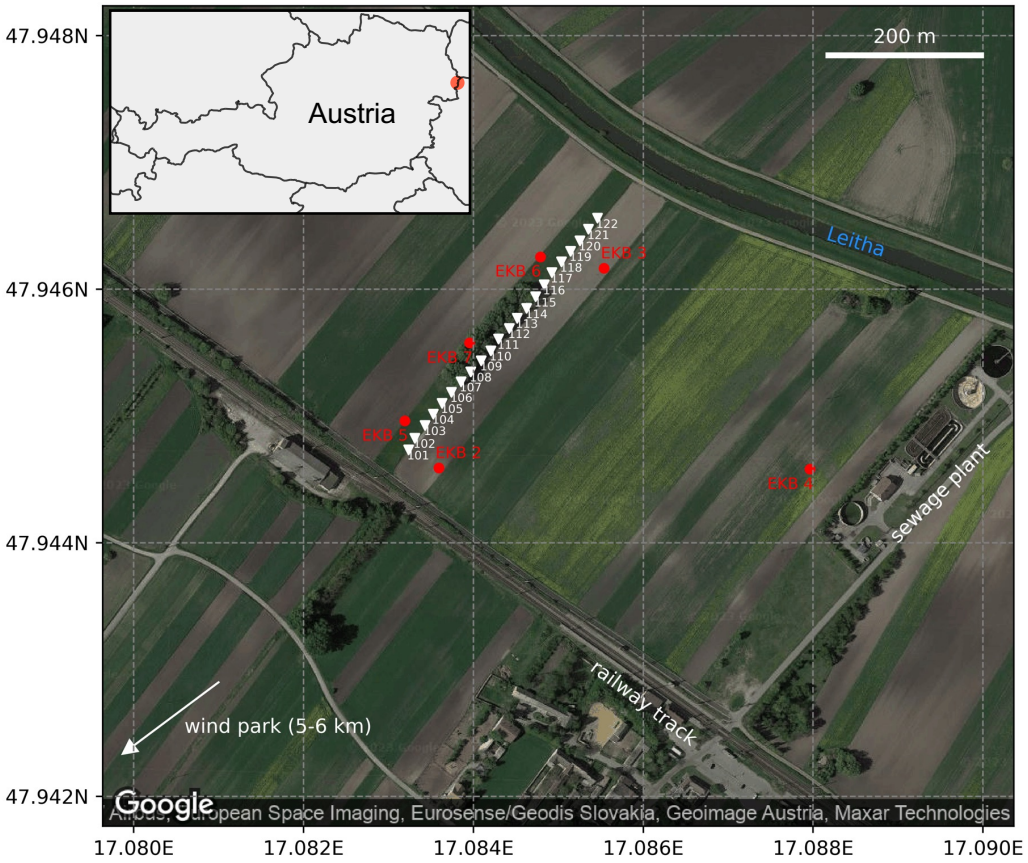


Figure 5.1.: The Nickelsdorf pumping test site showing locations of nodal seismic sensors (white triangles), hydrological wells (red circles) and local characteristics. The inset shows the location of the site within Austria.

2. transmissivity, which combines the hydraulic conductivity and the aquifer thickness, reflecting the ability of the aquifer to transmit water laterally (e.g., Theis, 1935; Domenico and Schwartz, 1997), and

3. storage coefficient, which is a metric which quantifies how much water the aquifer can store or release per unit area per unit change in hydraulic head (e.g., Bear, 1979).

These parameters are critical to understanding the productivity of the aquifer, assessing its sustainable yield, and predicting how it will respond to prolonged pumping (Custodio, 2002; Todd and Mays, 2004). In addition, they help to estimate recharge rates (Singh et al., 2019; Gumuła-Kawęcka et al., 2022), which are essential for managing water resources sustainably and preventing over-extraction that could lead to problems such as land subsidence, reduced water quality, or ecological damage (Sophocleous, 2003; Galloway and Burbey, 2011; Chen et al., 2020).

To evaluate the characteristics of the shallow and productive aquifer at Nickelsdorf, a controlled pumping test was conducted. The pumping test consisted of three main phases. In the first phase, the pump was activated in well EKB7 (Fig. 5.1 and Fig. 5.2c), while all other wells served as observation wells. In the second phase, pumping was performed in well EKB5 (Fig. 5.1 and Fig. 5.2b). In the last phase, pumping took place in the two wells (Fig. 5.2b, c).

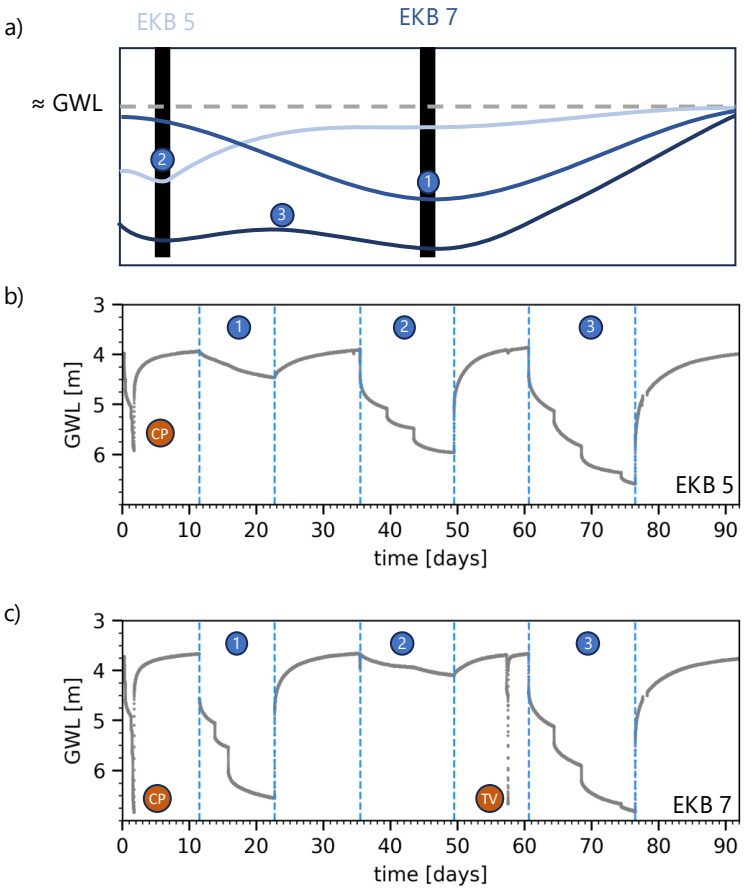


Figure 5.2.: Hydrological characteristics of the pumping tests. Panel **a)** shows a schematic view of the lowering of the groundwater table for each pumping phase. In panel **b)** and **c)** the groundwater levels (GWL) of the two wells EKB5 and EKB7 are presented. The encircled numbers are the phases of the pumping test, while the abbreviation "CP" stands for clear pumping and "TV" marks the time of the demonstration for the TV broadcast station.

Within these main phases, the pumping rate was increased from 12 l/s to 20 l/s. The combined pumping rates ranged from 23 l/s to 40 l/s. To capture the hydraulic behavior of the aquifer, the wells are equipped with piezometers to measure the depth of the groundwater table. The groundwater level time series (GWLTS) for the two pumping wells are shown in Fig. 5.2. In

addition to the typical water level declines caused by pumping, several smaller events can be observed in the GWLTS. Prior to the start of the pumping tests, the pipes are cleaned (CP - clear pumping) to remove gravel and sand, resulting in a sharp drop in water level. In addition, a sharp decrease in the water table can be observed around day 58, resulting from a demonstration of the experiment for the national television channel. Fig. 5.2a shows the schematic behavior of the water table due to pumping activities in the respective well. The drawdown is expected to be localized around the pumping well. However, due to the limited number of wells and piezometers, it is not possible to define precise spatial constraints.

5.2.3. Seismic Monitoring of the Nickelsdorf Pumping Tests

Our seismic experiment was planned as a complementary monitoring tool to a pumping test. The idea behind seismic investigations in the context of hydrological monitoring is the dependence of the surface wave velocity on the water saturation of the subsurface (Dong and Lu, 2016; Solazzi et al., 2021). Several studies have shown that it is possible to derive this behavior of coda and surface waves from ambient noise (e.g., Sens-Schönfelder and Wegler, 2006; Voisin et al., 2017; Clements and Denolle, 2018; Sobolevskaia et al., 2024). The potential of combining coda wave interferometry and tomography in controlled hydrological experiments is also demonstrated (Gaubert-Bastide et al., 2022). Time-lapse surface wave tomography from ambient noise has not yet been performed in such an environment. The working hypothesis for setting up the experiment was that local water table depletion (Fig. 5.2a) leads to significant changes in the saturation regime near the pumping wells, while the other parts of the profiles experience only minor changes. This contrast should be observed in the seismic velocities. To capture the velocity changes in the subsurface associated with pumping, we installed $\sim$ 50 seismic sensors, recording for approximately 4 months in 3 deployment phases. Each instrument is a Fairfield-Nodal Zland three-component sensor with a 5-Hz cutoff frequency. In total, we collect a dataset of 93 days from mid-January to mid-April 2023, while only one sensor (106) suffered a segmentation error in the first phase of our experiment. For this study, we focus on a dense profile of seismic nodes (see Fig. 5.1) crossing the two pumping wells EKB5 and EKB7.

5.3. Seismic Data Processing

We applied the following preprocessing steps to the continuous raw seismic data: detrending, instrument response removal, bandpass filtering, glitch removal, and spectral whitening. Before correlating the signals from two seismic sensors, we first performed data selection. The railway line perpendicular to the profile is frequently used, with up to 150 trains passing daily. We exploit this strong noise source by treating it as a permanent source (Rebert et al., 2024). To identify time windows corresponding to train passages, we use an STA/LTA (short-term average/long-term average) trigger (Allen, 1978), which detects rapid changes in the amplitude of the seismic signal relative to a background level. Train detections are made at station 101 (see Fig. 5.1), the station closest to the railway line. A time window is then defined around these events for correlation analysis. We then rotate the north, east, and vertical

components into the radial, transverse, and vertical components (Roux, 2009). We computed cross-correlations of 2-minute segments and then stacked these for every hour to increase the signal-to-noise ratio. The cross-correlation function between two stations represents the estimated Green's function, which is the impulse response of the Earth to a point source. It can be thought of as a wave traveling from one station (virtual source) to the other station (receiver). Changes in the properties of the medium induced by the groundwater pumping experiment can be inferred from the repeatedly reconstructed wave field as it propagates through the subsurface. Classically, noise interferometry is performed with sources that are ideally distributed uniformly around the station pairs. In our case, we have a strongly directional source, which means that most of our energy is on the causal part (positive lags) of the correlations (see Fig. 5.3b).

Inspection of the correlations over distance and time reveals not only a propagating fundamental mode surface wave, but also higher modes of surface waves (Fig. 5.3). These higher modes are more pronounced under certain conditions, such as shallow seismic sources, or strong velocity contrasts in the subsurface (Tokimatsu et al., 1992; Liu and Fan, 2012; Rivet et al., 2015; Ji et al., 2021). They usually have greater penetration depths and can sample deeper structures within the Earth (Rivet et al., 2015). Finally, their dispersion characteristics may overlap with the fundamental mode, making them difficult to distinguish (Rivet et al., 2015).

Inspection of the hourly cross-correlations in Fig. 5.3b reveals the variations associated with the pumping experiment. A decrease in the travel time of the surface wave is observed during all pumping cycles. Conversely, the travel time increases during the period of reservoir replenishment. The strength of the effect is directly related to the distance between the receiver pair and the pumping well. The higher mode shows a similar pattern and could potentially be used to further constrain the inversion. This study focuses on the fundamental mode of the surface waves. It is therefore important to select the correct wave train for dispersion analysis. To minimize the influence of the higher modes, we apply a frequency-wavenumber (f-k) filter that exploits the different propagation velocities (Capon, 1973; Morton and Crotwell, 2015).

5.4. Towards Time-Lapse Tomography of Active Hydrological Experiments

For each station pair, we pick the Rayleigh group dispersion. We have limited our temporal resolution to daily measurements by stacking the hourly cross-correlations of a given day, which means that 93 dispersion curves are selected for each station pair. For the dispersion measurement we follow the approaches of Dziewonski et al. (1969) and Levshin et al. (1989) while incorporating the frequency re-centering method introduced by Shapiro and Singh (1999) (see Fig. 5.4). Before inversion, the picks are checked and outliers are removed. To do this, we calculated the median of all dispersion picks for all days of each station pair. Picks outside of two standard deviations are considered outliers and are removed. This is crucial to ensure stable results for time-lapse tomography (see Fig. C.2).

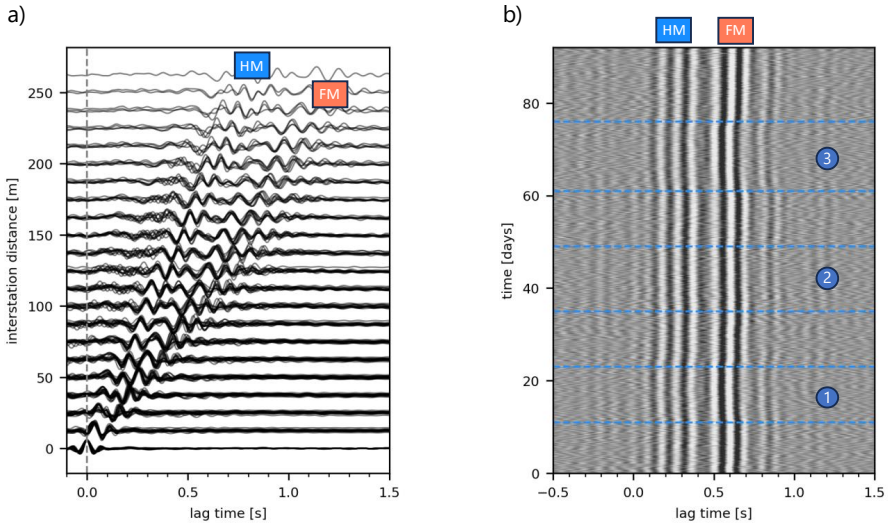


Figure 5.3.: Seismic waveforms from correlations of train generated noise. **a)** is the distance-time plot for all correlations stacked over the whole time period. **b)** shows the correlations over time for a representative station pair "104-113". The abbreviations "HM" and "FM" refer to higher mode and fundamental mode. The encircled numbers are the phases of the pumping test and the blue lines bound the time periods of each pumping test.

We extracted the measured group velocities for different frequencies for station pair "104-113", a station pair that crosses well EKB7, to illustrate its behavior over time (Fig. 5.5b). The changes are clearly visible for frequencies between 10.2 Hz and 15 Hz (sensitive to the top few meters of the subsurface). With a decrease in the GWL an increase in the group velocities is observable. This relation is expected due to the decreasing saturation in the media, which is associated with an increase in seismic velocity (Mavko et al., 2009; Schoen, 2015). The changes in group velocity are in the order of 15 % for the last pumping cycle, associated with the highest pumping rates and the lowest GWL. Interestingly, the clear pumping activity at the first day is also visible as a sharp velocity increase. Other events, such as the demonstration for the TV broadcast, are not resolved because their event durations fall below our daily resolution. The magnitude of the velocity change correlates with the distance to the pumping well. While the effect is quite strong for pumping cycles 1 and 3 (EKB7), it is smaller for pumping cycle 2 (EKB5). We aim to leverage this trend to potentially derive spatial constraints on the lowering of the groundwater table around the well.

Our inversion procedure follows the classic two-step approach. First, we invert the group-velocity dispersion measurements for each day to obtain the group velocity structure with associated uncertainties along the seismic profile. Then, we extract dispersion curves along the same profile and invert for 1-D shear-wave velocity structure.

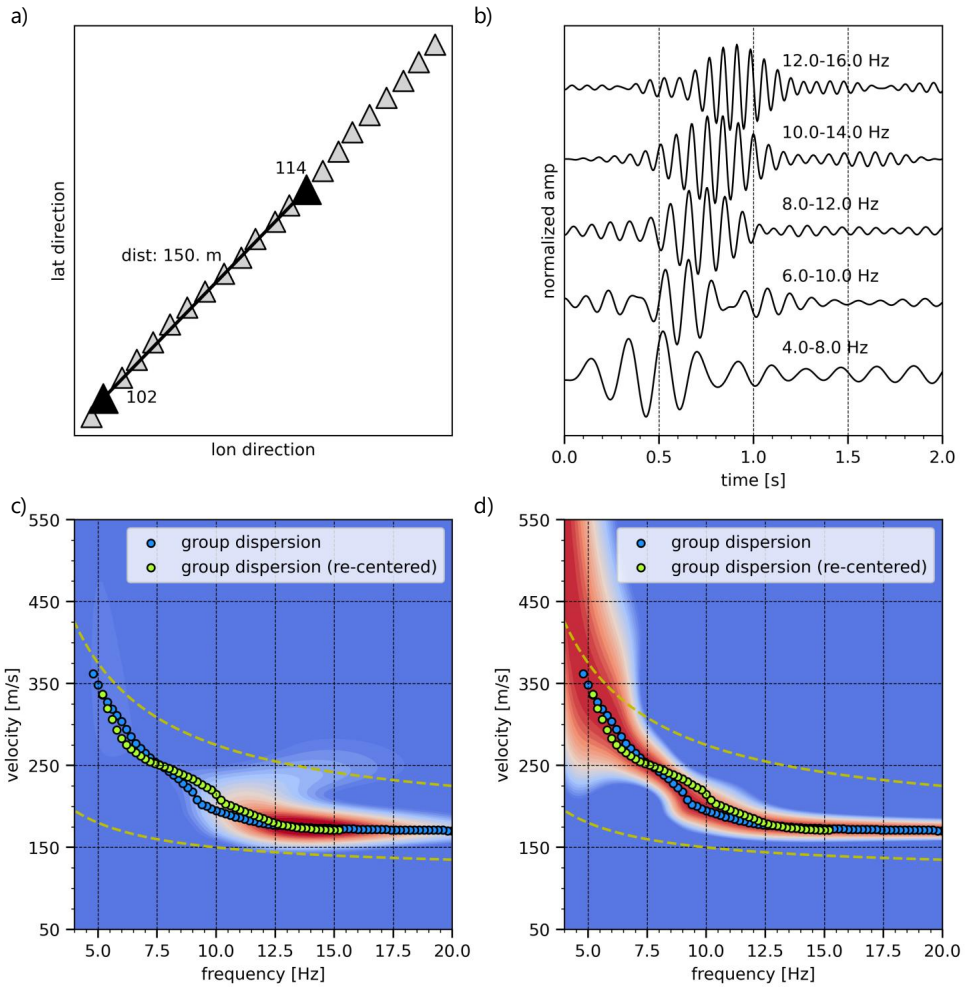


Figure 5.4.: Dispersion analysis of station pair "102-114". **a)** Seismic profile with stations in gray, the analyzed station-pair is highlighted in black and has an inter-station distance of 150 m. **b)** Normalized cross-correlations filtered into different frequency bands. **c)** Dispersion analysis normalized by the maximum of the signals and **d)** by the maximum in every frequency band. The blue dots represent the picked dispersion curves, while the green dots are the re-centered picks. The yellow dashed lines indicate a lower and upper bound for the group velocities to guide the automated picking.

5.4.1. Inversion of 2-D Group Velocity Profiles

We perform inversion of Rayleigh wave group velocity dispersion measurements within a probabilistic framework for individual days. This method eliminates the need for subjective regularization decisions that might compromise a meaningful uncertainty analysis, and it also avoids relying on user-defined selections of model complexity. This approach yields an

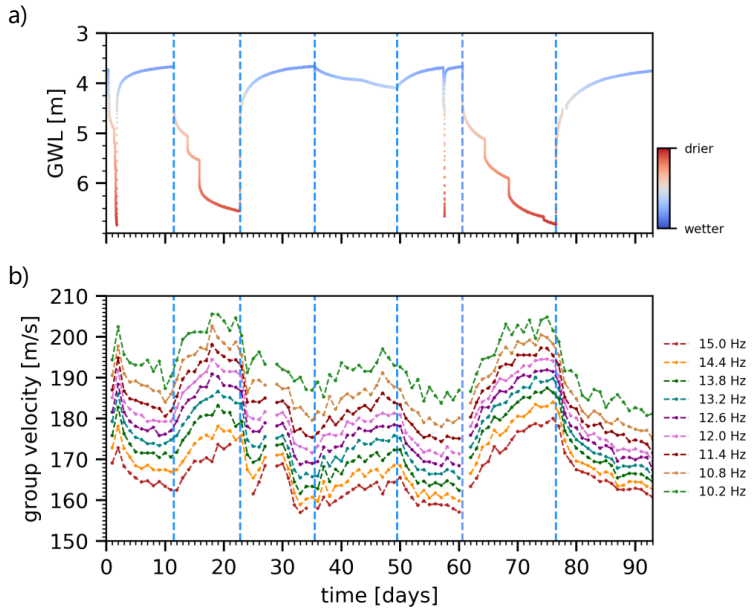


Figure 5.5.: Temporal evolution of group velocities for station pair "104-113". **a)** Groundwater level but color coded for well EKB7. Blueish colors means higher water saturation in the subsurface, while reddish color indicate the opposite. **b)** Group velocities of different frequencies over time in the experiment. Note that, the two gaps are associated with field work and replacement of instruments.

approximation of the posterior probability density (PPD) for the parameters that define the 2-D group velocity profile, allowing us to estimate group velocities along with their associated uncertainties. We establish broad, bounded, uniform prior distributions (see Tab. C.1). In this study, we use a modified version of the tomographic method introduced by Gosselin et al. (2021) and Esteve et al. (2025). Instead of inverting dispersion measurements at individual frequencies, we simultaneously invert Rayleigh wave group velocity dispersion data across the 5–15 Hz frequency range, with a 0.2 Hz increment. By using this implementation, velocity jumps between adjacent frequencies are only introduced when required by the data. In contrast, independent inversions for each frequency often yield velocity jumps attributed to numerical artifacts and model uncertainty. Our approach results in more realistic 2-D group velocity profiles. Uncertainties cannot be rigorously determined from the Rayleigh-wave group velocity dispersion measurements. Therefore, we treat Rayleigh-wave travel time uncertainties as unknowns that are solved for as part of the inversion procedure. The uncertainty associated with the Rayleigh-wave travel time is defined by:

$$\sigma_i = a\Delta_i + b + c \cdot f, \tag{5.1}$$

where Δ_i is the source-to-station distance for path i, f is the frequency and a, b and c are three unknown hyper-parameters. Previous studies have proposed probabilistic tomography

with similar hyperparameters to characterize data error dependence on inter-station distance (Bodin et al., 2012; Gosselin et al., 2021). The inclusion of a frequency-dependent term (and parameter c) is a novel improvement that allows for data-error variability between frequencies. This error model allows each travel time to have a unique uncertainty while only requiring three additional parameters in the inversion. An example of the PPDs for the parameters a, b and c is shown in Fig. C.3.

The 2-D group velocity profile is represented using a set of nodes, each defined by its position (in distance and frequency space) and an isotropic Rayleigh wave group velocity. The inversion follows a trans-dimensional approach, meaning that both the number of nodes and their spatial distribution are determined during the inversion process. In order to approximate the PPD of the model parameters, we employ the reversible-jump Markov-chain Monte Carlo (rjMcMC) method (Green, 1995) to produce a large ensemble of samples (200 million). We select random starting velocity models within the prior bounds for 40 interacting rjMcMC chains. Each chain generates 5 million samples, with the initial 10,000 discarded as burn-in samples that may be more dependent on the starting model. The mean and standard deviation of the remaining samples are calculated at each location within the 2-D profile, providing a representative model along with its associated uncertainty.

Fig. 5.6 shows the group velocity profile (Fig. 5.6a, b, d, e) and the associated uncertainties (see Fig. C.4) for days 9, 20, 59 and 75. An animation with all 93 days can be found in the digital supplement Mov. C.7. Days 9 and 59 represent the start of the respective pumping cycles at EKB7 (see Fig. 5.6c), while days 20 and 75 roughly represent the end of the cycles. The velocities for all models presented range from about 140 m/s to 1000 m/s. Comparing the models reveals some similarities and differences. In general, the features within the maps are comparable. At the beginning of the profile between 5 Hz and 10 Hz, the group velocities are faster compared to the rest of the profile between 600 m/s and 1000 m/s. In addition, a low-velocity zone (green rectangle) below well EKB5 can be observed in the results except for day 75. The most noticeable changes are in the vicinity of well EKB7. Before pumping (Fig. 5.6a, d - blue rectangle) a low velocity zone can be seen around well EKB7. After pumping (Fig. 5.6b, e - blue rectangle) the extent of this zone has shrunk. There is also a slight increase in velocities at lower frequencies below the indicated EKB7 well. To show the variability of the inverted group velocity, we have averaged the velocities of the frequencies of the profiles corresponding roughly to the station pair "104-113" for comparison (see Fig. C.5). The velocities match each other, and the behavior related to pumping is imprinted in the inverted group velocity results.

The uncertainties obtained from the inversion vary between about 1 m/s and 400 m/s, directly reflecting the sparse ray coverage at the beginning and end of the profile. In addition, there is a lack of data for lower frequencies, which results in a higher uncertainty. For high frequencies in the central part of the profile, we observe low uncertainties. Both of the low-velocity features mentioned above have low uncertainties, which makes us confident in them as signatures of pumping activity. This intermediate step already highlights the potential of the imaging

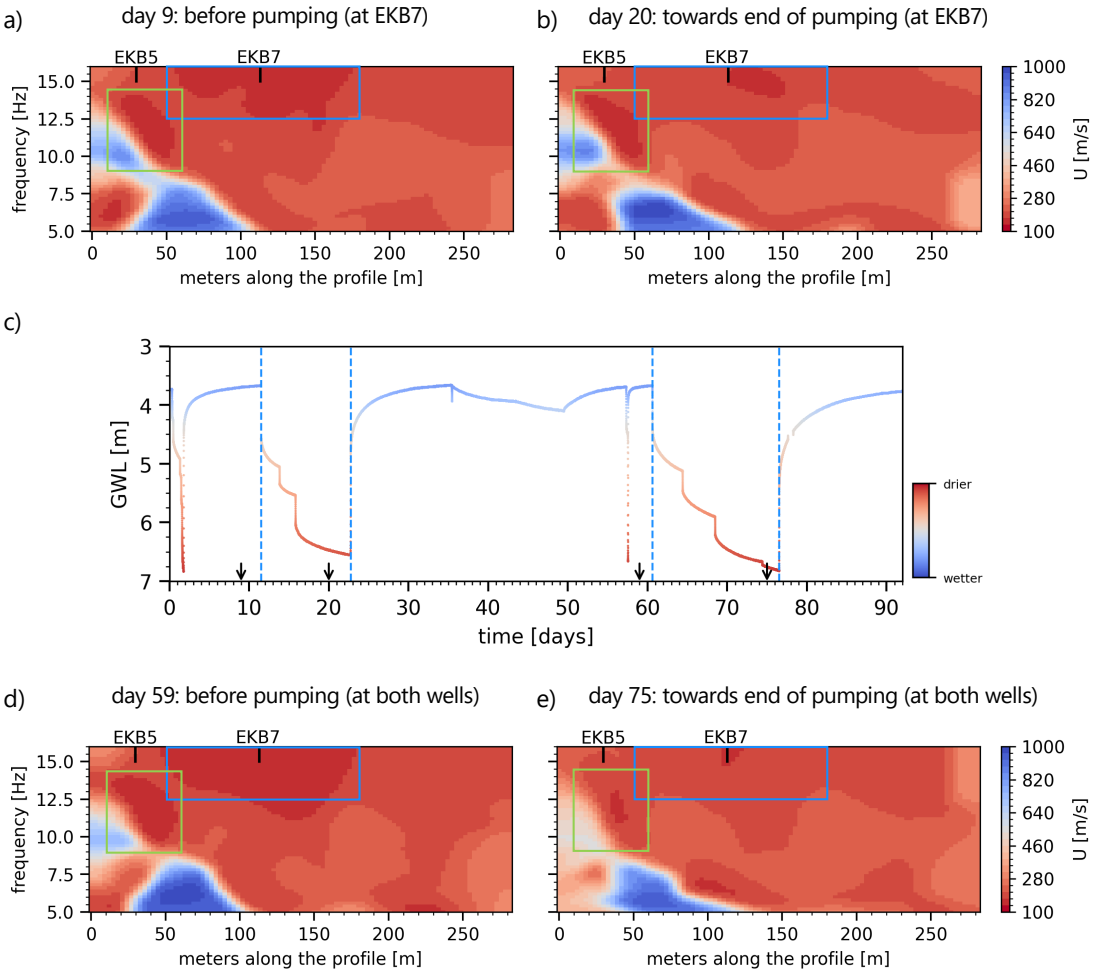


Figure 5.6.: 2-D group velocity profiles after the first step of inversion. Panels **a), b), d),** and **e)** show the obtained group velocities for the days 9, 20, 59, and 75. Panel **c** shows the groundwater level. The blue dashed lines indicate the start and end of the pumping cycles at EKB7.

approach for monitoring hydrological activity, as it shows some clear evidence of changes in subsurface velocities.

5.4.2. Depth Inversion of the Profile

Although the group velocity maps already indicate changes in the subsurface, the changes cannot be directly attributed to a specific depth. Thus, we need to invert the group velocities

for 1-D shear-wave velocity profiles.

At each location along the profile, we extract the Rayleigh-wave group velocity dispersion values. These dispersion measurements are then inverted for a 1-D shear-wave velocity (v_S) profile. The Rayleigh-wave group velocity uncertainty estimated from the ensemble of rjMcMC samples were used as input data uncertainty in the 1-D v_S inversion. For each 1-D inversion, the v_S profile is approximated by 4 layers and the infinite half space. We based this on the stratigraphic log from the boreholes. The parameters for each layer can be found in Tab. T2.

We invert for 1-D v_S profiles to 30 m depth, though our data set has limited sensitivities to approx. 20 m depth. We use *disba* (Luu, 2020) to calculate synthetic Rayleigh-wave group velocity dispersion curves. For each 1-D v_s inversion, we apply the Metropolis-Hastings algorithm (Metropolis et al., 1953; Hastings, 1970), a Markov-chain Monte Carlo (McMC) method, to create an ensemble of samples that approximate the PPD of the model parameters. Specifically, we generate 1 million model samples, with the initial 50,000 discarded for each chain as burn-in samples dependent on the (random) starting velocity model. We calculate the weighted median and (relative) standard deviation of the remaining samples, providing a representative model along with its associated uncertainty. Fig. 5.7 shows an example of results from a 1-D v_S inversion for day 0 of our experiment.

5.4.2.1. General Subsurface Structure

Fig. 5.7c reveals certain features in the shear-wave velocity (v_S) along the profile. In general the velocities vary between 150 m/s up to 500 m/s, which are typical seismic velocities for the near-surface region and the material found in the log (Xia et al., 1999; Schoen, 2015; Sun et al., 2024). Even though the very shallow part (top 1-2 m) shows some higher uncertainties, it indicates some variations alongthe transect which matches the local observations. These relatively higher uncertainties may be attributed to the band-width of our data (Gosselin et al., 2018). The first 70 meters along the transect serve as a storage area for heavy machinery and equipment, whereas the central section (70 m - 200 m) remains unused and overgrown with trees, bushes, and grass. This suggests that the soil at the beginning of the transect may be more compacted, aligning with the higher velocities observed compared to the central part. Another notable feature is a low-velocity zone next to the EKB7 well with velocities around 150 m/s. This could reflect wet soils and clays, which are found in the cores of EKB7. Velocities range between 200 m/s to 325 m/s in the layer below the soil along the transect, potentially reflecting the homogeneous distributions of pebbles and gravels in this depth range, as observed from the log data. Even though there are some low-velocity zones visible below the groundwater level of approx. 4 m, there is neither an interface detected nor a general decrease of seismic velocity. This is in agreement with former studies which are also insensitive to the groundwater table (Pasquet et al., 2015; Sobolevskaia et al., 2024).

Since there are no changes in the geological formations over this short time period, we interpret the main velocity variations between the 93 days to be caused by the pumping experiment and will focus on them in the following sections.

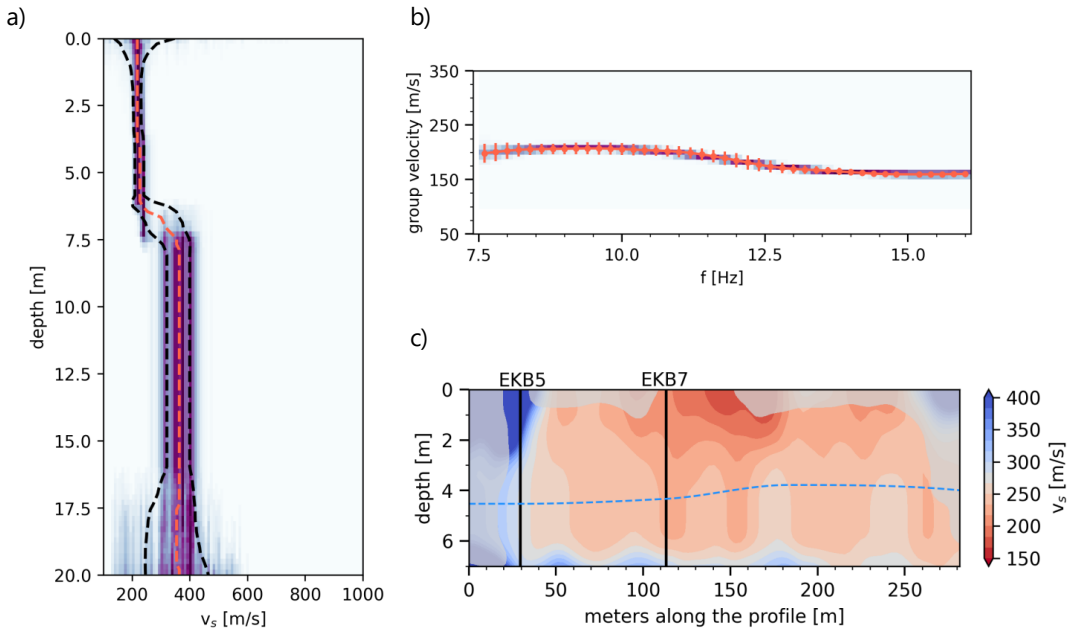


Figure 5.7.: 1-D depth inversion result for grid point 38 (close to the EKB7 well) for day 0. **a)** Posterior probability density for the grid point shown as v_s-depth profile. The red dashed line shows the mean, while the two black dashed lines are the standard deviation. **b)** Shows the local dispersion curve from the group velocity results (red dashed line) and the associated uncertainty. The background shows the fit of this local dispersion curve by the models produced by the McMC algorithm. **c)** Resulting v_S model obtained for day 0 of our experiment. The blue dashed lines indicated the measured groundwater table depth. The grey shaded areas mark parts where the relative standard deviation is higher than 40%.

5.4.2.2. Influence of the Pumping to the Subsurface

To evaluate the influence of pumping activity on v_S, we employ time-lapse tomography. In our approach, we invert for independent v_S models over the course of a 93-day experiment using the same parameterization (see Tab. C.2). For illustration, we concentrate on four representative days, day 9, 20, 59, and 75, which again capture key stages of the pumping cycles (for all 93 days see Supplementary Material Mov. C.8).

Fig. 5.8 presents the v_S inversion results for these selected days alongside concurrent groundwater table measurements. The daily v_S models consistently reveal similar overall structures and velocity distributions that largely mirror each other. However, subtle differences emerge between days, reflecting the dynamic nature of the subsurface in response to pumping.

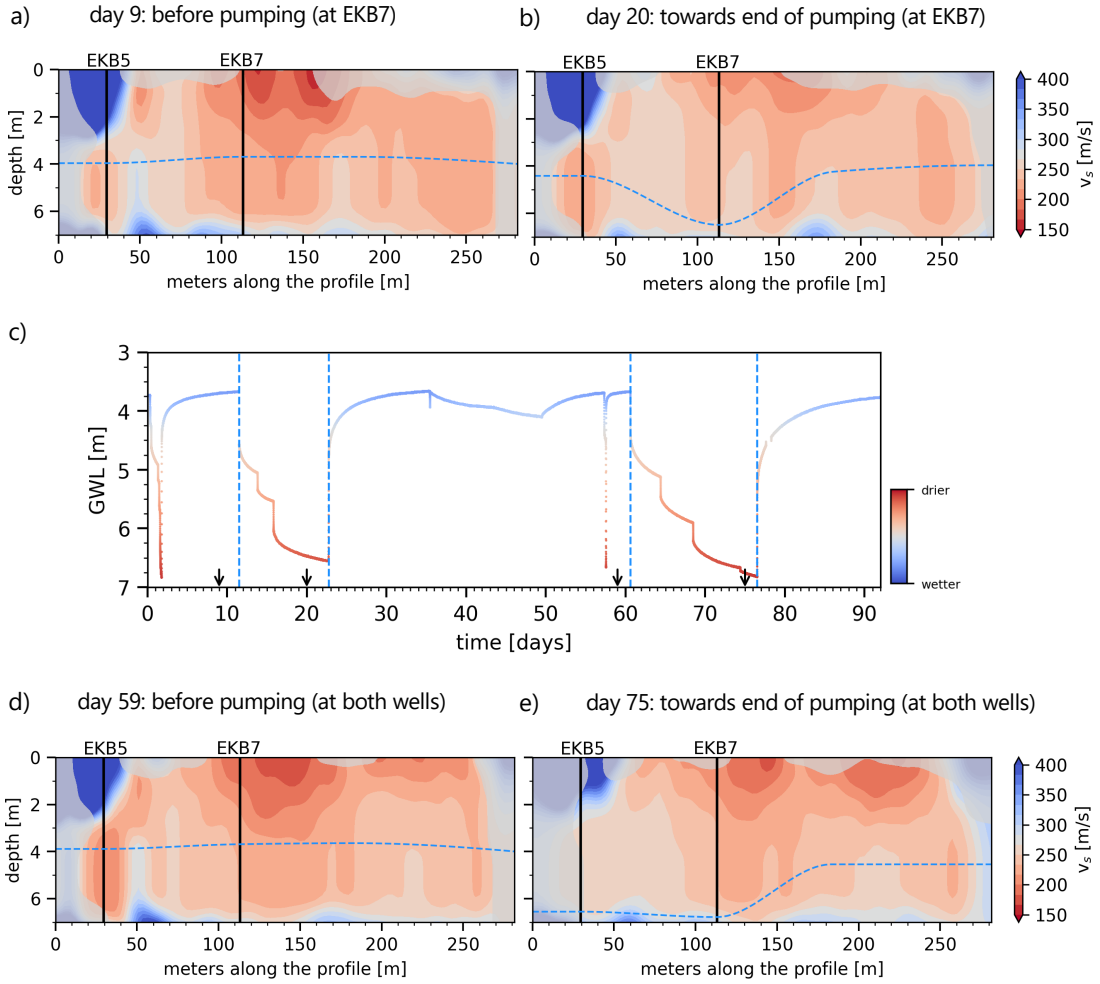


Figure 5.8.: v_s model of the transect obtained from the depth inversion. Panels **a), b), d),** and **e)** show the resulting v_s-models for the days 9, 20, 59 and 75. The blue dashed line indicates the groundwater table measured along the transect. The grey shaded areas mark parts where the relative standard deviation is higher than 40%. **c)** Shows the groundwater level. The blue dashed lines indicate the start and end of the pumping cycles at EKB7.

One of the most notable observations is the general increase in v_S with ongoing pumping activity. During the first pumping cycle (see Fig. 5.8a, b), the velocity changes are primarily localized around the pumping well at EKB7. This localized increase is consistent with the expected compaction and saturation changes in the vicinity of a single pumping source. In

contrast, the second pumping cycle (see Fig. 5.8c, d) involves the simultaneous operation of two wells. This configuration leads to a more complex spatial pattern: increased velocities are observed around each well as well as in the intervening zone. The impact is not confined solely to the saturated zone below the original groundwater table but extends into regions that were originally unsaturated.

The increase in v_S observed below the groundwater table can be explained by well-established petrophysical relationships, where decreased saturation generally leads to higher shear wave velocities (e.g., Schoen, 2015). In the unsaturated zone, the observed velocity changes are more nuanced. These changes can be attributed to coupled unsaturated-saturated flow processes, where the redistribution of water due to pumping alters the moisture content of the soil (Liang et al., 2017). This coupling can have significant implications for the interpretation of drawdown curves obtained from pumping experiments, as the hydraulic response of the unsaturated zone influences the overall system behavior (Mishra and Neuman, 2010, 2011).

Further insights are gained by examining the relative standard deviation of the v_S models (see Fig. C.6). The analysis shows that only limited areas within the model exhibit uncertainties lower than the magnitude of the expected velocity variations induced by saturation changes. This suggests that while the overall trends in v_s are robust, the resolution of our dataset constrains the precision with which we can quantify localized changes.

Despite these limitations, resulting from inhomogeneous ray coverage and inherent frequency restrictions, the time-lapse tomography approach successfully captures the general trend of increasing shear-wave velocity in response to pumping. Moreover, the observed changes not only corroborate laboratory experiments, but also provide valuable insights at the field scale. By mapping the temporal evolution of v_s at various depths (see Fig. 5.9), our study highlights the potential of time-lapse seismic methods as a tool for monitoring hydrological processes.

In summary, the combined inversion results and error analysis demonstrate that our methodology effectively tracks the dynamic response of the subsurface to pumping activity and enables robust interpretation. These findings are significant for hydrologists seeking to understand the interplay between fluid flow and mechanical properties in porous media, and they underscore the potential for further refinement of time-lapse seismic monitoring techniques.

5.5. Limitations and Prospects for Optimization

The presented work illustrates the feasibility of using time-lapse tomography of surface waves as a tool for monitoring pumping tests. Our novel approach provides insights into the dynamic changes of the subsurface, which are crucial for understanding hydrological processes. Despite the promising results, and implementation of an objective inversion procedure, some limitations present targets for future improvement.

The design of the array or profile is a critical factor in the success of the method. To fully

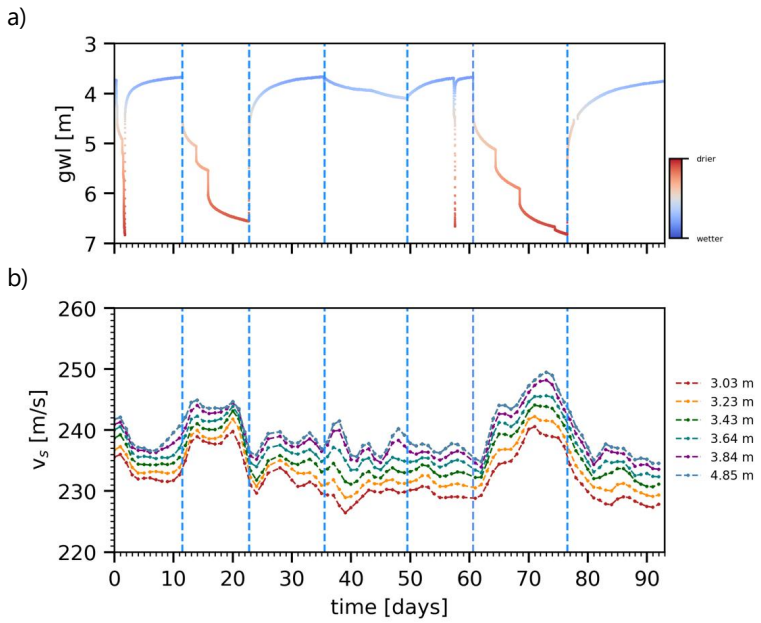


Figure 5.9.: Temporal evolution of v_s during the pumping experiment. **a)** GWLTS but color coded. Blueish colors means higher water saturation in the subsurface, while reddish color indicate the opposite. **b)** v_s extracted for different depth from the final velocity models and averaged between 45 m and 135 m along the transect. The dashed blue lines indicate the start and the end of the pumping of the different phases. Note that, the two gaps are associated with field work and replacement of instruments.

exploit the information contained in higher frequencies and mitigate strong attenuation, shorter station spacing is beneficial. Conversely, extending the profile in both directions can provide more ray paths for lower frequencies, which probe greater depths. This extended design will help better constrain the 2-D group velocity profiles, thereby improving the subsequent 1-D v_S inversions. The careful consideration of array geometry is essential not only for optimizing the frequency content of the data, but also for constraining the inversion results.

The observed changes in v_S appear to correlate with variations in the groundwater table, but we interpret them as changes in saturation due to pumping. However, it is important to note that surface wave sensitivity is inherently spread (integrated) over a broad depth range. This broad sensitivity complicates the direct transformation of group velocity measurements into shear wave velocity profiles by limiting the resolution of discrete layering structure. As such, while the group velocity maps provide valuable information, the depth inversion remains challenging. The broad sensitivity kernels mean that the response from a specific depth is not isolated but rather represents an integrated effect over a range of depths, thereby introducing ambiguity in the inversion process. Without strong constraints on layer interface depths (i.e.,

thicknesses) estimated v_S model uncertainties can be large.

Despite these challenges, the objective inversion strategy used to map group velocities yielded interpretable results. The inversion highlights features expected during a pumping test, such as an increase in velocity due to the removal of water from the pore space in unconsolidated sediments near the pumping well. This observation has important implications for hydrological monitoring, as it suggests that time-lapse tomography can capture the evolution of saturation changes.

The study complements other ambient noise monitoring efforts in hydrology and has several potential applications. With further refinement, it may be possible to quantitatively assess the loss of saturation due to pumping, possibly through the application of Gassmann substitution theory as demonstrated by Voisin et al. (2016). The methodology could also help qualitatively determine the direction of inflow from external water sources, such as rivers, which is critical for understanding regional groundwater recharge. By capturing temporal variations in shear wave velocity, our method provides a field-scale validation of laboratory experiments, bridging the gap between controlled experiments and real-world hydrological processes.

In summary, we highlight the promise of passive time-lapse surface wave tomography as a complementary tool for hydrological monitoring. Additional data types such as phase-velocity dispersion, higher-order modes, or horizontal-to-vertical spectral ratio (HVSR) could further constrain the observed effects, for example in joint inversion approaches. These complementary data would alleviate some of the challenges associated with the fundamental mode Rayleigh wave sensitivity. Addressing the issues of array design and inversion in future studies could further enhance the capability to monitor saturation changes in the near surface, ultimately contributing to more effective water resource management.

5.6. Conclusion and Outlook

In this study, we demonstrated the feasibility of using time-lapse surface wave tomography to monitor pumping tests.

A significant advantage of our study is the strategic deployment of our sensor array perpendicular to a high-traffic railway track, thereby capitalizing on a robust and continuous ambient noise source. Our results indicate that it is possible to retrieve group velocities across a broad frequency range, by capitalizing on such robust noise sources. This demonstrates the potential of using anthropogenic noise to advance ambient noise methodologies. Given that modern environments are infrastructure-dense, our approach is broadly applicable, offering promising prospects for high-quality data acquisition and improved seismic monitoring in urban settings.

Using a data-driven probabilistic inversion framework avoids subjective regularization and allows us to invert for v_s and the associated uncertainties. The inversion results reveal clear temporal trends in shear wave velocity. Notably, we resolve an increase in velocity near

pumping wells, which is attributed to saturation changes in the unconsolidated sediments.

Looking ahead, future work should focus on optimizing array configurations to better balance the resolution of high and low frequencies, thereby enhancing both the spatial and depth resolution of the inversion. Moreover, integrating this approach with quantitative models, such as Gassmann substitution theory, could facilitate the direct quantification of saturation changes in the near-surface environment. This integration would not only improve our understanding of the hydrological impacts of pumping but also provide valuable insights into the directionality of inflow from external water sources, such as rivers.

In summary, this study highlights the potential of passive time-lapse surface wave tomography in hydrological monitoring, and presents avenues for improvements and future research. With targeted improvements in data acquisition, inversion methodology, and model integration, this approach could become a powerful tool for monitoring subsurface hydrological processes and informing water resource management.

Data Availability Statement

The data cannot be made open access due to legal regulations and a disclosure agreement between the Department of Meteorology and Geophysics (University of Vienna) and the Wasserleitungsverband Nördliches Burgenland .

Acknowledgments

We thank the Wasserleitungsverband Nördliches Burgenland for the permission to perform our field experiment. The authors want to thank Yongki Aiman and Daniel Schützenhofer for helping during the fieldwork. Part of this work was supported by the Completion Grant of the Vienna International School of Earth and Space Science.

Publication

The presented study was submitted to the Journal Water Resources Research on May 14, 2025.

manuscript submitted to *Water Resources Research*

Monitoring Groundwater Pumping Using Time-Lapse Tomography from Ambient Seismic Noise

Richard Kramer[1], Clément Estève[1], Yang Lu[2], Jeremy M. Gosselin[3], Birgit Jochum[4], Götz Bokelmann[1]

[1]Department of Meteorology and Geophysics, University of Vienna, Austria
[2]Department of Geosciences and Geography, University of Helsinki, Finland
[3]Natural Resources Canada, Geological Survey of Canada - Pacific, Sidney, Canada
[4]Geosphere Austria, Vienna, Austria

Key Points:

- We showed the feasibility of using time-lapse probabilistic tomography for monitoring a hydrological pumping test.
- We can clearly identify the phases of pumping in the group velocities and the resulting shear wave velocity models.
- Changes in shear waves are coupled to fluctuations in the saturation of unconsolidated sediments in response to water level oscillations.

Corresponding author: Richard Kramer, richard.kramer@univie.ac.at

5.7. Extended Discussion

One of the central questions that has motivated this work is how far seismic methods can replace, or at least augment, classical hydrological monitoring. By going beyond standard coda-wave interferometry and dv/v approaches, we have sought to impose stronger, more accurate constraints on the spatio-temporal evolution of the subsurface response to active pumping.

Our experiments are an important step towards bridging the gap between small-scale laboratory studies of saturation effects and real-world field behavior. Controlled laboratory tests can isolate poroelastic responses to known saturation changes with precision, whereas our field campaign captures the complexity of a natural aquifer under pumping stress. However, the current array design limits both resolution and depth sensitivity. Sampling lower and higher frequencies would require a larger array aperture or denser station spacing, leading to lower uncertainties and better insight into subsurface dynamics.

For this study, we relied on the consistent noise of passing trains as our ambient noise source. Although this approach is convenient in our infrastructure-rich environment, it might not be feasible everywhere. A major goal of subsequent experiments should be to develop an application that can be used anywhere, regardless of the availability of a strong, repeating noise source.

In addition to the Rayleigh wave group velocities used here, several other seismic observables show promise for improving our results. One example is Love waves, which are more sensitive to the shallower parts of the subsurface. Other, more experimental observables could include the H/V spectral ratio (HVSR) or surface wave attenuation. Additionally, the traditional approach of measuring dv/v could provide more detailed information about high temporal variation due to rapid changes induced by pumping.

Our ultimate goal is to transition from relative velocity changes to absolute, quantitative estimates of the following: (1) pore-water saturation via calibrated rock physics models, (2) the spatial geometry of the depletion cone by mapping the three-dimensional velocity perturbation field, and potentially (3) flow directionality. These estimates will transform seismic monitoring into a quantitative tool for water resource management, particularly in remote or infrastructure-poor regions.

6 Summary

Groundwater resources are becoming increasingly vulnerable to overexploitation and climate variability. However, the temporal resolution and spatial coverage of current monitoring techniques are insufficient to detect short-term changes on a large scale. Seismic velocity changes have been identified as a valuable tool for addressing this issue. While long-term variations have received considerable attention, the short-term behaviour of seismic velocities in response to environmental influences has been relatively understudied. This thesis explored the use of ambient noise monitoring for a variety of applications. The aim is to improve our understanding of how environmental factors influence the subsurface and to promote new applications in monitoring the Earth's hydrosphere. The research conducted within the individual projects is based primarily on new observations and constitutes the first attempt to develop models for these phenomena. By combining continuous seismic recordings with hydrological and meteorological data, our work extends existing knowledge.

As mentioned in Chapter 2.1, there is a need in seismology to better understand how environmental factors affect seismic velocity. To this end, we analyzed data from local and regional arrays using coda wave interferometry methods. We adapted the methods to achieve a high temporal resolution to account for the arrays' different sizes. This enabled us to examine daily and sub-daily changes in seismic velocity across various spatial scales. Using established hydrological models, we identified atmospheric pressure variations as the potential driver of these fluctuations in seismic velocity. By systematically mapping the strength of this effect across Central and Southern Europe, we found a correlation between specific vulnerable aquifers and significant sub-daily velocity variations. This demonstrates that periodic velocity changes carry vital information about the subsurface that could be utilized. Insights into periodic velocity variations and their link to vulnerable aquifers pave the way for the practical application of continuous seismic monitoring of the Earth's hydrosphere dynamics.

To expand on these applications, we moved beyond traditional ambient noise monitoring. In our study, we used time-lapse probabilistic seismic tomography to successfully monitor subsurface changes during a groundwater pumping test in Austria. By deploying a dense array of seismic sensors and analyzing ambient noise generated by trains, we could image changes in shear wave velocity at one-day intervals. These variations correlate with water table fluctuations, reflecting changes in saturation. This approach provides continuous spatial data that complements traditional well-based measurements and enhances our understanding of groundwater dynamics.

We demonstrated that ambient seismic monitoring could inform sustainable groundwater management strategies and address urgent issues, such as water scarcity and resource depletion, in the context of climate change and increasing human demand. These methods provide high-resolution, continuous spatial measurements of subsurface properties and could complement existing tools for monitoring illegal pumping and droughts. The results presented in this thesis collectively lay the groundwork for a new generation of hydrosphere monitoring tools that combine environmental sensitivity with operational practicality.

7 Outlook

This thesis identified some potential avenues for future research. While it promoted a broader understanding of the impact of environmental parameters, particularly air pressure, on seismic velocities, some unresolved questions remain that need to be addressed in future research, so that one can make full use of the new observational capabilities demonstrated in this thesis. One of these is achieving a better conceptual understanding in order to model these effects. In particular, we must:

- Quantify (non-linear) responses of seismic velocity to pressure changes and disentangle them from other effects.
- Develop forward models that couple atmospheric, hydrological, and elastic response.

To achieve this, close collaboration with other disciplines, such as hydro(geo)logists, is required. Synergies between geophysicists, hydrologists and even meteorologists could lead to groundbreaking advancements in our understanding, management and protection of one of our most critical resources in the years to come. Joint field campaigns or co-located pilot sites, where multiple sensors run in parallel could lead to important ground-truth observations in controlled settings and experiments. While some of these "outdoor laboratories" are already in place, there is a need for them in different climate zones and geohydrological settings.

Last but not least, the accelerating pace of global warming and its consequences, particularly the disruption to water cycles, should encourage scientists to embrace their instinct for bold experimentation. In these rapidly changing circumstances, developing new tools to help us better understand our environment has never been more urgent. Future work could thus focus on:

- Real-time monitoring networks to provide near-instant feedback on aquifer stress and recharge.
- Machine-learning approaches that can process large datasets in a short amount of time.
- Open, interoperable data platforms that bring together seismic, hydrological and meteorological data, lowering the barrier to interdisciplinary innovation.

By advancing instrumentation, modeling and cross-disciplinary collaboration, the next generation of ambient-noise studies will be well-placed to contribute to the safeguarding of water resources in a warming world.

- No water, no life. No blue, no green. -

Sylvia Earle

References

Aki, K. (1969). Analysis of the seismic coda of local earthquakes as scattered waves. *Journal of Geophysical Research (1896-1977)*, 74(2):615–631.

Aki, K. and Richards, P. G. (2002). *Quantitative Seismology*. University Science Books.

Al-Hashimi, O. A., Hashim, K., Loffill, E., Marolt Cebasek, T., Nakouti, I., Faisal, A., and Al-Ansari, N. (2021). A Comprehensive Review for Groundwater Contamination and Remediation: Occurrence, Migration and Adsorption Modelling. *Molecules*, 26.

Albaric, J., Kühn, D., Ohrnberger, M., Langet, N., Harris, D., Polom, U., Lecomte, I., and Hillers, G. (2021). Seismic monitoring of permafrost in Svalbard, Arctic Norway. *Seismological Society of America*, 92(5):2891–2904.

Allen, R. V. (1978). Automatic earthquake recognition and timing from single traces. *Bulletin of the Seismological Society of America*, 68(5):1521–1532.

Andajani, R. D., Tsuji, T., Snieder, R., and Ikeda, T. (2020). Spatial and temporal influence of rainfall on crustal pore pressure based on seismic velocity monitoring. *Earth, Planets and Space*, 72(1).

Ardhuin, F., Gualtieri, L., and Stutzmann, E. (2015). How ocean waves rock the Earth: Two mechanisms explain microseisms with periods 3 to 300 s. *Geophysical Research Letters*, 42(3):765–772.

Ardhuin, F., Stutzmann, E., Schimmel, M., and Mangeney, A. (2011). Ocean wave sources of seismic noise. *Journal of Geophysical Research: Oceans*, 116(C9).

Aster, R. C., Ringler, A. T., Anthony, R. E., and Lee, T. A. (2023). Increasing ocean wave energy observed in Earth's seismic wavefield since the late 20th century. *Nature Communications*, 14(1):6984.

Aster, R. C. and Winberry, J. P. (2017). Glacial seismology. *Reports on Progress in Physics*, 80(12):126801.

Austrian Water Act (1959). Austrian Water Act 1959 (Wasserrechtsgesetz 1959, WRG). Austrian Federal Law, as amended.

Baisch, S. and Bokelmann, G. H. (1999). Spectral analysis with incomplete time series: an example from seismology. *Computers & Geosciences*, 25(7):739–750.

Barajas, A., Poli, P., D'Agostino, N., Margerin, L., and Campillo, M. (2021). Separation of Poroelastic and Elastic Processes of an Aquifer From Tectonic Phenomena Using Geodetic, Seismic, and Meteorological Data in the Pollino Region, Italy. *Geochemistry, Geophysics, Geosystems*, 22(11):e2021GC009742. e2021GC009742 2021GC009742.

Bauer, P., Thorpe, A., and Brunet, G. (2015). The quiet revolution of numerical weather prediction. *Nature*, 525:47–55.

Bawden, G. W., Thatcher, W., Stein, R. S., Hudnut, K. W., and Peltzer, G. (2001). Tectonic contraction across Los Angeles after removal of groundwater pumping effects. *Nature*, 412(6849):812–815.

Bear, J. (1979). *Hydraulics of Groundwater*. McGraw-Hill series in water resources and environmental engineering. McGraw-Hill International Book Company.

Bell, J. W., Amelung, F., Ferretti, A., Bianchi, M., and Novali, F. (2008). Permanent scatterer InSAR reveals seasonal and long-term aquifer-system response to groundwater pumping and artificial recharge. *Water Resources Research*, 44(2).

Ben-Zion, Y. and Leary, P. (1986). Thermoelastic strain in a half-space covered by unconsolidated material. *Bulletin of the Seismological Society of America*, 76(5):1447–1460.

Bensen, G. D., Ritzwoller, M. H., Barmin, M. P., Levshin, A. L., Lin, F., Moschetti, M. P., Shapiro, N. M., and Yang, Y. (2007). Processing seismic ambient noise data to obtain reliable broad-band surface wave dispersion measurements. *Geophysical Journal International*, 169(3):1239–1260.

Berg, A., Findell, K., Lintner, B., Giannini, A., Seneviratne, S. I., Van Den Hurk, B., Lorenz, R., Pitman, A., Hagemann, S., Meier, A., et al. (2016). Land–atmosphere feedbacks amplify aridity increase over land under global warming. *Nature Climate Change*, 6(9):869–874.

Berg, A. and Sheffield, J. (2018). Climate change and drought: the soil moisture perspective. *Current Climate Change Reports*, 4:180–191.

Berger, J. (1975). A note on thermoelastic strains and tilts. *Journal of Geophysical Research*, 80(2):274–277.

Bevis, M., Businger, S., Herring, T. A., Rocken, C., Anthes, R. A., and Ware, R. H. (1992). GPS meteorology: Remote sensing of atmospheric water vapor using the global positioning system. *Journal of Geophysical Research: Atmospheres*, 97(D14):15787–15801.

Binley, A., Hubbard, S. S., Huisman, J. A., Revil, A., Robinson, D. A., Singha, K., and Slater, L. D. (2015). The emergence of hydrogeophysics for improved understanding of subsurface processes over multiple scales. *Water Resources Research*, 51(6):3837–3866.

Birch, F. (1961). The velocity of compressional waves in rocks to 10 kilobars: 2. *Journal of Geophysical Research (1896-1977)*, 66(7):2199–2224.

Bodin, T., Sambridge, M., Rawlinson, N., and Arroucau, P. (2012). Transdimensional Tomography with Unknown Data Noise. *Geophysical Journal International*, 189:1536–1556.

Bontemps, N., Lacroix, P., Larose, E., Jara, J., and Taipe, E. (2020). Rain and small earthquakes maintain a slow-moving landslide in a persistent critical state. *Nature Communications*, 11(1):780.

Boucher, O., Friedlingstein, P., Collins, B., and Shine, K. P. (2009). The indirect global warming potential and global temperature change potential due to methane oxidation. *Environmental Research Letters*, 4(4):044007.

Bouchon, M., Karabulut, H., Aktar, M., Özalaybey, S., Schmittbuhl, J., and Bouin, M.-P. (2011). Extended nucleation of the 1999 M w 7.6 Izmit earthquake. *science*, 331(6019):877–880.

Bouwer, H. (1977). Land Subsidence and Cracking Due to Ground-Water Depletion. *Groundwater*, 15(5):358–364.

Boué, P., Poli, P., Campillo, M., Pedersen, H., Briand, X., and Roux, P. (2013). Teleseismic correlations of ambient seismic noise for deep global imaging of the Earth. *Geophysical Journal International*, 194(2):844–848.

Brenguier, F., Campillo, M., Hadziioannou, C., Shapiro, N. M., Nadeau, R. M., and Larose, E. (2008a). Postseismic Relaxation Along the San Andreas Fault at Parkfield from Continuous Seismological Observations. *Science*, 321:1478–1481.

Brenguier, F., Campillo, M., Takeda, T., Aoki, Y., Shapiro, N., Briand, X., Emoto, K., and Miyake, H. (2014). Mapping pressurized volcanic fluids from induced crustal seismic velocity drops. *Science*, 345(6192):80–82.

Brenguier, F., Shapiro, N. M., Campillo, M., Ferrazzini, V., Duputel, Z., Coutant, O., and Nercessian, A. (2008b). Towards forecasting volcanic eruptions using seismic noise. *Nature Geoscience*, 1(2):126–130.

Brenguier, F., Shapiro, N. M., Campillo, M., Nercessian, A., and Ferrazzini, V. (2007). 3-D surface wave tomography of the Piton de la Fournaise volcano using seismic noise correlations. *Geophysical Research Letters*, 34(2).

Bromirski, P. D. and Gerstoft, P. (2009). Dominant source regions of the Earth's "hum" are coastal. *Geophysical Research Letters*, 36(13).

Bruland, C., Dichiarante, A. M., Köhler, A., Oye, V., Van Bever, I., and Larose, E. (2025). Cultural activity and impact of extreme weather events revealed by ambient seismic noise and perspective on quick clay failure monitoring in Oslo, Norway. *Engineering Geology*, 347:107936.

Campillo, M. and Paul, A. (2003). Long-Range Correlations in the Diffuse Seismic Coda. *Science*, 299(5606):547–549.

Canassy, P. D., Röösli, C., and Walter, F. (2016). Seasonal variations of glacier seismicity at the tongue of Rhonegletscher (Switzerland) with a focus on basal icequakes. *Journal of Glaciology*, 62(231):18–30.

Capon, J. (1973). Signal Processing and Frequency-Wavenumber Spectrum Analysis for a Large Aperture Seismic Array. In *Methods in Computational Physics: Advances in Research and Applications*, volume 13, pages 1–124. Elsevier.

Castellazzi, P., Martel, R., Galloway, D. L., Longuevergne, L., and Rivera, A. (2016). Assessing groundwater depletion and dynamics using GRACE and InSAR: Potential and limitations. *Groundwater*, 54(6):768–780.

Chapman, S. (1951). *Atmospheric Tides and Oscillations*, pages 510–530. American Meteorological Society.

Chapman, S. and Lindzen, R. S. (1970). *Atmospheric Tides*. Springer Dordrecht.

Chapman, S. and Malin, S. R. C. (1970). Atmospheric Tides, Thermal and Gravitational: Nomenclature, Notation and New Results. *Journal of Atmospheric Sciences*, 27(5):707–710.

Chaussard, E., Bürgmann, R., Shirzaei, M., Fielding, E. J., and Baker, B. (2014). Predictability of hydraulic head changes and characterization of aquifer-system and fault properties from InSAR-derived ground deformation. *Journal of Geophysical Research: Solid Earth*, 119(8):6572–6590.

Chen, B., Gong, H., Chen, Y., Li, X., Zhou, C., Lei, K., Zhu, L., Duan, L., and Zhao, X. (2020). Land subsidence and its relation with groundwater aquifers in Beijing Plain of China. *Science of The Total Environment*, 735:139111.

Chen, Z., Auler, A. S., Bakalowicz, M., Drew, D., Griger, F., Hartmann, J., Jiang, G., Moosdorf, N., Richts, A., Stevanovic, Z., Veni, G., and Goldscheider, N. (2017). The World Karst Aquifer Mapping project: concept, mapping procedure and map of Europe. *Hydrogeology Journal*.

Clarke, D., Zaccarelli, L., Shapiro, N. M., and Brenguier, F. (2011). Assessment of resolution and accuracy of the Moving Window Cross Spectral technique for monitoring crustal temporal variations using ambient seismic noise. *Geophysical Journal International*, 186(2):867–882.

Clements, T. and Denolle, M. A. (2018). Tracking Groundwater Levels Using the Ambient Seismic Field. *Geophysical Research Letters*, 45(13):6459–6465.

Conti, L., Picozza, P., and Sotgiu, A. (2021). A Critical Review of Ground Based Observations of Earthquake Precursors. *Frontiers in Earth Science*, 9.

Cornu, J.-F., Eme, D., and Malard, F. (2013). The distribution of groundwater habitats in Europe. *Hydrogeology Journal*.

Crossley, D. J., Jensen, O. G., and Hinderer, J. (1995). Effective barometric admittance and gravity residuals. *Physics of the Earth and Planetary Interiors*, 90(3–4):221–241.

Custodio, E. (2002). Aquifer overexploitation: what does it mean? *Hydrogeology Journal*, 10(2):254–277.

Dai, A. and Wang, J. (1999). Diurnal and Semidiurnal Tides in Global Surface Pressure Fields. *Journal of the Atmospheric Sciences*, 56(22).

de Ridder, S. A. L., Biondi, B. L., and Clapp, R. G. (2014). Time-lapse seismic noise correlation tomography at Valhall. *Geophysical Research Letters*, 41(17):6116–6122.

Delouche, E. and Stehly, L. (2023). Seasonal Seismic Velocity Variations Measured Using Seismic Noise Autocorrelations to Monitor the Dynamic of Aquifers in Greece. *Journal of Geophysical Research: Solid Earth*, 128(12):e2023JB026759.

Demeritt, D. (2001). The Construction of Global Warming and the Politics of Science. *Annals of the Association of American Geographers*, 91(2):307–337.

Denolle, M. A. and Nissen-Meyer, T. (2020). Quiet Anthropocene, quiet Earth. *Science*, 369(6509):1299–1300.

Derode, A., Larose, E., Tanter, M., de Rosny, J., Tourin, A., Campillo, M., and Fink, M. (2003). Recovering the Green's function from field-field correlations in an open scattering medium (L). *The Journal of the Acoustical Society of America*, 113(6):2973–2976.

Dharmarathne, G., Waduge, A., Bogahawaththa, M., Rathnayake, U., and Meddage, D. (2024). Adapting cities to the surge: A comprehensive review of climate-induced urban flooding. *Results in Engineering*, 22:102123.

Domenico, P. A. and Schwartz, F. W. (1997). *Physical and chemical hydrogeology*. John Wiley & sons.

Dong, Y. and Lu, N. (2016). Dependencies of Shear Wave Velocity and Shear Modulus of Soil on Saturation. *Journal of Engineering Mechanics*, 142.

Dresen, G., Kwiatek, G., Goebel, T., and Ben-Zion, Y. (2020). Seismic and Aseismic Preparatory Processes Before Large Stick–Slip Failure. *Pure and Applied Geophysics*, 177:5741–5760.

du Plessis, A. (2022). Persistent degradation: Global water quality challenges and required actions. *One Earth*, 5(2):129–131.

Dziewonski, A., Bloch, S., and Landisman, M. (1969). A Technique for the Analysis of Transient Seismic Signals. *Bulletin of the Seismological Society of America*, 59(1):427–444.

Ellsworth, W. L. and Beroza, G. C. (1995). Seismic Evidence for an Earthquake Nucleation Phase. *Science*, 268(5212):851–855.

Erler, A. R., Frey, S. K., Khader, O., d'Orgeville, M., Park, Y.-J., Hwang, H.-T., Lapen, D. R., Peltier, W. R., and Sudicky, E. A. (2019). Evaluating Climate Change Impacts on Soil Moisture and Groundwater Resources Within a Lake-Affected Region. *Water Resources Research*, 55(10):8142–8163.

Esteve, C., Lu, Y., Gosselin, J., Kramer, R., Aiman, Y., and Bokelmann, G. (2025). The seismic signature and geothermal potential of the Schwechat Depression in the Vienna Basin, Austria, from ambient noise tomography. *Geothermics*, 127:103211.

Fabbri, A., Wong, H., Lai, B., Bui, T., and Branque, D. (2019). Constitutive elasto-plastic model for fine soils in the unsaturated to saturated saturation zone. *Computers and Geotechnics*, 111:10–21.

Fan, Y., Grant, G., and Anderson, S. P. (2019). Water within, moving through, and shaping the Earth's surface: Introducing a special issue on water in the critical zone. *Hydrological Processes*, 33(25).

Fichtner, A. (2014). Source and Processing Effects on Noise Correlations. *Geophysical Journal International*, 197(3):1527–1531.

Fichtner, A. (2015). Source-Structure Trade-Offs in Ambient Noise Correlations. *Geophysical Journal International*, 202(1):678–694.

Fokker, E., Ruigrok, E., Hawkins, R., and Trampert, J. (2023). 4D Physics-Based Pore Pressure Monitoring Using Passive Image Interferometry. *Geophysical Research Letters*, 50(5).

Food and Agriculture Organization of the United Nations (FAO) (2021). AQUASTAT: FAO's Global Information System on Water and Agriculture.

Ford, D. and Williams, P. (2007). *Introduction to Karst*. John Wiley & Sons, Ltd.

Freeze, R. and Cherry, J. (1979). *Groundwater*. 0-13-365312-9. Prentice-Hall.

Froment, B., Campillo, M., Roux, P., Gouédard, P., Verdel, A., and Weaver, R. L. (2010). Estimation of the effect of nonisotropically distributed energy on the apparent arrival time in correlations. *Geophysics*, 75(5):SA85–SA93.

Fuchs, W., Herrmann, P., and Grill, R. (1985). Geologische Karte der Republik Österreich 1:50.000, Blatt 79 Neusiedl am See – 80 Ungarisch Altenburg – 109 Pamhagen.

Galibert, P.-Y. (2016). Quantitative estimation of water storage and residence time in the epikarst with time-lapse refraction seismic. *Geophysical Prospecting*, 64(2):431–444.

Galloway, D. L. and Burbey, T. J. (2011). Review: Regional land subsidence accompanying groundwater extraction. *Hydrogeology Journal*, 19(8):1459–1486.

Gao, X., Huo, Z., Xu, X., Qu, Z., Huang, G., Tang, P., and Bai, Y. (2018). Shallow groundwater plays an important role in enhancing irrigation water productivity in an arid area: The perspective from a regional agricultural hydrology simulation. *Agricultural water management*, 208:43–58.

Garambois, S., Voisin, C., Romero Guzman, M. A., Brito, D., Guillier, B., and Réfloch, A. (2019). Analysis of ballistic waves in seismic noise monitoring of water table variations in a water field site: added value from numerical modelling to data understanding. *Geophysical Journal International*, 219(3):1636–1647.

Gassenmeier, M., Sens-Schönfelder, C., Delatre, M., and Korn, M. (2014). Monitoring of environmental influences on seismic velocity at the geological storage site for CO2 in Ketzin (Germany) with ambient seismic noise. *Geophysical Journal International*, 200(1):524–533.

Gaubert-Bastide, T., Garambois, S., Bordes, C., Voisin, C., Oxarango, L., Brito, D., and Roux, P. (2022). High-Resolution Monitoring of Controlled Water Table Variations From Dense Seismic-Noise Acquisitions. *Water Resources Research*, 58(8):e2021WR030680. e2021WR030680 2021WR030680.

GeoSphere Austria (2025). Interactive Map - Hydrogeological Map 1:500,000.

Gerstoft, P. and Bromirski, P. (2016). Weather bomb induced seismic signals. *Science*, 353:869–870.

Giazzi, M., Peressutti, G., Cerri, L., Fumi, M., Riva, I., Chini, A., Ferrari, G., Cioni, G., Franch, G., Tartari, G., Galbiati, F., Condemi, V., and Ceppi, A. (2022). Meteonetwork: An Open Crowdsourced Weather Data System. *Atmosphere*, 13:928.

Gleeson, T., Wada, Y., Bierkens, M. F. P., and van Beek, L. P. H. (2012). Water balance of global aquifers revealed by groundwater footprint. *Nature*, 488(7410):197–200.

Gleick, P. (1996). Water Resources, Encyclopaedia of Climate and Weather.

Gonzalez, A., Fontaine, F. R., Barruol, G., Recking, A., Burtin, A., Join, J.-L., Delcher, E., Michon, L., and Gimbert, F. (2023). Seismic signature of a river flooding in La Réunion Island during the tropical cyclone Dumazile (March 2018). *Journal of Applied Geophysics*, 215:105127.

Gosselin, J. M., Audet, P., and Schaeffer, A. J. (2018). Probabilistic seismic-hazard site assessment in Kitimat, British Columbia, from Bayesian inversion of surface-wave dispersion. *Bulletin of the Seismological Society of America*, 108(3A):1351–1362.

Gosselin, J. M., Audet, P., Schaeffer, A. J., Darbyshire, F. A., and Estève, C. (2021). Azimuthal anisotropy in Bayesian surface wave tomography: application to northern Cascadia and Haida Gwaii, British Columbia. *Geophysical Journal International*, 224(3):1724–1741.

Gouédard, P., Roux, P., Campillo, M., Verdel, A., Campman, X., and Weaver, R. L. (2008). Convergence of the two-point correlation function toward the Green's function in the context of a seismic-prospecting data set. *Geophysics*, 73(6):V47–V53.

Gradon, C., Brenguier, F., Stammeijer, J., Mordret, A., Hindriks, K., Campman, X., Lynch, R., Boué, P., and Chmiel, M. (2021). Seismic Velocity Response to Atmospheric Pressure Using Time-Lapse Passive Seismic Interferometry. *Bulletin of the Seismological Society of America*, 111(6):3451–3458.

Green, P. J. (1995). Reversible jump Markov chain Monte Carlo computation and Bayesian model determination. *Biometrika*, 82(4):711–732.

Gruber, S., Hoelzle, M., and Haeberli, W. (2004). Permafrost thaw and destabilization of Alpine rock walls in the hot summer of 2003. *Geophysical Research Letters*, 31(13).

Gualtieri, L., Stutzmann, E., Capdeville, Y., Ardhuin, F., Schimmel, M., Mangeney, A., and Morelli, A. (2013). Modelling secondary microseismic noise by normal mode summation. *Geophysical Journal International*, 193(3):1732–1745.

Guillemot, A., van Herwijnen, A., Larose, E., Mayer, S., and Baillet, L. (2021). Effect of snowfall on changes in relative seismic velocity measured by ambient noise correlation. *The Cryosphere*, 15(12):5805–5817.

Gumuła-Kawęcka, A., Jaworska-Szulc, B., Szymkiewicz, A., Gorczewska-Langner, W., Pruszkowska-Caceres, M., Angulo-Jaramillo, R., and Šimůnek, J. (2022). Estimation of groundwater recharge in a shallow sandy aquifer using unsaturated zone modeling and water table fluctuation method. *Journal of Hydrology*, 605:127283.

Guo, P., Saygin, E., and Kennett, B. (2024). Space-Time Monitoring of Seafloor Velocity Changes Using Seismic Ambient Noise. *Journal of Geophysical Research: Solid Earth*, 129(6):e2023JB027953. e2023JB027953 2023JB027953.

Hadziioannou, C. (2011). *Ondes sismiques en milieu complexe: mesure des variations temporelles des vitesses*. PhD thesis, Universitè Grenoble-Alps.

Hadziioannou, C., Larose, E., Baig, A., Roux, P., and Campillo, M. (2011). Improving temporal resolution in ambient noise monitoring of seismic wave speed. *Journal of Geophysical Research: Solid Earth*, 116(B7).

Hadziioannou, C., Larose, E., Coutant, O., Roux, P., and Campillo, M. (2009). Stability of monitoring weak changes in multiply scattering media with ambient noise correlation: Laboratory experiments. *The Journal of the Acoustical Society of America*, 125(6):3688–3695.

Haeni, F. P. (1986). Application of Continuous Seismic Reflection Methods to Hydrologic Studies. *Groundwater*, 24(1):23–31.

Hanssen, R. (2001). *Radar Interferometry Data Interpretation and Error Analysis*, volume 2. Springer.

Harjes, H.-P. (1990). Design and siting of a new regional array in Central Europe. *Bulletin of the Seismological Society of America*, 80(6B):1801–1817.

Hasselmann, K. (1963). A statistical analysis of the generation of microseisms. *Reviews of Geophysics*, 1(2):177–210.

Hastings, W. K. (1970). Monte Carlo sampling methods using Markov chains and their applications. *Biometrika*, 57(1):97–109.

Heinz, B., Birk, S., Liedl, R., Geyer, T., Straub, K. L., Bester, K., and Kappler, A. (2006). Vulnerability of a karst spring to wastewater infiltration (Gallusquelle, Southwest Germany). *Austrian Journal of Earth Sciences*, 99:11–17.

Hennino, R., Trégourès, N., Shapiro, N. M., Margerin, L., Campillo, M., van Tiggelen, B. A., and Weaver, R. L. (2001). Observation of Equipartition of Seismic Waves. *Phys. Rev. Lett.*, 86:3447–3450.

Herrmann, R. B. (1973). Some Aspects of Band-Pass Filtering of Surface Waves. *Bulletin of the Seismological Society of America*, 63(2):663–671.

Herrmann, R. B. (1987). *Computer Programs in Seismology*. University.

Herrmann, R. B. (2013). Computer Programs in Seismology: An Evolving Tool for Instruction and Research. *Seismological Research Letters*, 84(6):1081–1088.

Hetényi, G., Molinari, I., Clinton, J., and et al. (2018). The AlpArray Seismic Network: A Large-Scale European Experiment to Image the Alpine Orogen. *Surveys in Geophysics*, 39:1009–1033.

Hetzel, F., Vaessen, V., Himmelsbach, T., Struckmeier, W., and Villholt, K. G. (2008). Groundwater and climate change: Challenges and possibilities. *Groundwater. Resources and Management*.

Hillers, G., Ben-Zion, Y., Campillo, M., and Zigone, D. (2015a). Seasonal variations of seismic velocities in the San Jacinto fault area observed with ambient seismic noise. *Geophysical Journal International*, 202(2):920–932.

Hillers, G., Husen, S., Obermann, A., Planès, T., Larose, E., and Campillo, M. (2015b). Noise-based monitoring and imaging of aseismic transient deformation induced by the 2006 Basel reservoir stimulation. *GEOPHYSICS*, 80(4):KS51–KS68.

Hillers, G., Retailleau, L., Campillo, M., Inbal, A., Ampuero, J. P., and Nishimura, T. (2015c). In situ observations of velocity changes in response to tidal deformation from analysis of the high-frequency ambient wavefield. *Journal of Geophysical Research: Solid Earth*, 120(1):210–225.

Hjort, J., Streletskiy, D., Doré, G., Wu, Q., Bjella, K., and Luoto, M. (2022). Impacts of permafrost degradation on infrastructure. *Nature Reviews Earth & Environment*, 3(1):24–38.

Hussein, M. E. A., Odling, N. E., and Clark, R. A. (2013). Borehole water level response to barometric pressure as an indicator of aquifer vulnerability. *Water Resources Research*, 49(10):7102–7119.

Ikeda, T. and Tsuji, T. (2018). Temporal change in seismic velocity associated with an offshore MW 5.9 Off-Mie earthquake in the Nankai subduction zone from ambient noise cross-correlation. *Progress in Earth and Planetary Science*, 5:62.

Illien, L., Andermann, C., Sens-Schönfelder, C., Cook, K. L., Baidya, K. P., Adhikari, L. B., and Hovius, N. (2021). Subsurface Moisture Regulates Himalayan Groundwater Storage and Discharge. *AGU Advances*, 2(2):e2021AV000398.

Illien, L., Sens-Schönfelder, C., Andermann, C., Marc, O., Cook, K. L., Adhikari, L. B., and Hovius, N. (2022). Seismic Velocity Recovery in the Subsurface: Transient Damage and Groundwater Drainage Following the 2015 Gorkha Earthquake, Nepal. *Journal of Geophysical Research: Solid Earth*, 127(2):e2021JB023402.

IPCC (2021). *Climate Change 2021: The Physical Science Basis. Contribution of Working Group I to the Sixth Assessment Report of the Intergovernmental Panel on Climate Change*, volume In Press. Cambridge University Press, Cambridge, United Kingdom and New York, NY, USA.

James, S., Knox, H., Abbott, R., Panning, M., and Screaton, E. (2019). Insights into permafrost and seasonal active-layer dynamics from ambient seismic noise monitoring. *Journal of Geophysical Research: Earth Surface*, 124(7):1798–1816.

Jang, W.-S., Engel, B., Harbor, J., and Theller, L. (2017). Aquifer Vulnerability Assessment for Sustainable Groundwater Management Using DRASTIC. *Water*, 9(10).

Ji, K. H. and Herring, T. A. (2012). Correlation between changes in groundwater levels and surface deformation from GPS measurements in the San Gabriel Valley, California. *Geophysical Research Letters*, 39(1).

Ji, Y., Gao, H., Wang, K., and Song, X. (2021). Observation of Higher-Mode Surface Waves from an Active Source in the Hutubi Basin, Xinjiang, China. *Journal of Geophysical Research: Solid Earth*, 126(9).

Jones, N. F., Pejchar, L., and Kiesecker, J. M. (2015). The Energy Footprint: How Oil, Natural Gas, and Wind Energy Affect Land for Biodiversity and the Flow of Ecosystem Services. *BioScience*, 65(3):290–301.

Karagianni, A., Karoutzos, G., Ktena, S., Vagenas, N., Vlachopoulos, I., Sabatakakis, N., and Koukis, G. (2010). Elastic Properties of Rocks. *Bulletin of the Geological Society of Greece*, 43(3):1165–1168.

Khaldoun, A., Moller, P., Fall, A., Wegdam, G., De Leeuw, B., Méheust, Y., Otto Fossum, J., and Bonn, D. (2009). Quick clay and landslides of clayey soils. *Physical review letters*, 103(18):188301.

Kim, D. and Lekic, V. (2019). Groundwater Variations From Autocorrelation and Receiver Functions. *Geophysical Research Letters*, 46(23):13722–13729.

King, N. E., Argus, D., Langbein, J., Agnew, D. C., Bawden, G., Dollar, R. S., Liu, Z., Galloway, D., Reichard, E., Yong, A., Webb, F. H., Bock, Y., Stark, K., and Barseghian, D. (2007). Space geodetic observation of expansion of the San Gabriel Valley, California,

aquifer system, during heavy rainfall in winter 2004–2005. *Journal of Geophysical Research: Solid Earth*, 112(B3).

Knoblauch, C., Beer, C., Liebner, S., Grigoriev, M. N., and Pfeiffer, E.-M. (2018). Methane production as key to the greenhouse gas budget of thawing permafrost. *Nature Climate Change*, 8(4):309–312.

Kramer, R., Lu, Y., and Bokelmann, G. (2023). Interaction of air pressure and groundwater as main cause of sub-daily relative seismic velocity changes. *Geophysical Research Letters*, 50.

Kramer, R., Lu, Y., Wang, Q.-Y., Serafin, S., Ceppi, A., and Bokelmann, G. (2025). Identifying large vulnerable water reservoirs using passive seismic monitoring. *Earth and Planetary Science Letters*, 653:119223.

Kruseman, G. P., De Ridder, N. A., and Verweij, J. M. (1970). *Analysis and evaluation of pumping test data*, volume 11. International institute for land reclamation and improvement Wageningen, The ....

Köhler, A., Nuth, C., Schweitzer, J., Weidle, C., and Gibbons, S. J. (2015). Regional passive seismic monitoring reveals dynamic glacier activity on Spitsbergen, Svalbard. *Polar Research*, 34:26178.

Lanari, R., Lundgren, P., Manzo, M., and Casu, F. (2004). Satellite radar interferometry time series analysis of surface deformation for Los Angeles, California. *Geophysical Research Letters*, 31(23).

Larose, E., Carrière, S., Voisin, C., Bottelin, P., Baillet, L., Guéguen, P., Walter, F., Jongmans, D., Guillier, B., Garambois, S., Gimbert, F., and Massey, C. (2015). Environmental seismology: What can we learn on earth surface processes with ambient noise? *Journal of Applied Geophysics*, 116:62–74.

Larose, E., Planès, T., Rossetto, V., and Margerin, L. (2010). Locating a small change in a multiple scattering environment. *Applied Physics Letters*, 96(20).

Larson, K. M., Small, E. E., Gutmann, E. D., Bilich, A. L., Braun, J. J., and Zavorotny, V. U. (2008). Use of GPS receivers as a soil moisture network for water cycle studies. *Geophysical Research Letters*, 35(24).

Lashof, D. A. and Ahuja, D. R. (1990). Relative contributions of greenhouse gas emissions to global warming. *Nature*, 344(6266):529–531.

Le Breton, M., Bontemps, N., Guillemot, A., Baillet, L., and Larose, É. (2021). Landslide monitoring using seismic ambient noise correlation: challenges and applications. *Earth-Science Reviews*, 216:103518.

Lecocq, T., Caudron, C., and Brenguier, F. (2014). MSNoise, a Python package for monitoring seismic velocity changes using ambient seismic noise. *Seismological Research Letter*, 85(3):715–726.

Lecocq, T., Hicks, S. P., Noten, K. V., van Wijk, K., Koelemeijer, P., Plaen, R. S. M. D., Massin, F., Hillers, G., Anthony, R. E., Apoloner, M.-T., Arroyo-Solórzano, M., Assink, J. D., Büyükakpınar, P., Cannata, A., Cannavo, F., Carrasco, S., Caudron, C., Chaves, E. J., Cornwell, D. G., Craig, D., den Ouden, O. F. C., Diaz, J., Donner, S., Evangelidis, C. P., Evers, L., Fauville, B., Fernandez, G. A., Giannopoulos, D., Gibbons, S. J., Girona, T., Grecu, B., Grunberg, M., Hetényi, G., Horleston, A., Inza, A., Irving, J. C. E., Jamalreyhani, M., Kafka, A., Koymans, M. R., Labedz, C. R., Larose, E., Lindsey, N. J., McKinnon, M., Megies, T., Miller, M. S., Minarik, W., Moresi, L., Márquez-Ramírez, V. H., Möllhoff, M., Nesbitt, I. M., Niyogi, S., Ojeda, J., Oth, A., Proud, S., Pulli, J., Retailleau, L., Rintamäki, A. E., Satriano, C., Savage, M. K., Shani-Kadmiel, S., Sleeman, R., Sokos, E., Stammler, K., Stott, A. E., Subedi, S., Sørensen, M. B., Taira, T., Tapia, M., Turhan, F., van der Pluijm, B., Vanstone, M., Vergne, J., Vuorinen, T. A. T., Warren, T., Wassermann, J., and Xiao, H. (2020). Global quieting of high-frequency seismic noise due to COVID-19 pandemic lockdown measures. *Science*, 369(6509):1338–1343.

Levshin, A. L., Yanovskaya, T. B., Lander, A. V., Bukchin, B. G., Barmin, M. P., Ratnikova, L. I., and Its, E. N. (1989). *Seismic Surface Waves in a Laterally Inhomogeneous Earth*, volume 9 of *Modern Approaches in Geophysics*. Springer Netherlands, Dordrecht.

Liang, X. S., Zhang, L., and Li, J. (2017). On the coupled unsaturated–saturated flow process induced by vertical, horizontal, and slant wells in unconfined aquifers. *Water Resources Research*, 53(1):188–210.

Lin, F.-C. and Ritzwoller, M. H. (2011). Helmholtz Surface Wave Tomography for Isotropic and Azimuthally Anisotropic Structure. *Geophysical Journal International*, 186(3):1104–1120.

Lindner, F., Wassermann, J., and Igel, H. (2021). Seasonal freeze-thaw cycles and permafrost degradation on Mt. Zugspitze (German/Austrian Alps) revealed by single-station seismic monitoring. *Geophysical Research Letters*, 48(18):e2021GL094659.

Liu, X. and Fan, Y. (2012). On the characteristics of high-frequency Rayleigh waves in stratified half-space. *Geophysical Journal International*, 190(2):1041–1057.

Liu, Z., Liang, C., Zhu, Z., Wang, L., Jiang, N., Wang, C., and Wu, Z. (2019). The Complex Velocity Variation Induced by the Precipitation and the 2018 Eruption of the Kilauea Volcano in Hawaii Revealed by Ambient Noise. *Seismological Research Letters*, 90(6):2154–2164.

Lobkis, O. I. and Weaver, R. L. (2001). On the emergence of the Green's function in the correlations of a diffuse field. *The Journal of the Acoustical Society of America*, 110(6):3011–3017.

Lobkis, O. I. and Weaver, R. L. (2003). Coda-Wave Interferometry in Finite Solids: Recovery of P-to-S Conversion Rates in an Elastodynamic Billiard. *Phys. Rev. Lett.*, 90:254302.

Longuet-Higgins, M. S. and Jeffreys, H. (1950). A theory of the origin of microseisms. *Philosophical Transactions of the Royal Society of London. Series A, Mathematical and Physical Sciences*, 243(857):1–35.

Lu, Y., Stehly, L., Brossier, R., Paul, A., and Group, A. W. (2020). Imaging Alpine Crust Using Ambient Noise Wave-Equation Tomography. *Geophysical Journal International*, 222(1):69–85.

Lu, Y., Stehly, L., Paul, A., and the AlpArray Working Group (2018). High-resolution surface wave tomography of the European crust and uppermost mantle from ambient seismic noise. *Geophysical Journal International*, 214(2):1136–1150.

Luu, K. (2020). disba: Numba-accelerated computation of surface wave dispersion. GitHub repository. `https://github.com/kevinluu/disba`.

Mainsant, G., Larose, E., Brönnimann, C., Jongmans, D., Michoud, C., and Jaboyedoff, M. (2012). Ambient seismic noise monitoring of a clay landslide: Toward failure prediction. *Journal of Geophysical Research: Earth Surface*, 117(F1).

Mantovani, E., Viti, M., Babbucci, D., Tamburelli, C., and Cenni, N. (2019). How and why the present tectonic setting in the Apennine belt has developed. *Journal of the Geological Society*, 176.

Mao, S., Campillo, M., van der Hilst, R., Brenguier, F., Stehly, L., and Hillers, G. (2019a). High temporal resolution monitoring of small variations in crustal strain by dense seismic arrays. *Geophysical Research Letters*, 46:128–137.

Mao, S., Lecointre, A., van der Hilst, R. D., and Campillo, M. (2022). Space-time monitoring of groundwater fluctuations with passive seismic interferometry. *Nature Communications*, 13.

Mao, S., Mordret, A., Campillo, M., Fang, H., and van der Hilst, R. D. (2019b). On the measurement of seismic traveltime changes in the time–frequency domain with wavelet cross-spectrum analysis. *Geophysical Journal International*, 221(1):550–568.

Margerin, L., Planès, T., Mayor, J., Calvet, M., Rossetto, V., and Campillo, M. (2015). Sensitivity kernels for coda-wave interferometry and scattering tomography: theory and numerical evaluation in two-dimensional anisotropically scattering media. *Geophysical Journal International*, 202(1):512–523.

Mavko, G., Mukerji, T., and Dvorkin, J. (2009). *The Rock Physics Handbook: Tools for Seismic Analysis of Porous Media*. Cambridge University Press, 2 edition.

Mayor, J., Margerin, L., Calvet, M., and Rossetto, V. (2014). Sensitivity of coda waves to spatial variations of absorption and scattering: radiative transfer theory and 2-D examples. *Geophysical Journal International*, 196(1):680–697.

McMillan, T. C., Rau, G. C., Timms, W. A., and Andersen, M. S. (2019). Utilizing the Impact of Earth and Atmospheric Tides on Groundwater Systems: A Review Reveals the Future Potential. *Reviews of Geophysics*, 57(2):281–315.

Megdal, S. B. (2018). Invisible water: the importance of good groundwater governance and management. *npj Clean Water*.

Meier, U., Shapiro, N. M., and Brenguier, F. (2010). Detecting seasonal variations in seismic velocities within Los Angeles basin from correlations of ambient seismic noise. *Geophysical Journal International*, 181(2):985–996.

Metropolis, N., Rosenbluth, A. W., Rosenbluth, M. N., Teller, A. H., and Teller, E. (1953). Equation of State Calculations by Fast Computing Machines. *The Journal of Chemical Physics*, 21(6):1087–1092.

Mikesell, T. D., Malcolm, A. E., Yang, D., and Haney, M. M. (2015). A comparison of methods to estimate seismic phase delays: numerical examples for coda wave interferometry. *Geophysical Journal International*, 202(1):347–360.

Mishra, P. K. and Neuman, S. P. (2010). Improved forward and inverse analyses of saturated-unsaturated flow toward a well in a compressible unconfined aquifer. *Water Resources Research*, 46(7).

Mishra, P. K. and Neuman, S. P. (2011). Saturated-unsaturated flow to a well with storage in a compressible unconfined aquifer. *Water Resources Research*, 47(5).

Montagner, J.-P., Mangeney, A., and Stutzmann, E. (2020). Seismology and Environment. *Encyclopedia of Solid Earth Geophysics*, pages 1–8.

Mordret, A., Mikesell, T. D., Harig, C., Lipovsky, B. P., and Prieto, G. A. (2016). Monitoring southwest Greenland's ice sheet melt with ambient seismic noise. *Science Advances*, 2(5).

Morton, T. J. and Crotwell, H. P. (2015). A modified F-K filter for removing the effects of higher-mode dispersion patterns from surface wave data. *Seismological Research Letters*, 86(2A):427–434.

Mukherjee, S., Mishra, A., and Trenberth, K. (2018). Climate Change and Drought: a Perspective on Drought Indices. *Current Climate Change Reports*, 4.

Nakata, N., Gualtieri, L., and Fichtner, A. (2019). *Seismic Ambient Noise*. Cambridge University Press,, Cambridge, England.

Nakata, N. and Snieder, R. (2011). Near-surface weakening in Japan after the 2011 Tohoku-Oki earthquake. *Geophysical Research Letters*, 38(17).

Nakata, N. and Snieder, R. (2012). Estimating near-surface shear wave velocities in Japan by applying seismic interferometry to KiK-net data. *Journal of Geophysical Research: Solid Earth*, 117(B1).

Nishida, K., Montagner, J.-P., and Kawakatsu, H. (2009). Global Surface Wave Tomography Using Seismic Hum. *Science*, 326(5949):112–112.

Nistor, M.-M. (2020). Groundwater vulnerability in Europe under climate change. *Quaternary International*, 547:185–196.

Niu, F., Silver, P. G., Daley, T. M., Cheng, X., and Majer, E. L. (2008). Preseismic velocity changes observed from active source monitoring at the Parkfield SAFOD drill site. *Nature*, 454(7201):204–208.

Norum, D. I. and Luthin, J. N. (1968). The effects of entrapped air and barometric fluctuations on the drainage of porous mediums. *Water Resources Research*, 4(2):417–424.

Nouibat, A., Brossier, R., Stehly, L., Cao, J., Paul, A., and Cifalps Team and AlpArray Working Group (2023). Ambient-Noise Wave-Equation Tomography of the Alps and Ligurian-Provence Basin. *Journal of Geophysical Research: Solid Earth*, 128(10):e2023JB026776. e2023JB026776 2023JB026776.

Nur, A. (1971). Effects of stress on velocity anisotropy in rocks with cracks. *Journal of Geophysical Research (1896-1977)*, 76(8):2022–2034.

Nur, A. and Simmons, G. (1969). Stress-induced velocity anisotropy in rock: An experimental study. *Journal of Geophysical Research (1896-1977)*, 74(27):6667–6674.

Oakley, D., Forsythe, B., Gu, X., Nyblade, A., and Brantley, S. (2021). Seismic Ambient Noise Analyses Reveal Changing Temperature and Water Signals to 10s of Meters Depth in the Critical Zone. *Journal of Geophysical Research: Earth Surface*, 126(2).

Obermann, A., Froment, B., Campillo, M., Larose, E., Planès, T., Valette, B., Chen, J. H., and Liu, Q. Y. (2014). Seismic noise correlations to image structural and mechanical changes associated with the Mw 7.9 2008 Wenchuan earthquake. *Journal of Geophysical Research: Solid Earth*, 119(4):3155–3168.

Obermann, A. and Hillers, G. (2019). Chapter Two - Seismic time-lapse interferometry across scales. In Schmelzbach, C., editor, *Recent Advances in Seismology*, volume 60 of *Advances in Geophysics*, pages 65–143. Elsevier.

Obermann, A., Planès, T., Larose, E., and Campillo, M. (2013a). Imaging preeruptive and coeruptive structural and mechanical changes of a volcano with ambient seismic noise. *Journal of Geophysical Research: Solid Earth*, 118(12):6285–6294.

Obermann, A., Planès, T., Larose, E., Sens-Schönfelder, C., and Campillo, M. (2013b). Depth sensitivity of seismic coda waves to velocity perturbations in an elastic heterogeneous medium. *Geophysical Journal International*, 194(1):372–382.

O'Connell, R. J. and Budiansky, B. (1974). Seismic velocities in dry and saturated cracked solids. *Journal of Geophysical Research (1896-1977)*, 79(35):5412–5426.

Odling, N., R., P., Hussein, M., Riva, M., and Guadagnini, A. (2015). Detecting the vulnerability of groundwater in semi-confined aquifers using barometric response functions. *Journal of Hydrology*, 520:143–156.

Okamoto, T., Larsen, J. O., Matsuura, S., Asano, S., Takeuchi, Y., and Grande, L. (2004). Displacement properties of landslide masses at the initiation of failure in quick clay deposits and the effects of meteorological and hydrological factors. *Engineering geology*, 72(3-4):233–251.

Olivier, G., Brenguier, F., Carey, R., Okubo, P., and Donaldson, C. (2019). Decrease in Seismic Velocity Observed Prior to the 2018 Eruption of Kīlauea Volcano With Ambient Seismic Noise Interferometry. *Geophysical Research Letters*, 46(7):3734–3744.

Pacheco, C. and Snieder, R. (2005). Time-lapse travel time change of multiply scattered acoustic waves. *The Journal of the Acoustical Society of America*, 118(3):1300–1310.

Palumbo, A. (1998). Atmospheric tides. *Journal of Atmospheric and Solar-Terrestrial Physics*, 60(3):279–287.

Pascher, G., Herrmann, P., Mandl, G., Matura, A., Nowotny, A., Pahr, A., and Schnabel, W. (1999). Geologische Karte des Burgenlandes 1:200.000. In Schönlaub, H., editor, *Geologie der Österreichischen Bundesländer – Burgenland; Erläuterungen zur Geologischen Karte des Burgenlandes 1:200.000*. Geologische Bundesanstalt, Wien.

Pasquet, S., Bodet, L., Dhemaied, A., Rejiba, F., Abraham, O., Al-Halbouni, D., Samyn, K., Versteeg, R., Guérin, R., and Camerlynck, C. (2015). Detecting different water table levels in a shallow aquifer with combined P-, surface and SH-wave surveys: Insights from VP/VS or Poisson's ratios. *Journal of Applied Geophysics*, 113:38–50.

Pathirana, S., Lambot, S., Krishnapillai, M., Cheema, M., Smeaton, C., and Galagedara, L. (2023). Ground-Penetrating Radar and Electromagnetic Induction: Challenges and Opportunities in Agriculture. *Remote Sensing*, 15(11).

Paul, A., Campillo, M., Margerin, L., Larose, E., and Derode, A. (2005). Empirical synthesis of time-asymmetrical Green functions from the correlation of coda waves. *The Journal of Geophysical Research: Solid Earth*, 110(B8).

Peck, A. J. (1960). The water table as affected by atmospheric pressure. *Journal of Geophysical Research (1896-1977)*, 65(8):2383–2388.

Peterson, J. R. (1993). Observations and modeling of seismic background noise. *U.S. Geological Survey Technical Report*.

Petit, J. R., Jouzel, J., Raynaud, D., Barkov, N. I., Barnola, J.-M., Basile, I., Bender, M., Chappellaz, J., Davis, M., Delaygue, G., Delmotte, M., Kotlyakov, V. M., Legrand, M., Lipenkov, V. Y., Lorius, C., PÉpin, L., Ritz, C., Saltzman, E., and Stievenard, M. (1999). Climate and atmospheric history of the past 420,000 years from the Vostok ice core, Antarctica. *Nature*, 399(6735):429–436.

Podolskiy, E. A. and Walter, F. (2016). Cryoseismology. *Reviews of Geophysics*, 54(4):708–758.

Pollitz, F. F. (1992). Postseismic relaxation theory on the spherical earth. *Bulletin of the Seismological Society of America*, 82(1):422–453.

Pollitz, F. F. (2005). Transient rheology of the upper mantle beneath central Alaska inferred from the crustal velocity field following the 2002 Denali earthquake. *Journal of Geophysical Research: Solid Earth*, 110(B8).

Poupinet, G., Ellsworth, W. L., and Frechet, J. (1984). Monitoring velocity variations in the crust using earthquake doublets: An application to the Calaveras fault, California. *Journal of Geophysical Research: Solid Earth*, 112(B7):5719–5731.

Qin, L., Qiu, H., Nakata, N., Deng, S., Levander, A., and Ben-Zion, Y. (2022). Variable Daily Autocorrelation Functions of High-Frequency Seismic Data on Mars. *Seismological Research Letters*, 94(2A):746–758.

Qureshi, A. S., Gill, M. A., and Sarwar, A. (2010). Sustainable groundwater management in Pakistan: challenges and opportunities. *Irrigation and Drainage: The Journal of the International Commission on Irrigation and Drainage*, 59(2):107–116.

Rabbel, W. and Zschau, J. (1985). Deformations and Gravity Changes at the Earth's Surface Due to Atmospheric Loading. *Journal of Geophysics*, 56:81–89.

Rasmussen, T. C. and Crawford, L. A. (1997). Identifying and Removing Barometric Pressure Effects in Confined and Unconfined Aquifers. *Groundwater*, 35(3):502–511.

Ratdomopurbo, A. and Poupinet, G. (1995). Monitoring a temporal change of seismic velocity in a volcano: Application to the 1992 eruption of Mt. Merapi (Indonesia). *Geophysical Research Letters*, 22(7):775–778.

Reasenberg, P. and Aki, K. (1974). A precise, continuous measurement of seismic velocity for monitoring in situ stress. *Journal of Geophysical Research (1896-1977)*, 79(2):399–406.

Rebert, T., Bardainne, T., Allemand, T., Cai, C., and Chauris, H. (2024). Characterization of train kinematics and source wavelets from near-field seismic data. *Geophysical Journal International*, 237(2):697–715.

Retailleau, L. and Gualtieri, L. (2019). Toward High-Resolution Period-Dependent Seismic Monitoring of Tropical Cyclones. *Geophysical Research Letters*, 46(3):1329–1337.

Retailleau, L. and Gualtieri, L. (2021). Multi-phase seismic source imprint of tropical cyclones. *Nature Communications*, 12:2064.

Rezaei, A. and Mousavi, Z. (2019). Characterization of land deformation, hydraulic head, and aquifer properties of the Gorgan confined aquifer, Iran, from InSAR observations. *Journal of Hydrology*, 579:124196.

Rhie, J. and Romanowicz, B. (2004). Excitation of Earth's continuous free oscillations by atmosphere–ocean–seafloor coupling. *Nature*, 431.

Richey, A. S., Thomas, B. F., Lo, M.-H., Reager, J. T., Famiglietti, J. S., Voss, K., Swenson, S., and Rodell, M. (2015). Quantifying renewable groundwater stress with GRACE. *Water Resources Research*, 51(7):5217–5238.

Richter, T., Sens-Schönfelder, C., Kind, R., and Asch, G. (2014). Comprehensive observation and modeling of earthquake and temperature-related seismic velocity changes in northern Chile with passive image interferometry. *Journal of Geophysical Research: Solid Earth*, 119(6):4747–4765.

Rivet, D., Campillo, M., Sanchez-Sesma, F., Shapiro, N. M., and Singh, S. K. (2015). Identification of surface wave higher modes using a methodology based on seismic noise and coda waves. *Geophysical Journal International*, 203(2):856–868.

Robinson, D., Binley, A., Crook, N., Day-Lewis, F., Ferré, T., Grauch, V., Knight, R., Knoll, M., Lakshmi, V., Miller, R., et al. (2008). Advancing process-based watershed hydrological research using near-surface geophysics: A vision for, and review of, electrical and magnetic geophysical methods. *Hydrological Processes: An International Journal*, 22(18):3604–3635.

Rodell, M. and Famiglietti, J. S. (2002). The potential for satellite-based monitoring of groundwater storage changes using GRACE: the High Plains aquifer, Central US. *Journal of Hydrology*, 263(1-4):245–256.

Rodríguez Tribaldos, V. and Ajo-Franklin, J. B. (2021). Aquifer Monitoring Using Ambient Seismic Noise Recorded With Distributed Acoustic Sensing (DAS) Deployed on Dark Fiber. *Journal of Geophysical Research: Solid Earth*, 126(4).

Roeloffs, E. (1988). Hydrologic precursors to earthquakes: A review. *Pure and Applied Geophysics*, 126:177–209.

Roeloffs, E. (1996). Poroelastic Techniques in the Study of Earthquake-Related Hydrologic Phenomena. *Advances in Geophysics*, 37:135–195.

Romero-Ruiz, A., Linde, N., Keller, T., and Or, D. (2018). A Review of Geophysical Methods for Soil Structure Characterization. *Reviews of Geophysics*, 56(4):672–697.

Rosen, P., Hensley, S., Zebker, H., Webb, F., and Fielding, E. (1996). Surface deformation and coherence measurements of Kilauea Volcano, Hawaii, from SIR-C radar interferometry. *Journal of Geophysical Research*, 101:23109–23125.

Roux, P. (2009). Passive seismic imaging with directive ambient noise: application to surface waves and the San Andreas Fault in Parkfield, CA. *Geophysical Journal International*, 179(1):367–373.

Roux, P., Sabra, K. G., Gerstoft, P., Kuperman, W. A., and Fehler, M. C. (2005). P-waves from cross-correlation of seismic noise. *Geophysical Research Letters*, 32(19).

Rubin, Y. and Hubbard, S. S. (2006). *Hydrogeophysics*, volume 50. Springer Science & Business Media.

Sager, K., Boehm, C., Ermert, L., Krischer, L., and Fichtner, A. (2020). Global-Scale Full-Waveform Ambient Noise Inversion. *Journal of Geophysical Research: Solid Earth*, 125(4):e2019JB018644. e2019JB018644 10.1029/2019JB018644.

Saji, A. P., Sunil, P. S., Sreejith, K. M., Gautam, P. K., Kumar, K. V., Ponraj, M., Amirtharaj, S., Shaju, R. M., Begum, S. K., Reddy, C. D., and Ramesh, D. S. (2020). Surface Deformation and Influence of Hydrological Mass Over Himalaya and North India Revealed From a Decade of Continuous GPS and GRACE Observations. *Journal of Geophysical Research: Earth Surface*, 125(1):e2018JF004943. e2018JF004943 2018JF004943.

Schnabel, W., Krenmayr, H.-G., Mandl, G., Nowotny, A., Roetzel, R., and Scharbert, S., editors (2002). *Legende und kurze Erläuterungen zur geologischen Karte von Niederösterreich 1:200.000*. Geologische Bundesanstalt Wien.

Schoen, J. (2015). *Physical Properties of Rocks - Fundamentals and Principles of Petrophysics*. Elsevier.

Schoenberg, M. (1980). Elastic wave behavior across linear slip interfaces. *The Journal of the Acoustical Society of America*, 68(5):1516–1521.

Scuderi, M., Marone, C., and Tinti E.and Di Stefano, G.and Collettini, C. (2016). Precursory changes in seismic velocity for the spectrum of earthquake failure modes. *Nature Geoscience*, 9(9):695–700.

Sens-Schönfelder, C. and Eulenfeld, T. (2019). Probing the in situ Elastic Nonlinearity of Rocks with Earth Tides and Seismic Noise. *Physical Review Letters*, 122.

Sens-Schönfelder, C. and Wegler, U. (2006). Passive image interferometry and seasonal variations of seismic velocities at Merapi Volcano, Indonesia. *Geophysical Research Letters*, 33(21):109–119.

Serpelloni, E., Pintori, F., Gualandi, A., Scoccimarro, E., Cavaliere, A., Anderlini, L., Belardinelli, M. E., and Todesco, M. (2018). Hydrologically Induced Karst Deformation: Insights From GPS Measurements in the Adria-Eurasia Plate Boundary Zone. *Journal of Geophysical Research: Solid Earth*, 123(5):4413–4430.

Shapiro, N. and Singh, S. (1999). A systematic error in estimating surface-wave group-velocity dispersion curves and a procedure for its correction. *Bulletin of the Seismological Society of America*, 89(4):1138–1142.

Shapiro, N. M. and Campillo, M. (2004). Emergence of broadband Rayleigh waves from correlations of the ambient seismic noise. *Geophysical Research Letters*, 31(7).

Shapiro, N. M., Campillo, M., Stehly, L., and Ritzwoller, M. H. (2005). High-Resolution Surface-Wave Tomography from Ambient Seismic Noise. *Science*, 307(5715):1615–1618.

Shen, Z., Yang, Y., Fu, X., Adams, K. H., Biondi, E., and Zhan, Z. (2024). Fiber-optic seismic sensing of vadose zone soil moisture dynamics. *Nature Communications*, 15(1):6432.

Shi, X., Mao, D., Song, K., Xiang, H., Li, S., and Wang, Z. (2024). Effects of landscape changes on water quality: A global meta-analysis. *Water Research*, 260:121946.

Short Gianotti, D. J., Akbar, R., Feldman, A. F., Salvucci, G. D., and Entekhabi, D. (2020). Terrestrial Evaporation and Moisture Drainage in a Warmer Climate. *Geophysical Research Letters*, 47(5):e2019GL086498.

Silver, P. G., Daley, T. M., Niu, F., and Majer, E. L. (2007). Active Source Monitoring of Cross-Well Seismic Travel Time for Stress-Induced Changes. *Bulletin of the Seismological Society of America*, 97(1B):281–293.

Singh, A., Panda, S. N., Uzokwe, V. N. E., and Krause, P. (2019). An assessment of groundwater recharge estimation techniques for sustainable resource management. *Groundwater for Sustainable Development*, 9:100218.

Smith, A., Lott, N., and Vose, R. (2011). The Integrated Surface Database: Recent Developments and Partnerships. *Bulletin of the American Meteorological Society*, 92.

Snieder, R. (2006). The theory of Coda Wave Interferometry. *Pure and Applied Geophysics*, 163:455–473.

Snieder, R., Grêt, A., Douma, H., and Scales, J. (2002). Coda Wave Interferometry for Estimating Nonlinear Behavior in Seismic Velocity. *Science*, 295(5563):2253–2255.

Snieder, R. and Trampert, J. (1999). *Inverse Problems in Geophysics*. Springer.

Sobolevskaia, V., Ajo-Franklin, J., Cheng, F., Dou, S., Lindsey, N. J., and Wagner, A. (2024). Monitoring Water Level of a Surficial Aquifer Using Distributed Acoustic Sensing and Ballistic Surface Waves. *Water Resources Research*, 60(8):e2023WR036172. e2023WR036172 2023WR036172.

Solazzi, S. G., Bodet, L., Holliger, K., and Jougnot, D. (2021). Surface-Wave Dispersion in Partially Saturated Soils: The Role of Capillary Forces. *Journal of Geophysical Research: Solid Earth*, 126(12).

Somers, L. D. and McKenzie, J. M. (2020). A review of groundwater in high mountain environments. *WIREs Water*, 7(6).

Sophocleous, M. (2003). Environmental implications of intensive groundwater use with special regard to streams and wetlands. *Intensive use of groundwater: challenges and opportunities*, pages 93–112.

Stehly, L., Fry, B., Campillo, M., Shapiro, N. M., Guilbert, J., Boschi, L., and Giardini, D. (2009). Tomography of the Alpine region from observations of seismic ambient noise. *Geophysical Journal International*, 178(1):338–350.

Stevanovic, Z. (2015). *Karst Aquifers: Characterization and Engineering*. Springer.

Stevanovic, Z. (2019). Karst waters in potable water supply: a global scale overview. *Environmental Earth Sciences*.

Stork, A. L., Allmark, C., Curtis, A., Kendall, J.-M., and White, D. J. (2018). Assessing the potential to use repeated ambient noise seismic tomography to detect CO2 leaks: Application to the Aquistore storage site. *International Journal of Greenhouse Gas Control*, 71:20–35.

Subcommittee Permafrost (1988). Glossary of permafrost and related ground-ice terms. *Associate Committee on Geotechnical Research, National Research Council of Canada, Ottawa*, 156:63–64.

Sun, Z., Li, M., Yamanaka, H., Lu, Y., Song, X., Wu, H., Zhang, H., and Chen, S. (2024). Three-Dimensional Urban Subsurface Space Tomography with Dense Ambient Noise Seismic Array. *Seismological Research Letters*, 95(1):85–96.

Syed, T. H., Famiglietti, J. S., and Chambers, D. P. (2009). GRACE-based estimates of terrestrial freshwater discharge from basin to continental scales. *Journal of Hydrometeorology*, 10(1):22–40.

Takano, T., Nishimura, T., Nakahara, H., Ohta, Y., and Tanaka, S. (2014). Seismic velocity changes caused by the Earth tide: Ambient noise correlation analyses of small-array data. *Geophysical Research Letters*, 41(17):6131–6136.

Taylor, C. J. and Alley, W. M. (2001). Ground-water-level monitoring and the importance of long-term water-level data. *U.S. Geological Survey Circular*.

Taylor, R., Scanlon, B., Döll, P., Rodell, M., Van Beek, R., Wada, Y., Longuevergne, L., Leblanc, M., Famiglietti, J., Edmunds, M., Konikow, L., Green, T., Chen, J., Taniguchi, M., Bierkens, M., Macdonald, A., Fan, Y., Maxwell, R., Yechieli, Y., Gurdak, J., Allen, D., Shamsudduha, M., Hiscock, K., Yeh, P., Holman, I., and Treidel, H. (2013). Ground water and climate change. *Nature Climate Change*, 3(4):322–329.

Theis, C. V. (1935). The relation between the lowering of the Piezometric surface and the rate and duration of discharge of a well using ground-water storage. *Eos, Transactions American Geophysical Union*, 16(2):519–524.

Tiwari, V. M., Wahr, J., and Swenson, S. (2009). Dwindling groundwater resources in northern India, from satellite gravity observations. *Geophysical Research Letters*, 36(18).

Todd, D. K. and Mays, L. W. (2004). *Groundwater hydrology*. John Wiley & Sons.

Tokimatsu, K., Tamura, S., and Kojima, H. (1992). Effects of multiple modes on Rayleigh wave dispersion characteristics. *Journal of geotechnical engineering*, 118(10):1529–1543.

Toksöz, M. N., Cheng, C. H., and Timur, A. (1976). Velocities of seismic waves in porous rocks. *Geophysics*, 41(4):621–645.

Toksöz, M. N. and Lacoss, R. T. (1968). Microseisms: Mode Structure and Sources. *Science*, 159(3817):872–873.

Topp, G. C., Davis, J., and Annan, A. P. (1980). Electromagnetic determination of soil water content: Measurements in coaxial transmission lines. *Water resources research*, 16(3):574–582.

Tsai, V. C. (2011). A model for seasonal changes in GPS positions and seismic wave speeds due to thermoelastic and hydrologic variations. *Journal of Geophysical Research: Solid Earth*, 116(B4).

Tsai, V. C., Sager, K., and Bowden, D. C. (2024). Towards limited-domain full waveform ambient noise inversion. *Geophysical Journal International*, 237(2):965–973.

Turk, L. (1975). Diurnal fluctuations of water tables induced by atmospheric pressure changes. *Journal of Hydrology*, 26(1):1–16.

Uchiyama, Y. and McWilliams, J. C. (2008). Infragravity waves in the deep ocean: Generation, propagation, and seismic hum excitation. *Journal of Geophysical Research: Oceans*, 113(C7).

United Nations (2025). Gobal Issues: Population.

Valois, R., Rau, G. C., Vouillamoz, J.-M., and Derode, B. (2022). Estimating Hydraulic Properties of the Shallow Subsurface Using the Groundwater Response to Earth and Atmospheric Tides: A Comparison With Pumping Tests. *Water Resources Research*, 58(5):e2021WR031666.

Van Camp, M., de Viron, O., Watlet, A., Meurers, B., Francis, O., and Caudron, C. (2017). Geophysics From Terrestrial Time-Variable Gravity Measurements. *Reviews of Geophysics*, 55(4):938–992.

Vereecken, H., Binley, A., Cassiani, G., Revil, A., and Titov, K. (2006). Applied Hydrogeophysics, vol. 71 of IV: Earth and Environmental sciences. *NATO Science Series*.

Voisin, C., Garambois, S., Massey, C., and Brossier, R. (2016). Seismic noise monitoring of the water table in a deep-seated, slow-moving landslide. *Interpretation*, 4(3):SJ67–SJ76.

Voisin, C., Romero Guzmán, M., Réfloch, A., Taruselli, M., and Garambois, S. (2017). Groundwater Monitoring with Passive Seismic Interferometry. *Journal of Water Resource and Protection*, 9:1414–1427.

Wada, Y., van Beek, L. P. H., van Kempen, C. M., Reckman, J. W. T. M., Vasak, S., and Bierkens, M. F. P. (2010). Global depletion of groundwater resources. *Geophysical Research Letters*, 37(20).

Wang, G., Liang, X., Li, J., Wang, J., and Wang, C.-Y. (2024a). Impact of Depth-Dependent Heterogeneity in Aquifers on the Response of Unsaturated-Saturated Flow to Earth Tides. *Water Resources Research*, 60(6):e2023WR036310. e2023WR036310 2023WR036310.

Wang, P., Yu, J., Pozdniakov, S. P., Grinevsky, S. O., and Liu, C. (2014). Shallow groundwater dynamics and its driving forces in extremely arid areas: a case study of the lower Heihe River in northwestern China. *Hydrological Processes*, 28(3):1539–1553.

Wang, Q.-Y., Brenguier, F., Campillo, M., Lecointre, A., Takeda, T., and Aoki, Y. (2017). Seasonal Crustal Seismic Velocity Changes Throughout Japan. *Journal of Geophysical Research: Solid Earth*, 122(10):7987–8002.

Wang, Q.-Y., Campillo, M., Brenguier, F., Lecointre, A., Takeda, T., and Hashima, A. (2019). Evidence of Changes of Seismic Properties in the Entire Crust Beneath Japan After the Mw 9.0, 2011 Tohoku-oki Earthquake. *Journal of Geophysical Research: Solid Earth*, 124(8):8924–8941.

Wang, Q.-Y., Cui, X., Frank, W. B., Lu, Y., Hirose, T., and Obara, K. (2024b). Untangling the environmental and tectonic drivers of the Noto earthquake swarm in Japan. *Science Advances*, 10(19):eado1469.

Wang, Q.-Y. and Yao, H. J. (2020). Monitoring of velocity changes based on seismic ambient noise: A brief review and perspective. *Earth and Planetary Physics*, 4(5):532–542.

Wapenaar, K. (2004). Retrieving the Elastodynamic Green's Function of an Arbitrary Inhomogeneous Medium by Cross Correlation. *Phys. Rev. Lett.*, 93:254301.

Watson, K. M., Bock, Y., and Sandwell, D. T. (2002). Satellite interferometric observations of displacements associated with seasonal groundwater in the Los Angeles basin. *Journal of Geophysical Research: Solid Earth*, 107(B4):ETG 8–1–ETG 8–15.

Weaver, R. and Lobkis, O. (2002). On the emergence of the Green's function in the correlations of a diffuse field: pulse-echo using thermal phonons. *Ultrasonics*, 40(1):435–439.

Weaver, R. L. and Lobkis, O. I. (2004). Diffuse fields in open systems and the emergence of the Green's function (L). *The Journal of the Acoustical Society of America*, 116(5):2731–2734.

Webb, S. C. (2008). The Earth's hum: the excitation of Earth normal modes by ocean waves. *Geophysical Journal International*, 174(2):542–566.

Weichert, D., Horner, R. B., and Evans, S. G. (1994). Seismic signatures of landslides: The 1990 Brenda Mine collapse and the 1965 Hope rockslides. *Bulletin of the Seismological Society of America*, 84(5):1523–1532.

Wendland, F., Blum, A., Coetsiers, M., Gorova, R., Griffioen, J., Grima-Olmedo, J., Hinsby, K., Kunkel, R., Marandi, A., de Melo, M. T., Panagopoulos, A., Pauwels, H., Ruisi, M., Traversa, P., Vermooten, S., and Walraevens, K. (2008). European aquifer typology: A practical framework for an overview of major groundwater composition at European scale. *Environmental Geology*, 55:77–85.

White, A. M., Gardner, W. P., Borsa, A. A., Argus, D. F., and Martens, H. R. (2022). A Review of GNSS/GPS in Hydrogeodesy: Hydrologic Loading Applications and Their Implications for Water Resource Research. *Water Resources Research*, 58(7):e2022WR032078. e2022WR032078 2022WR032078.

Wielandt, E. (2012). Seismic Sensors and their Calibration. *New manual of seismological observatory practice 2*, pages 1–51.

World Meteorological Organization (WMO) (1954). Reduction of Atmospheric Pressure: Preliminary Report on Problems Involved. Technical Note No. 7 (WMO-No. 36,TP. 12). Technical report, WMO.

Wu, W.-Y., Lo, M.-H., Wada, Y., Famiglietti, J. S., Reager, J. T., Yeh, P. J.-F., Ducharne, A., and Yang, Z.-L. (2020). Divergent effects of climate change on future groundwater availability in key mid-latitude aquifers. *Nature Communications*, 11(1):3710.

Xanke, J., Goldscheider, N., Bakalowicz, M., Barberá, J. A., Broda, S., Chen, Z., Ghanmi, M., Günther, A., Hartmann, A., Jourde, H., Liesch, T., Mudarra, M., Petitta, M., Ravbar, N., and Stevanovic, Z. (2022). Mediterranean Karst Aquifer Map (MEDKAM), 1:5,000,000. *Berlin, Karlsruhe, Paris*.

Xia, J., Miller, R. D., and Park, C. B. (1999). Estimation of near-surface shear-wave velocity by inversion of Rayleigh waves. *Geophysics*, 64(3):691–700.

Yamamura, K., Sano, O., Utada, H., Takei, Y., Nakao, S., and Fukao, Y. (2003). Long-term observation of in situ seismic velocity and attenuation. *Journal of Geophysical Research: Solid Earth*, 108(B6).

Yates, A. S., Caudron, C., Mordret, A., Lesage, P., Pinel, V., Lecocq, T., Miller, C. A., Lamb, O. D., and Fournier, N. (2024). Seasonal Snow Cycles and Their Possible Influence on Seismic Velocity Changes and Eruptive Activity at Ruapehu Volcano, New Zealand. *Journal of Geophysical Research: Solid Earth*, 129(12):e2024JB029568.

Young, Z. M., Martens, H. R., Hoylman, Z. H., and Gardner, W. P. (2024). Drought Characterization With GPS: Insights Into Groundwater and Surface-Reservoir Storage in California. *Water Resources Research*, 60(8):e2024WR037404. e2024WR037404 2024WR037404.

Zhan, Z., Tsai, V. C., and Clayton, R. W. (2013). Spurious velocity changes caused by temporal variations in ambient noise frequency content. *Geophysical Journal International*, 194(3):1574–1581.

ÖNORM ISO 22282-4:2021 (2012). Geotechnical investigation and testing - Geohydraulic testing - Part 4: Pumping tests (ISO 22282-4:2021). Austrian National Standard.

A Appendix: Interaction of Air Pressure and Groundwater as Main Cause of Sub-Daily Relative Seismic Velocity Changes

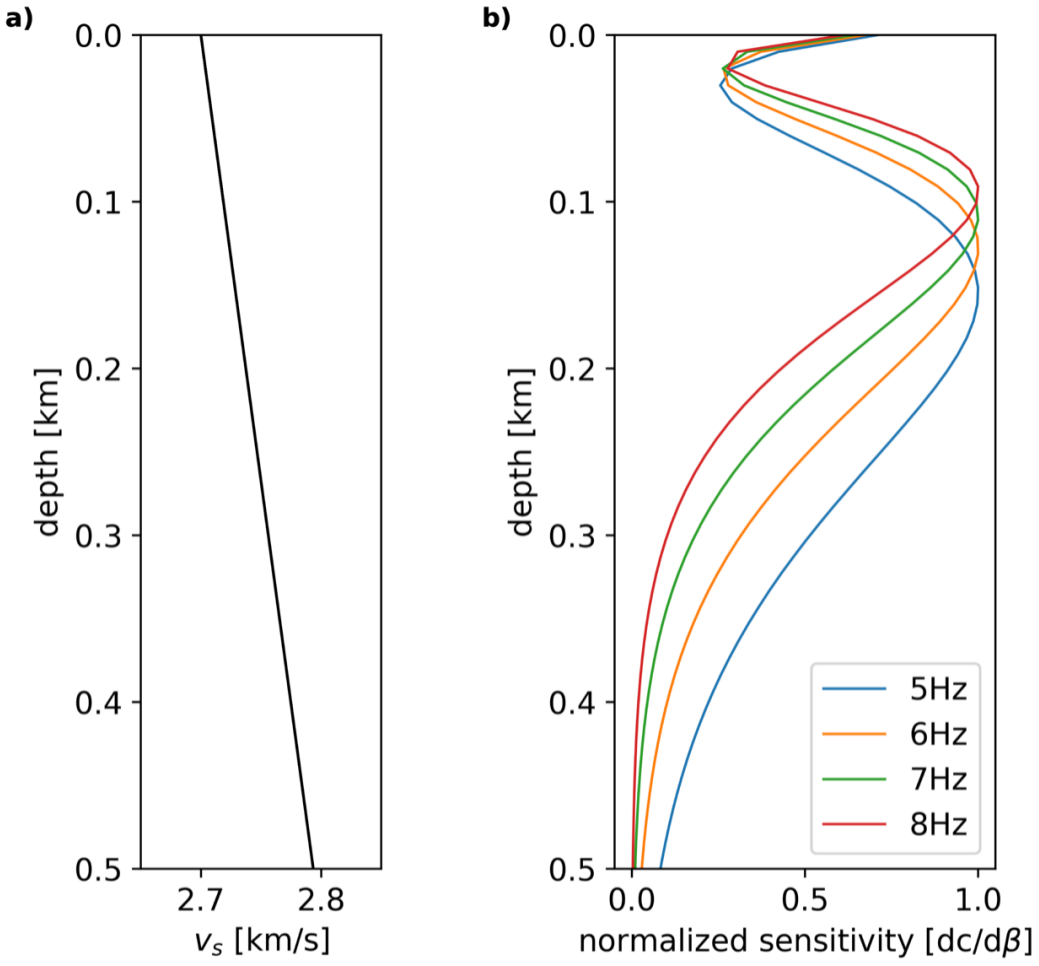


Figure A.1.: **a)** Estimated shear-wave velocity profile for the investigated region. **b)** Sensitivity kernels calculated with the software of Herrmann (2013). The shown frequency is the center frequency of the different frequency bands.

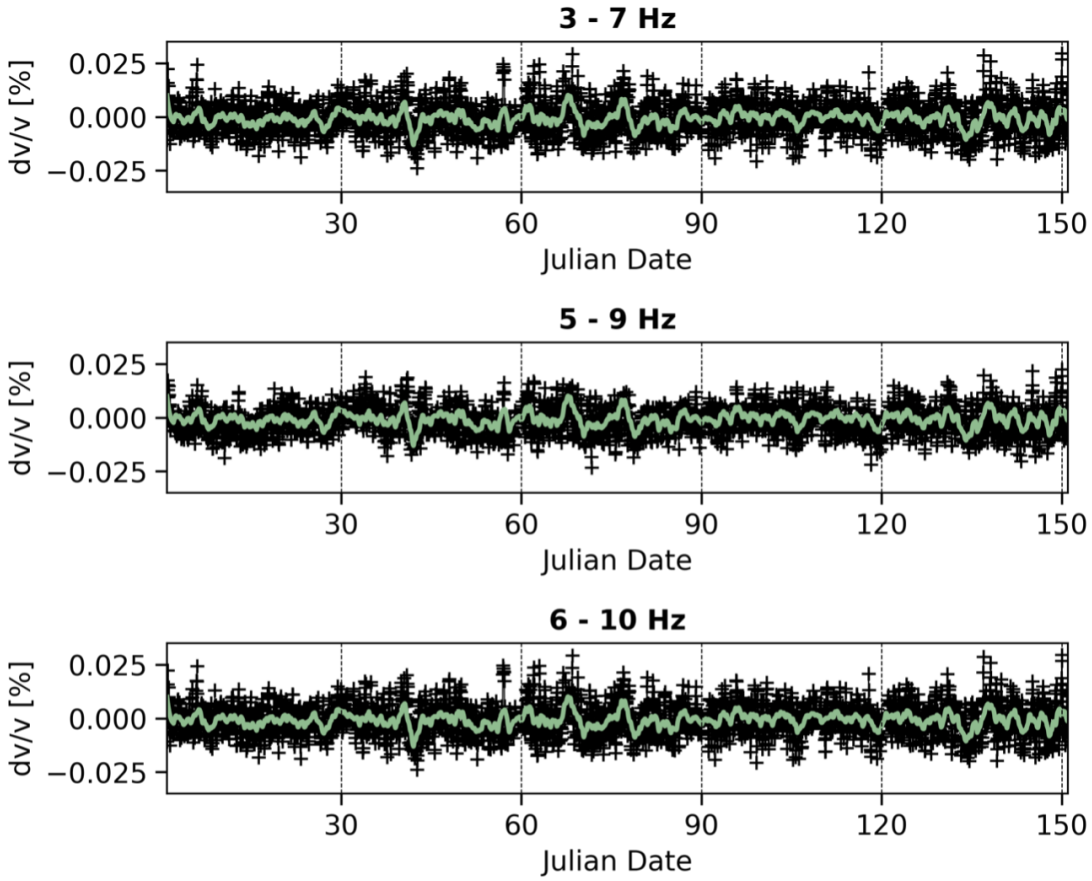


Figure A.2.: Relative seismic velocity changes for different frequency bands. The green curve shows a smoothed version of the hourly measurements (black line with crosses).

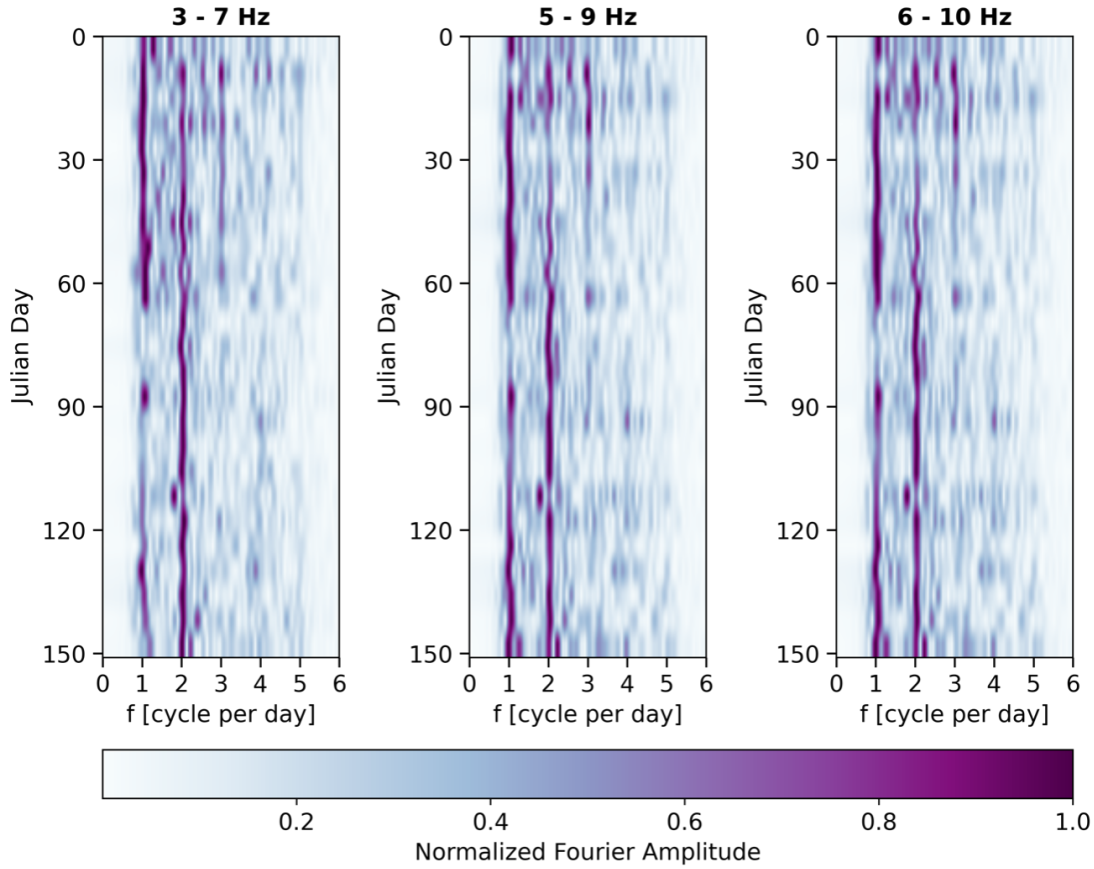


Figure A.3.: 2D spectrograms calculated within a 7-day sliding window Fourier analysis. The three different panels show the different frequency bands.

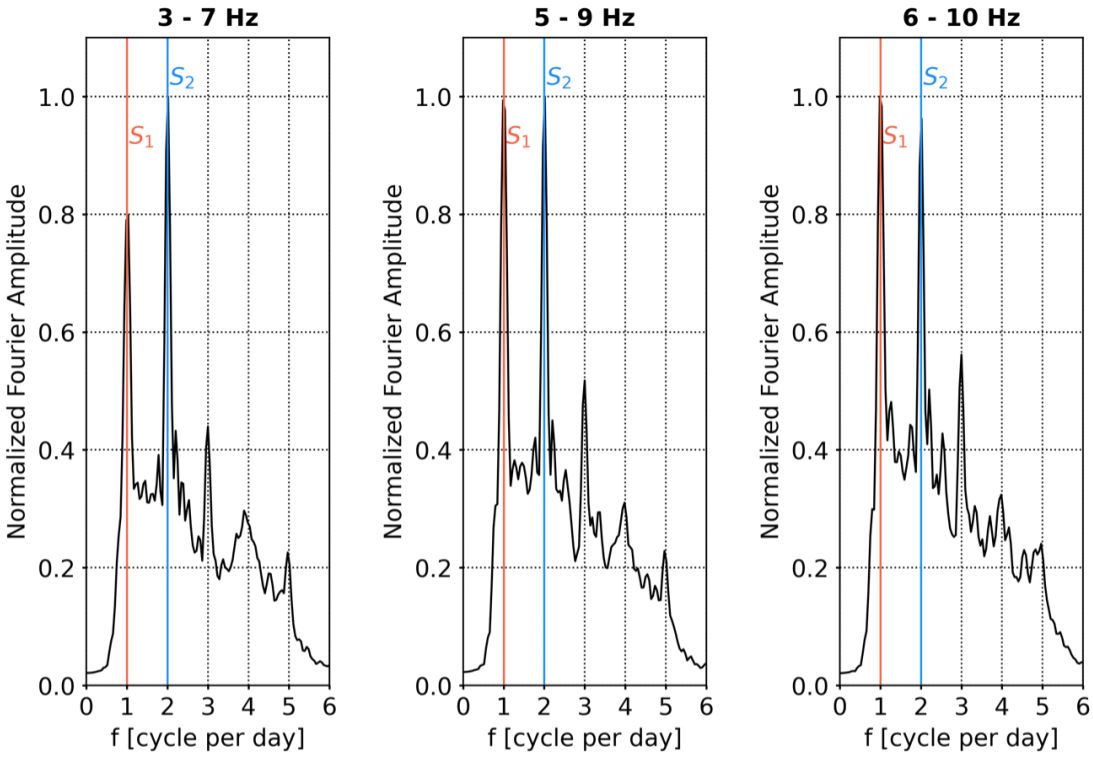


Figure A.4.: Stack of the 2D spectrograms of Fig. S3. Each panel shows a different frequency band. The red and the blue line indicates the one (S_1) and two (S_2) cycles per day, respectively.

B Appendix: Identifying large vulnerable water reservoirs using passive seismic monitoring

Temporal Evolution and Stability of Air Pressure Signal

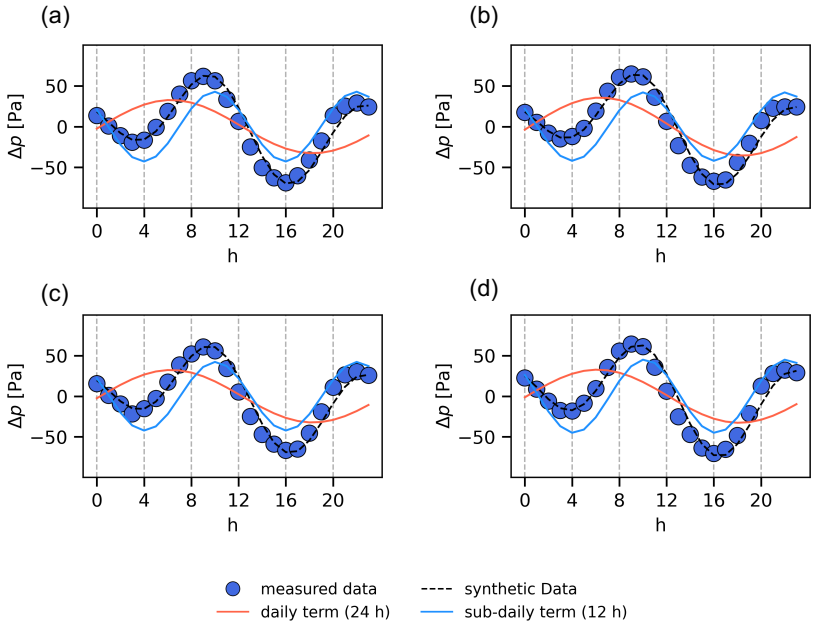


Figure B.1.: Temporal stability of the air pressure signal and the decomposition into the main periods of 24 h and 12 h. The panels (**a**) - (**d**) show the air pressure signals for the year 2016 - 2019 averaged over the whole investigation area. The dashed black line indicates the synthetic data from fitting sinusoidal functions using both 24-hour and 12-hour periods. The red and blue lines represent the fitted daily and semi-daily terms, respectively.

Temporal Evolution and Stability of Seismic Velocity Changes

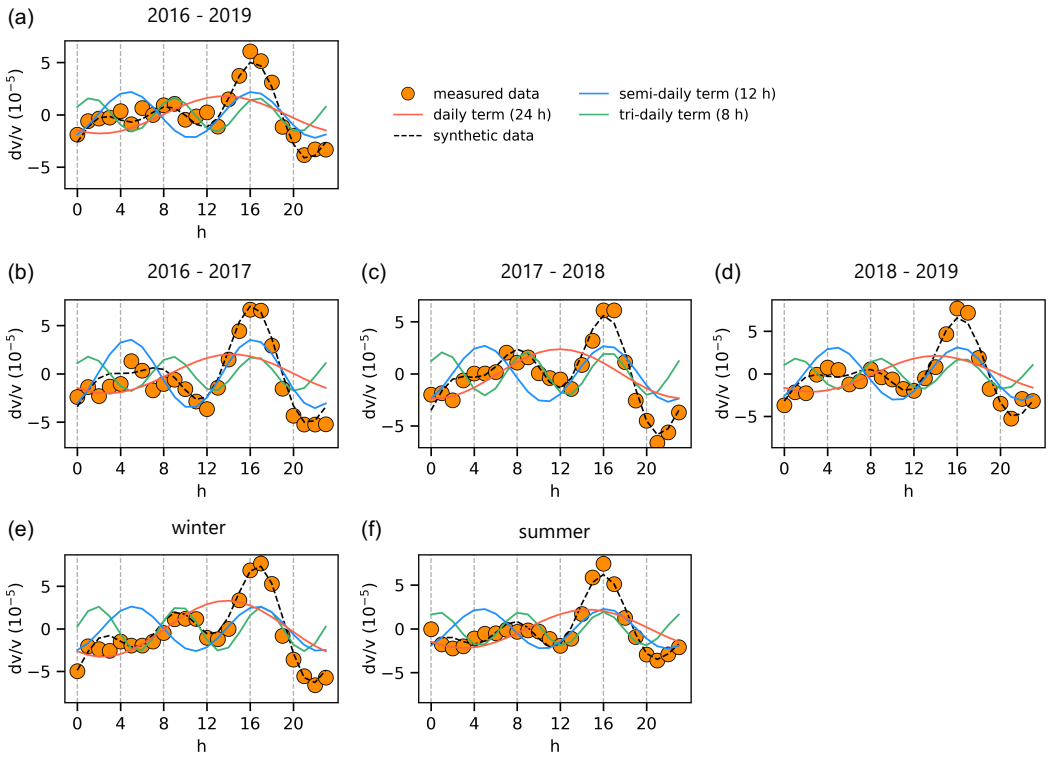


Figure B.2.: Temporal stability of the dv/v measurements (averaged over the study area) and the decomposition into the main periods of 24 h, 12 h and 8 h. (**a**) Shows the dv/v over the whole time from 2016 - 2019. The subfigures (**b**) - (**d**) show the stacking over two years as indicated to ensure a comparable station coverage. Panel (**e**) and (**f**) show the stacking result over winter and summer, respectively. The dashed black line indicates the synthetic data from fitting sinusoidal functions using both 24-hour and 12-hour periods. The red, blue and green lines represent the fitted daily, semi-daily and tri-daily terms, respectively.

Group Velocity Measurement across South and Central Europe

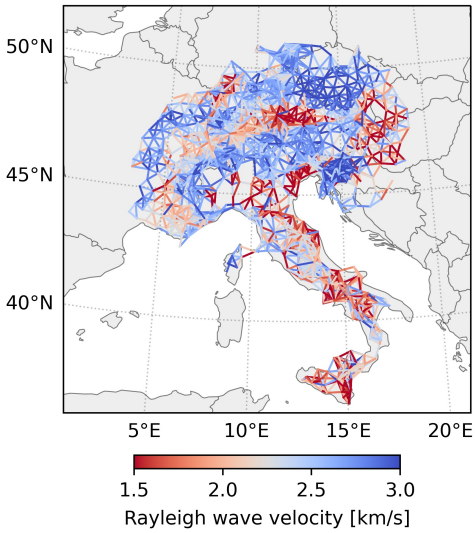


Figure B.3.: Group velocity measurements across the study area in the frequency band around 1 Hz.

Misfit of measured and fitted seismic velocity changes

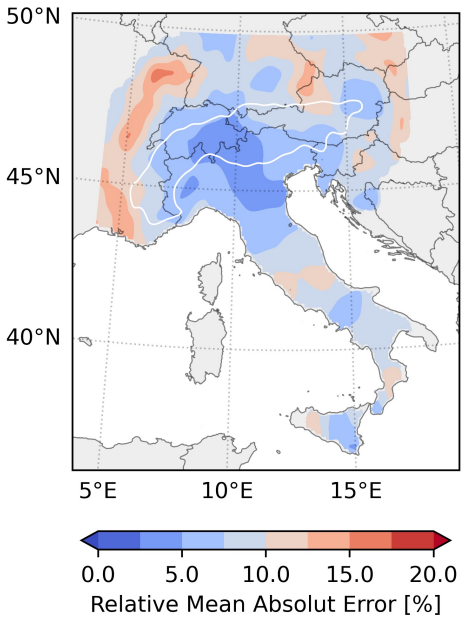


Figure B.4.: Map of the relative mean absolute misfit between the measured dv/v and the results of the fitting with three sinusoids with periods of 24 h, 12 h and 8 h.

Phase Difference between Seismic Velocity Changes and Air Pressure

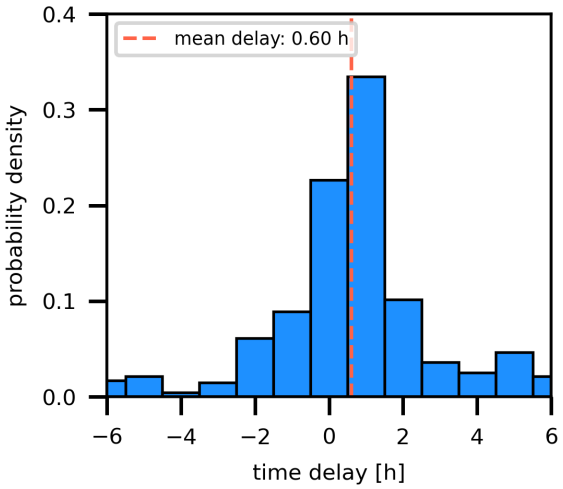


Figure B.5.: Histogram of the time delays between the air pressure (forcing) and the dv/v (reaction).

C Appendix: Monitoring Groundwater Pumping Using Time-Lapse Tomography from Ambient Seismic Noise

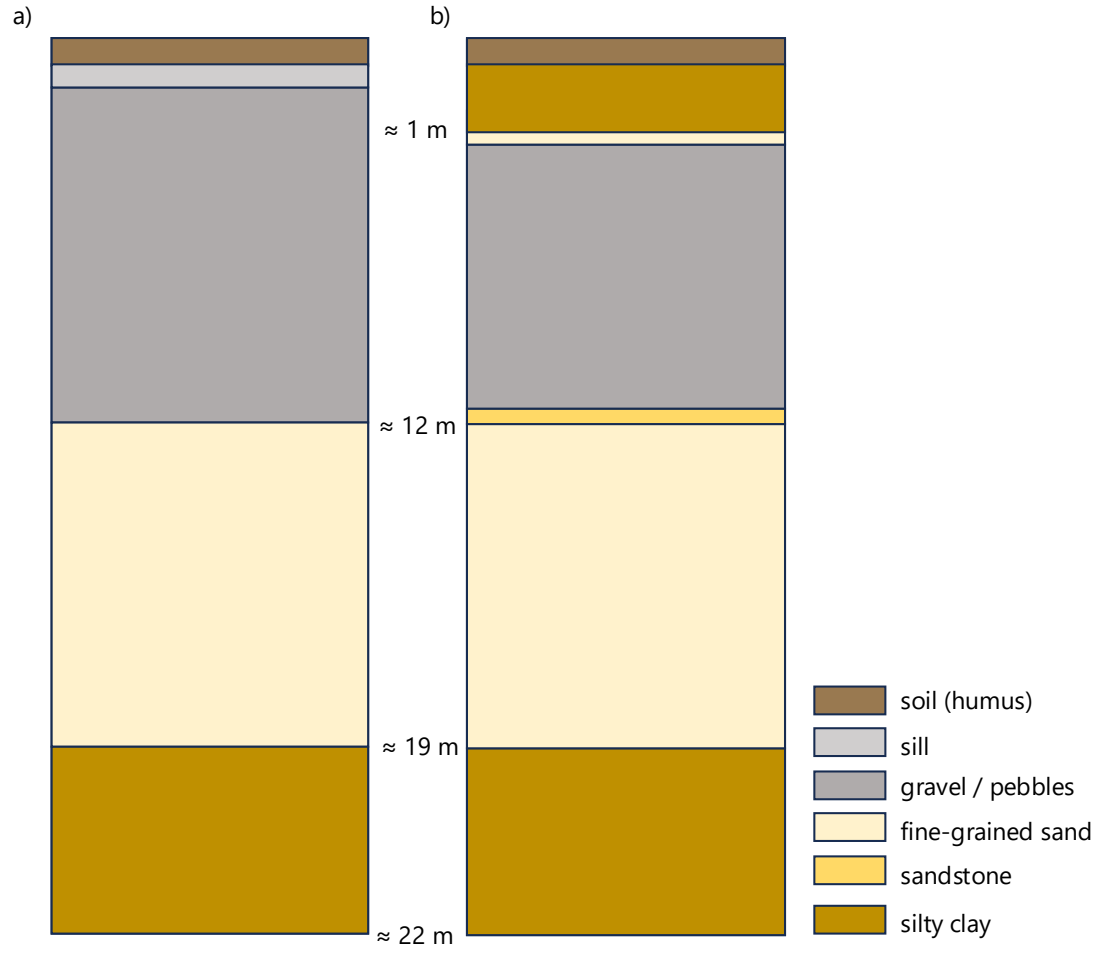


Figure C.1.: Simplified lithological log determined from core samples of **a)** the EKB5 and **b)** the EKB7 well.

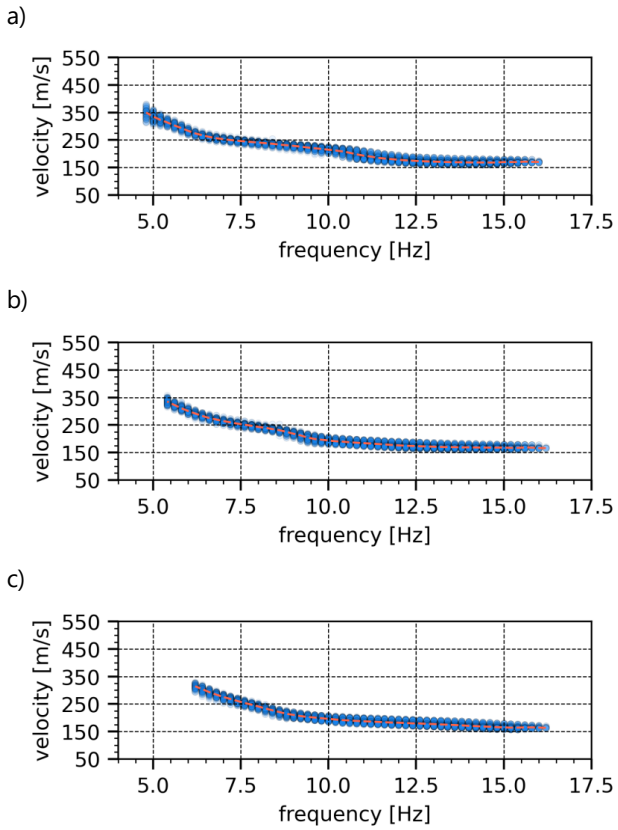


Figure C.2.: Dispersion picks for all frequencies over 93 days from station pairs **a)** "102-114", **b)** "103-114" and **c)** "104-114". The red dashed line indicated the median dispersion curve.

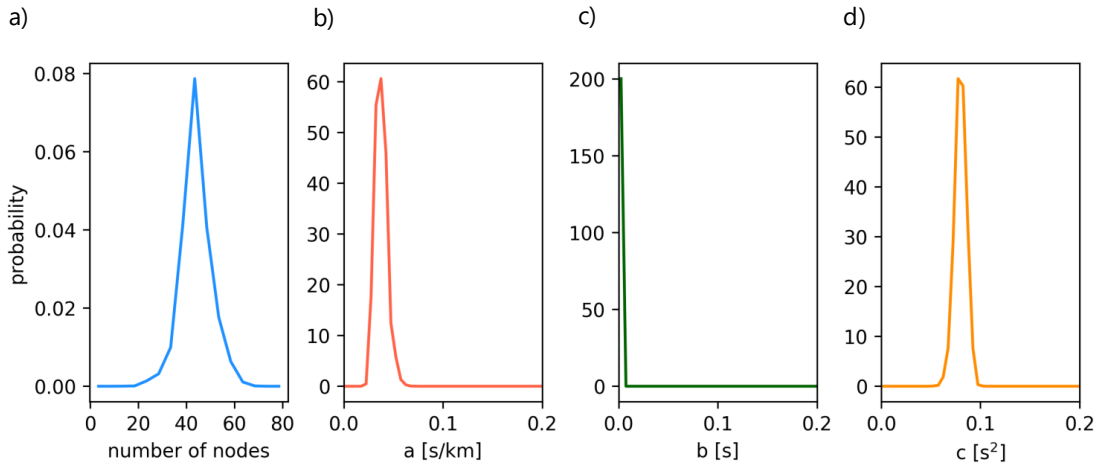


Figure C.3.: Hyper-parameter estimates obtained from the inversion of group velocity dispersion data for day 89. **a)** Histogram of the posterior distribution on the number of nodes. **b)** Diagram shows the linear coefficient between unknown data errors and travel path length. **c)** and **d)** show the constant terms for unknown data error.

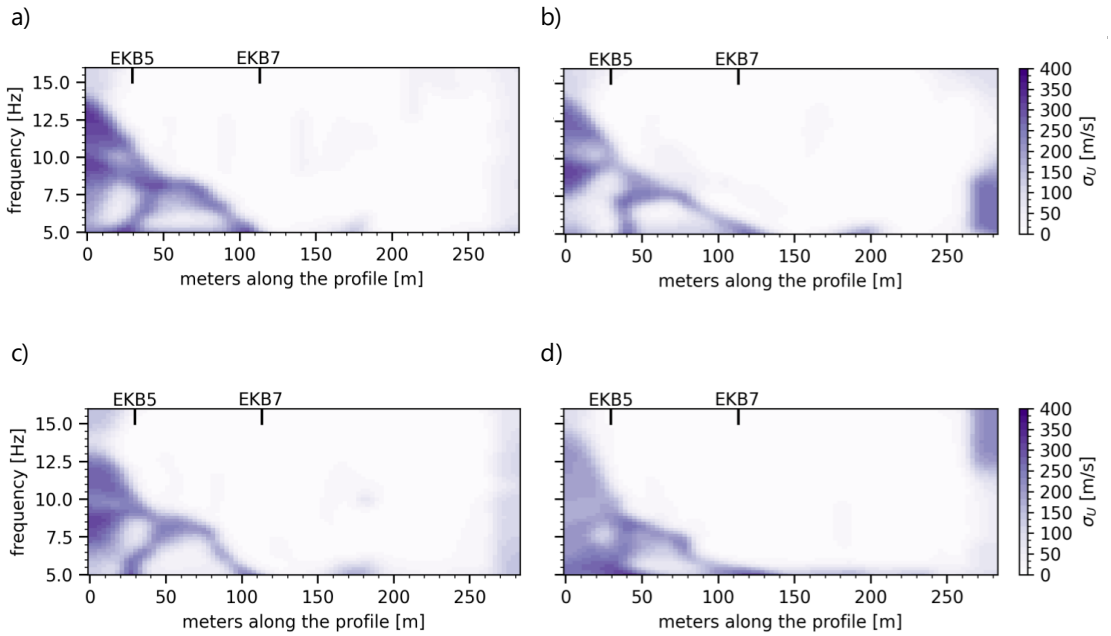


Figure C.4.: Estimated uncertainties from the 2-D group velocity inversion obtained from the ensemble of rjMcMC samples. The panels show day **a)** 9, **b)** 20, **c)** 59 and **d)** 75.

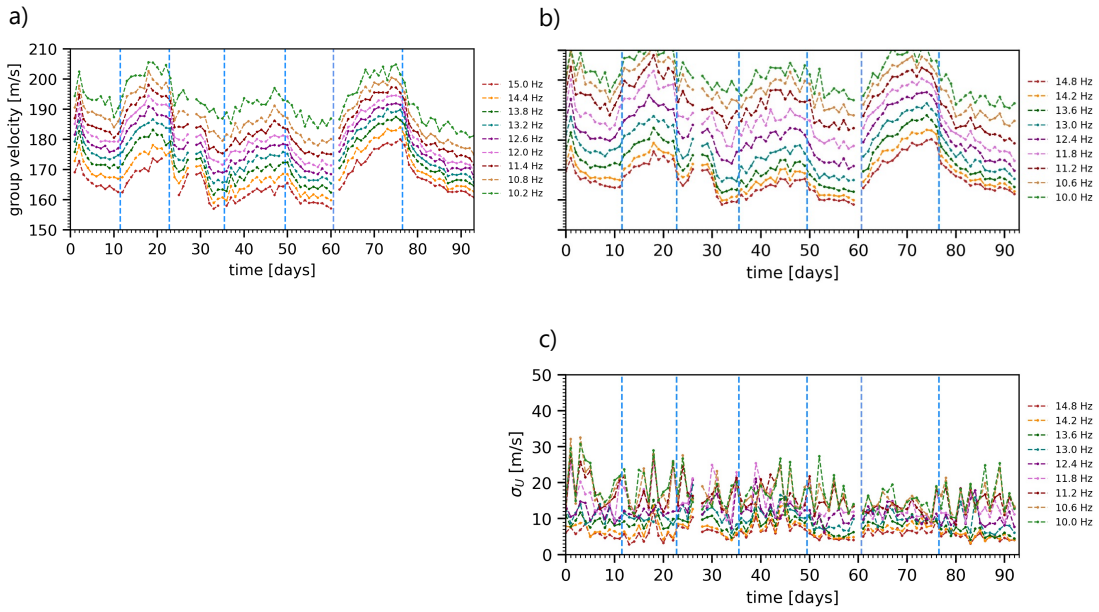


Figure C.5.: Temporal evolution of group velocities from **a)** dispersion analysis of station pair "104-113" and **b)** extracted from the 2-D group velocity profiles between 45 m and 135 m, corresponding to the extent of station pair "104-113". **c)** Shows the associated uncertainties for group velocities shown in **b)**.

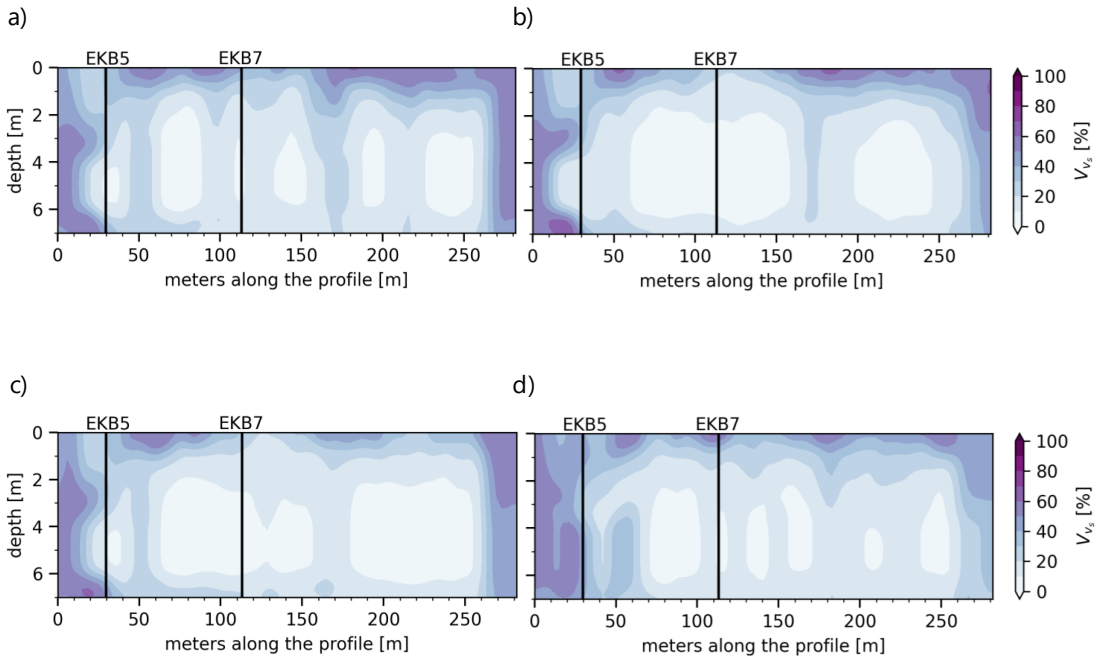


Figure C.6.: Coefficient of variation (relative standard deviation) estimated from the McMC samples for the 1-D depth inversion results of day **a)** 9, **b)** 20, **c)** 59 and **d)** 75.

Parameter	Minimum Value	Maximum Value
U_0 [km/s]	0.05	1.0
a [s/km]	0	0.2
b [s]	0	0.2
c [s^2]	0	0.2
Number of Nodes	4	80

Table C.1.: Prior bounds for the 2-D probabilistic inversion. U_0 is the group velocity, while a, b and c are the error parameters in $\sigma_i = a\Delta_i + b + c \cdot f$.

Layer	Velocity Range	Depth Range
1	(0.1 - 1) km/s	(0.001 – 0.004) m
2	(0.1 - 1) km/s	(0.006 – 0.008) m
3	(0.1 - 1) km/s	(0.016 – 0.02) m
4	(0.1 - 1) km/s	(0.01 – 0.03) m
5	(0.1 - 1) km/s	-

Table C.2.: Prior bounds for the 1-D depth inversion. Note: The last layer is the infinite half-space.

Additional Supporting Information

Movie M1 Animation of the group velocity results over time. The top panel shows the groundwater table depth measured at well EKB7. The lower panel is the result from the 2-D group velocity inversion.
Accessible via: `https://ucloud.univie.ac.at/index.php/s/opzgYtEGGdD6kBY`

Movie M2 Temporal evolution of the inverted vs model. The top panel shows the groundwater table depth measured at well EKB7. The lower panel is the resulting vs model. The blue dashed line indicated the groundwater table measured along the transect. The grey shaded areas marking parts where the relative standard deviation is higher than 40%.
Accessible via: `https://ucloud.univie.ac.at/index.php/s/opzgYtEGGdD6kBY`